TABLE OF CONTENTS

LIST OF FIGURES

Page

LIST OF ABREVIATIONS

AAD-PLL	Advanced Adaptive Digital PLL
AEF	Adaptive Ellipse Fitting
AF	Autotuning Filter
ANF	Adaptive Notch Filter
ANN	Artificial Neural Networks
ASIC	Application Specific Integrated Circuit
BEMF	Back Electromotive Force
BPF	Band Pass Filter
CCS	Code Composer Studio
CONACYT	Consejo Nacional de Ciencia y Tecnología de México (National Council of Science and Technology of Mexico)
DSP	Digital Signal Processor
DSRF-PLL	Decoupled Double Synchronous Reference Frame PLL
DTC	Direct Torque Control
EMB	Electromechanical Braking System
EMI	Electromagnetic Interference
EV	Electric Vehicle
FOC	Field Oriented Control
FW	Flux Weakening
FWL	Finite Word Length
FWT	Flux Weakening Technique
GPOC	Gain Phase Offset Correction

HEV	Hybrid Electric Vehicle
HFI	High Frequency Inductances
HFSI	High Frequency Signal Injection
HSFVI	Half Switching Frequency Voltage Injection
IC	Integrated Circuit
IEEE	Institute of Electrical and Electronics Engineers
IOA	Iterative Optimization Algorithm
IPMSM	Interior PMSM
ISG	Integrated Starter Generator
KF	Kalman Filter
LCM	Least Common Multiple
LF	Loop Filter
LHDEV	Light and Heavy-Duty EV
LMS	Least Mean Squares
LPF	Low Pass Filter
LUT	Look-Up Table
MAE	Magnetic Analog Encoder
MTPA	Maximum Torque Per Ampere
MTPV	Maximum Torque Per Volt
NCE	Network of Centres of Excellence of Canada
NLD	Non-Linear Distortion
NSERC	Natural Sciences and Engineering Research Council of Canada
PA	Polynomial Approximation

PCB	Printed Circuit Board
PD	Phase Detector
PLL	Phase Locked Loop
PMSM	Permanent Magnet Synchronous Machine
PU	Per Unit
PWM	Pulse Width Modulation
RAM	Random Access Memory
ROM	Read Only Memory
SAKO	Self-Adaption Kalman Observer
SMPMSM	Surface Mounted PMSM
SNR	Signal-to-Noise Ratio
SVM	Space Vector Modulation
THD	Total Harmonic Distortion
TI	Texas Instruments
TIE	Transactions on Industrial Electronics
V/f	Voltage Frequency
VSC	Voltage Source Converter
ZSVC	Zero Sequence Voltage Component

LIST OF SYMBOLS

R_s	Stator resistance
L_d , L_q	Direct and quadrature stator inductance
P	Number of pole pairs
Φ_r	Rotor permanent magnet flux
θ_r , θ_m	Electrical and mechanical real rotor position
δ, ρ	Rotor position error, Peak position error
$\alpha\beta$, dq	Stationary and rotating reference frame
I_d , I_q	Direct and quadrature stator current
V_d , V_q	Direct and quadrature stator voltage
X_α , X_β	Variable in the stationary reference frame
X_d , X_q	Variable in the rotating reference frame
X_a , X_b , X_c	Variable in the abc reference frame
ω_r , ω_m	Electrical and mechanical real rotor speed
Z	Impedance
τ	Torque
ΣL , ΔL	Average and difference inductance
X'	Variable in the estimated reference frame
$\tilde{X}$, $\hat{X}$, X^*	Approximated, measured and reference variable
X_{hf} , X_f	High frequency and filtered variable
V_{inj} , f_{inj}	Injected voltage and injected frequency

θ_{inj}	Injection angle of the high frequency voltage
ΔX	Variation between two sampling instants
t , t_x	Time and sampling instant *x*
n , T_s	Sample number and sampling time
f_s , f_{sw}	Sampling and inverter switching frequency
BW	Bandwidth
S	Laplace transform variable
ω_B, ω_C , ω_M	Base, critical and maximum rotor speed

INTRODUCTION

The reduction of the dependency on fossil fuels and the involved environmental concerns are motivating the research on alternative sources of energy for achieving someday a sustainable transport system. The Electric Vehicles are showing to be serious candidates to fulfill this goal. Even when the electricity used to charge them comes from a CO_2 emitting source, they pollute one half to one third of a typical combustion engine-based car because of the higher efficiency of electric machines (evHUB, 2011).

Global electric vehicles sales surpassed three quarters of a million in 2016. This is roughly 42% higher than for 2015 (EV-volumes, 2017). Bearing in mind that this exponential growing trend will certainly continue over the next years, the research regarding the different aspects of the EVs technology will also be a continuous source of study and knowledge generation.

New technologies on Li-metal batteries having super high densities of around 400-500 Wh/kg (SolidEnergy, 2016) will make possible to achieve an amazing EV autonomy range that surpasses the 346 Km. Likewise, the high band-gap semiconductors such as Silicon Carbide (SiC) and Gallium Nitride (GaN) will revolutionize the power switching devices and all the static converters-based applications. The EVs will likewise benefit from their outstanding characteristics, i.e., higher operating temperature, better thermal dissipation, higher switching frequencies and lower power losses. The new generation of 480V super-chargers will allow soon a full charge in as little as half-an hour (Tesla, 2016). The advances on machine design, power electronics and drives as well as on the control algorithms are making possible to achieve acceleration times below 5 seconds to go from 0 to 100 Km/h as well as to reach with ease top speeds over 200Km/h. In the upcoming years, not only the autonomy range, time-of-charge, acceleration-time, top speed and cost reduction are a challenge but also the reliability, safety and overall performance during the life-span of the vehicle.

The Permanent Magnet Synchronous Machine (PMSM) and the Induction Machine (IM) are the main types of electric machines currently used in the massive production market of EVs. The PMSM has been successfully integrated in various models released by Nissan, Honda and Toyota whereas the IM remains being the workhorse in companies such as Tesla, Renault, Chevrolet, Chrysler and BMW. In spite that the IM has a superior robustness, a higher reliability, a less material cost and a zero dependency on the fluctuating rare earths market, the PMSM is preferred when the characteristics of high efficiency and compactness, high power density, fast dynamics, high torque to inertia ratio and wider constant power region are demanded (Zeraoulia et al., 2006).

Either Direct Torque Control (DTC) or (FOC) Field Oriented Control can be used for independently controlling the rotor flux and the torque developed by the PMSM. The pros of DTC are a less complexity of implementation, the absence of current controllers to tune, the no requirement of the rotor position information, the less power computing and processing-time consumption as well as the ease of adaptation to any PMSM by knowing just a minimum of its basic parameters. Nevertheless, the cons of variable switching frequency, lower efficiency, poor performance at low speeds and high torque ripple generation make DTC unsuitable for high-performance PMSM-drives. Although FOC requires a deep knowledge of the machine parameters as well as a detailed analysis and a full characterization before commissioning it, the achieved performance can successfully fulfill the strict requirements of controllability, reliability and safeness demanded in EV applications.

Given that the FOC technique implies coordinate transformations from the stationary to the rotating reference frame and vice-versa, the knowledge of the rotor flux orientation indirectly measured by absolute position sensors such as resolvers and encoders attached to the shaft of the machine is essential. The closer the rotor position measurement or estimation to the real value, the better the quality of the control and the higher the achieved performance. The big importance of this rotor position variable in FOC-PMSM drives for EVs has thus been a fairly interesting and justifiable motivation of the research work presented in this thesis. The

following titles of the three *IEEE Transactions on Industrial Electronics (TIE)* published during my doctoral studies reflect the main axes of research as well as the contributions presented in this thesis: 1) A Novel Algorithm Based on Polynomial Approximations for an Efficient Error Compensation of Magnetic Analog Encoders in PMSMs for EVs 2) Effects of Rotor Position Error in the Performance of Field-Oriented-Controlled PMSM Drives for Electric Vehicle Traction Applications 3) Performance Investigation of Two Novel HSFVI Demodulation Algorithms for Encoderless FOC of PMSMs Intended for EV Propulsion: A DSP-Based Experimental Study. Note that each of these three papers is the content of Chapter 2, Chapter 3 and Chapter 4, respectively.

In Chapter 1, the problem statement, the literature review as well as the objectives and the methodology of the research work are introduced. The originality and contribution of each of the three *IEEE TIE* papers as well as the thesis summary are alike described in detail in this chapter.

In Chapter 2, a novel algorithm based on Polynomial Approximations for an efficient error compensation of MAEs in PMSMs intended for EV propulsion is presented. The proposed algorithm fairly increases the rotor-position measurement accuracy without carrying out an interpolation or a quantization operation, and advantageously, it only requires storing 56 coefficients for a fifth-order approximation, thereby reducing in around 90% the memory resources required from the DSP compared to a typical high-resolution LUT of 512 points. The PA algorithm is quite efficient bearing in mind that solely 20 multiplications and 14 additions have to be executed in real time, thus consuming less than 0.25 μs of the DSP time step set for executing the FOC algorithm. The position error of ±0.75 electrical degrees obtained with the TM4 EV drive controlling the 80 kW PMSM demonstrates that the proposed PA algorithm assisted with the type-2 PLL is a promising solution to compensate the position error of MAEs in PMSMs for EV applications.

In Chapter 3, the effects of the rotor position error in the performance of FOC PMSM-drives intended for EV traction applications are analyzed. The extended and generalized model

developed for evaluating the torque ripple produced in PMSMs due to the error from the rotor position sensor is verified in simulation for a finite-speed SMPMSM-drive and an infinite-speed IPMSM-drive. The experimental results obtained with the 400-W SMPMSM and the 80-kW demonstrate the accuracy of the proposed model. The compensation of the error from the rotary position sensor mounted on an 80-kW SMPMSM from TM4 allowed reducing the equivalent torque ripple percentage to an interval between 1% and 3% for the entire operating speed range of the machine working under the maximum symmetrical motoring and generating torque. Thanks to the torque ripple modeling and the rotor position error compensation algorithm based on PA, the maximum limit condition of 5% demanded in high-performance EV PMSM-drives has been successfully evaluated and fulfilled.

In Chapter 4, the performance of two novel HSFVI demodulation algorithms for encoderless FOC of PMSMs intended for EV propulsion is investigated. The achieved DSP-based qualitative and quantitative comparison analysis exhaustively validated through simulations and experiments with a 2.5kW PMSM shows that the proposed PWM-based HSFSI techniques present a smaller rotor position error and a larger bandwidth than the classic SVM-based HFSI sensorless algorithms. Therefore, they allow a better machine control performance in terms of a smaller torque ripple generation and a faster current control loop. Thanks to the very small dq-inductances value and the larger saliency ratio of the simulated 80kW IPMSM intended for EV propulsion, the dc bus voltage utilization percentage required for achieving a large high frequency stator currents SNR and thus a small rotor position estimation error does not limit the operating frequency of the proposed HSFVI algorithms. Hence, the parameters of the EV-IPMSM can allow increasing eventually the injection frequency up to 20 kHz, where the audible noise is virtually unnoticeable for human ear. The use of the proposed pulsating and rotating HSFPWM sensorless techniques for estimating the rotor position in the low speed range and the standstill condition can thereby positively contribute to the fault-tolerant and reliability enhancement in LHDEV PMSM-traction drives.

The thesis finalizes providing the general conclusions, the future work and the Appendices I, II, III and IV that contain important design and analysis information as well as more data and details added for complementing each of the three research papers.

The proposed algorithms, the developed models, the derived equations as well as the obtained simulations and experimental results constitute valuable performance improvements on rotor position sensored and sensorless FOC of PMSMs intended for EV propulsion applications.

CHAPTER 1

RESEARCH OUTLINE

This chapter presents the outline of the research work included in this thesis. Section 1.1 describes the problem statement that has motivated the development of this doctoral study. The literature review given in section 1.2 provides an overview of the solutions proposed by researchers over the last years for giving a step-forward in the problem solving. The objectives of the thesis as well as the methodology followed to achieve the goals are defined in section 1.3. The originality and contribution of each of the three *IEEE TIE* papers is explained in section 1.4 whereas the details of the *IEEE* Transactions and the *IEEE* Conference articles published during my doctoral studies are given in section 1.5. Finally, a summary of chapters 2, 3 and 4 is given in section 1.6.

1.1 Problem statement

The research work presented in this thesis addresses three main problems.

The first problem is described as follows: In order to perform field-oriented control (FOC) of permanent-magnet synchronous machines (PMSMs), the orientation of the rotor flux generated by the permanent magnets must be known. This variable is indirectly measured by absolute rotary position sensors such as resolvers and encoders attached to the machine shaft. In electric vehicle (EV) applications, the performance of such sensors is highly demanding because the rotor position measurement is directly related to the torque quality produced by the PMSM. Given that even a costly high-quality encoder or resolver with remarkable resolution, precision, and accuracy and based on any operating principle will present an inherent periodic position error due to different causes (Hanselman, 1990; Lara and Chandra, 2014b; Lin et al., 2011) including the nonideal mechanical mounting of their components on the machine, thus the use of low-cost rotary position sensors improved with efficient position-error compensation algorithms is strongly attracting the attention of academic

researchers and industry professionals. The main nonidealities found in the quadrature analog signals from these position sensors must be fairly compensated in order to achieve a high-performance control of the PMSM.

The second problem is described as follows: Rotor position error plays a very important role in high-performance field-oriented control (FOC) of permanent-magnet synchronous machines (PMSMs) intended for EV traction applications, where the maximum average torque with a minimum torque ripple is demanded over the entire operating speed range of the machine. Because of the inherent position error from the encoder or resolver attached to the PMSM shaft, the direct and quadrature stator currents deduced from the Park's transformation provide a mistaken feedback to the FOC algorithm; thus, producing real stator current vectors characterized by the unwanted effects of torque ripple and air-gap flux variations. (Chen et al., 2007; Hao et al., 2013; Rahman and Hiti, 2005) have analyzed the torque–speed characteristic curves of various IPMSMs considering different errors from the rotary position sensor. The obtained curves demonstrate how an inaccurate rotor position measurement leads to a severe degradation of the machine-drive performance and how in some cases, the resulting torque, power and efficiency reduction along the flux weakening (FW) region can reach unacceptable levels. Therefore, the development of a model for analyzing the impact of the rotor position error in the PMSM-drive performance is mandatory.

The third problem is described as follows: The performance of FOC-PMSMs heavily depends on the accuracy and resolution of the rotor position sensor (Lara et al., 2016a). High quality encoders and resolvers can fulfill this requirement in demanding applications (Lara and Chandra, 2014b) such as PMSM-drives for light and heavy-duty electric vehicle (LHDEV) traction applications (Lara et al., 2016b). Nevertheless, the sensor components are prone to mechanical and electrical failures that can put the vehicle out of service or even lead to severe dangerous scenarios. In this regard, the use of rotor position sensorless algorithms working as a backup of the position sensor can positively contribute to the fault-tolerant and reliability enhancement in LHDEV PMSM-traction drives (Kano et al., 2013).

1.2 Literature review

The state-of-art and the research done in the past addressing each of the three problem statements defined in section 1.1 is portrayed below:

For the first problem the literature review is as follows : Over the last years, different radial and axial configurations of low-cost linear Hall-effect sensors have been proved to be effective for providing high-resolution and accurate rotor position measurements (Hu et al., 2012; Wu et al., 2014) including electromechanical braking systems (EMB) (Choi et al., 2015), vacuum pumps (Jung and Nam, 2011), and PMSM integrated starter generators (ISG) for hybrid electric vehicle (HEV) applications (Chen et al., 2007). Likewise, interesting online compensation algorithms have been also devised to counteract the main nonidealities found in the quadrature analog signals from these position sensors: iterative optimization algorithm (IOA) (Lara and Chandra, 2014b), Kalman filter (KF) (Hu et al., 2012), adaptive notch filter (ANF)-phase-locked loop (PLL) (Jung and Nam, 2011), self-adaption Kalman observer (SAKO) (Shi et al., 2015), autotuning filter (AF) (Qamar et al., 2015), artificial neural networks (ANN) (Kok Kiong and Kok-Zuea, 2005), adaptive ellipse fitting (AEF) (Hoseinnezhad et al., 2007), advanced adaptive digital (AAD)-PLL (Hoang and Jeon, 2011), decoupled double synchronous reference frame (DSRF)-PLL (Bergas-Jan et al., 2012; Xu et al., 2012), gain-phase-offset-correction (GPOC) (Bunte and Beineke, 2004; Faber, 2012), probabilistic learning (Kavanagh, 2001), Fourier analysis (Aksenenko and Matveyev, 2005; Ramakrishnan et al., 2013), and some other special methods (Hwang et al., 2011; Hwang et al., 2010; Mok et al., 2007). In contrast to the online correction algorithms, the static calibration methods are less prone to undergo instability conditions that can unexpectedly lead to dangerous scenarios in a real EV on the road. A traditional static calibration consists in a compensating look-up table (LUT) (Hagiwara et al., 1992; Hanselman, 1991; Ju-Chan et al., 2006; Lin et al., 2011; Tan et al., 2002) that generally stores either the position error or the direct mapping of the measurement from the position sensor under test to the reading of a high accuracy encoder. A better error compensation is possible by increasing the LUT resolution. Nevertheless, the larger amount of memory required to store the data is a tradeoff

in embedded applications running on low-cost digital signal processors (DSP), where hardware resources are quite limited.

For the second problem the literature review is as follows: Over the past years, different torque ripple minimization techniques roughly categorized into machine design and machine control have been proposed by academicians and industry professionals (Nakao and Akatsu, 2014). On the machine-control side, diverse algorithms based on repetitive control (Mattavelli et al., 2005), artificial neural networks (Flieller et al., 2014), resonant controllers (Xia et al., 2015; Yepes et al., 2015), fuzzy logic (Uddin, 2011), predictive control (Chai et al., 2013; Cho et al., 2015; Zhu et al., 2012), adaptive control (Mohamed and El-Saadany, 2008; Petrovic et al., 2000; Sencer and Shamoto, 2014), and iterative learning control (Weizhe et al., 2004; Weizhe et al., 2005) have been proved to be effective in reducing the amplitude of both torque and speed error oscillations in various PMSM applications. This kind of algorithms counteracts the global effect of numerous sources that contribute concurrently to the torque ripple generation, e.g., asymmetric stator phase resistance (Xu et al., 2014), nonsinusoidal air-gap flux density, rotor permanent-magnet field and stator slots interaction, imperfect current sensing, finite resolution of the pulse width modulation (PWM), among others (Gebregergis et al., 2015; Shaotang et al., 2002; Weizhe et al., 2004; Xu et al., 2014). However, the experimental results obtained in this study with two different PMSMs show that the torque oscillations caused by these sources are negligible compared to the torque ripple produced by just a few electrical degrees of error in the rotor position measurement. For this reason, the research work of (Hanselman, 1990; Lara and Chandra, 2014b; Lara et al., 2016b; Lin et al., 2011; Ramakrishnan et al., 2013) mainly focuses on the inaccuracy of the position sensor for evaluating the overall performance of FOC PMSM-drives intended for EV applications. Below the base speed, the influence of the rotor position error on the PMSM-drive performance is negligible. Nevertheless, it becomes increasingly important with rotor speed along the constant power region. Therefore, the performance analysis results are inherently correlated with the FW technique used for the simulations and the experimental tests. In the past, insightful techniques that increase the voltage utilization of the limited dc bus as well as effective and efficient FW algorithms have been devised to

extend the PMSM-drives torque–speed characteristics (Bolognani et al., 2014; Bon-Ho et al., 2003; Gallegos-Lopez et al., 2005; Jung et al., 2015; Lin and Lai, 2012; Nalepa and Orlowska-Kowalska, 2012; Wai and Jahns, 2001). The scheme proposed by Wai and Jahns (Wai and Jahns, 2001) has the advantages of simplicity and good performance. The original scheme that consists of an integrator with antiwindup must be adapted for working in both motoring and generating modes.

For the third problem the literature review is as follows: The High Frequency Signal Injection (HFSI) methods rely on the geometrical and saturation saliency properties of the machine (Ha, 2008). The variation of the high frequency inductances (HFI) as a function of the rotor position makes possible the estimation at standstill as well as in the low-speed range where the Back-Electromotive Force (BEMF)-based algorithms are inherently unsuitable. The HFSI methods are also feasible for the high speed range provided that the HFI are relatively small so that the voltage required from the DC bus for injection purposes is not a concern (Gao et al., 2009; Masaki et al., 2002). Over the last years, researchers have done a significant step-forward regarding the HFSI algorithms for encoderless FOC of PMSMs. The exhaustive classification presented in (Briz and Degner, 2011) considers important aspects such as the continuity of the excitation, the machine winding connection, the number of sensors required for either voltage or current injection, the frame of coordinates as well as the type of modulation. In Voltage Source Converter (VSC)-based algorithms working with SVM, the injection frequency range commonly varies around 400Hz-1kHz (Ji-Hoon et al., 2004; Ji-Hoon et al., 2003; Lara et al., 2012; Liu and Zhu, 2014; Luo et al., 2016; Wang et al., 2013; Xu and Zhu, 2016a; 2016b; Yu-seok et al., 2005) whereas in the algorithms working with PWM, the injection frequency is near the switching frequency (Gabriel et al., 2013; Kano et al., 2012; Kim et al., 2016; Kim et al., 2011b; Kim and Sul, 2011; Yoon et al., 2011) or even they become equal (Kim et al., 2011a; 2012; Lara and Chandra, 2014a; Masaki et al., 2002). The frequency range of the injected signal in the methods using PWM is much higher than in those using SVM. This difference is mainly because the HF demodulation algorithms in the PWM-based methods do not involve digital filters. By doing so, the top injection frequency is inherently limited given that for a constant sampling rate, the number of samples decreases as

the frequency of the injected signal increases, thus deteriorating the performance of the filters. In order to overcome this issue, the use of analog filters for HF demodulation purposes has been recently proposed in (Jung and Ha, 2015). The PWM modulation is also preferred over SVM when the HF demodulation algorithm is sensitive to the inverter nonlinearities, e.g. the dead-time effect can give rise to a severe deterioration of the rotor position estimation (Briz and Degner, 2011; Gabriel et al., 2013). The use of higher frequencies using PWM-based algorithms is likewise motivated due to the audible nuisance caused by the sound that arises from the vibration of the stator windings of the machine. If the frequency of the injected signal reaches the upper pitch audibility limit of human ear of around 20 kHz, the hassle acoustic frequency can be virtually unnoticeable (Gabriel et al., 2013; Jung and Ha, 2015; Kim et al., 2012). In previous literature on the subject (Kim et al., 2011a; 2012; Kim et al., 2016; Kim et al., 2011b; Ogasawara and Akagi, 1998; Petrovic et al., 2003), the HF demodulation algorithms working in the stationary reference frame require both voltage and current measurements given that they are based on the inductance matrix of the PMSM model that contains the valuable rotor position information. This dependency on stator voltage measurements makes the demodulation particularly susceptible not only to measurement errors due to the inaccuracy and limited bandwidth of the voltage sensors but to the imprecise extraction and computing of the mean value from the high frequency voltage pulse over a carrier period. A special acquisition system with a sampling frequency much higher than the switching frequency is required to achieve accurate results. Moreover, when the voltage references from the FOC are used instead of the measured values, the rotor position estimation is inherently degraded given that the nonlinearities of the inverter are fully disregarded. Likewise, the HF sensorless algorithms based on zero-sequence voltage components (ZSVC) (Xu and Zhu, 2016a; 2016b) not only require extra-hardware but access to the neutral point of the machine, which is not typically available in industrial drives (Briz and Degner, 2011). The ZSVC-based methods are inherently unfeasible for implementation in PMSMs with delta-connected windings.

1.3 Objectives and methodology

This research work has the aim of contributing to the solution of the three problems stated in section 1.1. Accordingly, the three objectives of this thesis are as follows:

1) To develop a novel algorithm for compensating the rotor position error in magnetic analog encoders (MAE) used in PMSMs intended for electric vehicle propulsion;

2) To develop a model for analyzing the effects of the rotor position error in the performance of FOC-PMSM drives intended for EV traction applications;

3) To investigate the performance of two novel Half Switching Frequency Voltage Injection (HSFVI) demodulation algorithms for encoderless FOC of PMSMs intended for EV propulsion.

The methodology adopted for achieving each of these three objectives is composed by the following five sequential steps:

a) Development of the mathematical model that supports the theory behind the proposal. The nonidealities present in the quadrature signals of magnetic encoders, i.e., amplitude mismatch, nonzero dc offset, nonorthogonality and harmonic distortion produce a characteristic periodical position error. The expressions that model the error produced due to each of these nonidealities have been mathematically deduced. The resulting set of equations constitutes the first model developed in the methodology. The second developed model has made possible the evaluation of the torque ripple produced in PMSMs due to the error from the rotor position sensor along the different characteristic trajectories and operating regions of the machine. The third developed model supports the theory behind the PMSM that makes possible the encoderless FOC of the machine by means of the proposed Half Switching Frequency Voltage Injection (HSFVI) demodulation algorithms.

b) Preliminary validation through MATLAB-SimPowerSystems-based simulations of the models and algorithms developed for solving the problematic. The SimPowerSystems toolbox is a very powerful tool to simulate the behavior of electrical and mechanical dynamic systems. This tool has allowed simulating the sensored and sensorless FOC algorithms applied to both SMPMSMs and IPMSMs. Likewise, the position errors obtained from the nonidealities of the magnetic encoder have been validated using Simulink and an m-file containing the modeling equations. Thanks to the simulation results, important questions have also been answered before building the prototype in the laboratory, e.g. the DC voltage required for the drive to develop the maximum torque at the desired maximum speed, the total power generated during regenerative braking, the torque ripple in the different operating regions, the magnitude of the high frequency current produced for a given magnitude of high frequency voltage injected in the stator windings of the machine, among others. In order to achieve high-performance of the developed algorithms in the various machines analyzed, it was necessary to accurately tune the PI current controllers, the PI position estimators, the PI compensator in the PLLs as well as the flux weakening regulators. The procedure to find the optimal gains of these controllers is generally a complex task. However, given that the simulations were carried out with the same time-steps used in the DSP for the experiments, i.e., 50μs, 125μs and 200μs, the tuning of the diverse controllers was done with relative ease. The obtained simulation results also have strongly helped to identify and size the components and equipment required for the experimental validation before purchasing them or mounting them, thus saving money, time and effort. Although the discretization and quantization operation performed for carrying out the control with a digital processor inherently implies a mapping error between the continuous and the discrete domains given that the real plant and the analog sensors inherently belong to a continuous system, it has been possible to achieve a high-performance FOC of the PMSM. It must be also beared in mind that the simulation only considers a few main variables that characterize the physical system. Therefore, the simulation results are just an approximation to the real system response. However, the simulation curves obtained from this simplified model provide a quite acceptable behavior prediction. If the

immense number of variables that influence the real system as well as the nonlinear dependency and interaction among them were considered in the simulation, it would become highly complex and unfeasible.

c) Software development for executing the required algorithms in real-time using a TI® DSP. Once the simulations provide good results, the proposed models and algorithms have been implemented to work in real-time on a Digital Signal Processor (DSP). The Matlab-Simulink environment includes an embedded-coder toolbox capable of automatically generating C-language code fully compatible with the TI® C2000 family of DSPs. This tool is very useful and allows saving too much programming time. Nevertheless, for a complex control system, the generated code needs to be improved in order to achieve an acceptable small execution time-step whereas the time-critical routines must be necessarily hand-programmed. The integration of generated-code and hand-code was carried out successfully in C-language using Code Composer Studio®. The resulting .out file obtained after compilation, assembly and linking allows programming either the flash or the RAM memory of the DSP.

d) Building and mounting of the experimental setups in the hardware laboratory. Three different test benches have been built to obtain the experimental results that validate the proposed models and algorithms. The first setup consisted of the machine under test, a three-phase wye-connected 400-W SMPMSM tightly coupled to another 400-W SMPMSM controlled in speed-mode by a high-performance industrial drive. Two reconfigurable banks of rechargeable lead-acid batteries from Enerwatt® have been used to feed the dc bus of the two-level inverter based drives. The second setup consisted of an EV-drive controlling an 80-kW SMPMSM, both of them designed and manufactured by the company TM4®. The 80-kW machine has been coupled to the driveshaft of an induction machine by means of an EV gearbox with a ratio of 10:1. The third setup consisted of a 2.5-kW SMPMSM with radially inset rotor magnets. This machine has been coupled to a 4kW induction machine controlled in speed mode by an 8kW ABB®-drive implementing DTC. The 250Vdc-bus of the Lab-Volt® inverter connected to the

2.5-kW PMSM has been fed with a 4kW bi-directional DC voltage source from Convertronix®. In the second and third setups, the energy generated during the regenerative braking has not been dissipated through resistors in the form of heat but it has been sent back to the grid. The first and third setups with the 400W and 2.5kW PMSMs have been built at GRÉPCI-ÉTS laboratory whereas the second setup with the 80kW PMSM has been built at TM4® facilities. Likewise, the developed magnetic encoder prototype was successfully mounted on the back-side of the three PMSMs under test. Moreover, in the three setups, the board that controls the drive and performs in real-time the FOC of the machine is based on a DSP from Texas Instruments®.

e) Final validation of the theoretical models and the simulations by means of exhaustive experimental tests under different operating conditions. This stage also includes the characterization, performance evaluation and comparison of the achieved results with respect to the ones reported in previous published works. The first setup with the 400W PMSM was tested at ±5000 r/min under no torque as well as at −3000 r/min and ±4000 r/min under torque step-changes from ±1.2 to ∓1.2 Nm while alternating from the uncompensated to the compensated rotor position. The second setup with the 80-kW PMSM has been evaluated for both motoring and regenerative braking operation modes under maximum torque conditions varying from 100 Nm at 1000 r/min up to 55 Nm at 9000 r/min. The third setup with the 2.5kW PMSM has been tested at 300 rpm under 100% torque step-changes of ±9Nm. The experimental results obtained with the three different setups have successfully demonstrated the validity of the proposed models and algorithms.

1.4 Originality and contribution

The originality of each of the three proposed solutions and their contribution with respect to the state-of-the-art and the research works published over the past years are explained below:

1) The proposed algorithm based on polynomial approximations (PA) quite reduces the size

of the required read-only memory (ROM) in comparison with a very high-resolution calibration LUT. The use of polynomials allows compensating every possible input rotor position without carrying out an interpolation or a quantization operation. Advantageously, the polynomial coefficients are deduced from a calibration procedure that does not require an accurate and high-resolution position sensor for comparison and error-calculation purposes.

2) In the implementation of the techniques of MTPA, FW1, and MTPV/FW2, the vector control condition $\vec{I}_d{}' = 0$ assumed in the previous literature for finding the torque developed by the PMSM as a function of the rotor position error is no longer satisfied. The proposed extended and generalized model considering the condition $\vec{I}_d{}' \neq 0$ is valid for both SMPM and IPM machines working in any of the aforementioned scenarios.

3) The two proposed half switching frequency demodulation algorithms in the stationary and rotating coordinates estimate the rotor position angle without requiring any information about the inverter output voltage feeding the stator windings of the PMSM. The use of only current measurements simplifies their implementation and allows avoiding voltage measurement issues as well as voltage assumptions and approximations that inherently deteriorate the valuable position estimation. The no need of extra-hardware and the capability of working indistinctly with PMSMs having either delta- or wye-connected windings allow an easier integration of the proposed algorithms with most of the PMSM-drives currently available in industry.

1.5 Publications

The proposed solution for each of the three problems formerly described in section 1.1 is the key content of Chapter 2, Chapter 3 and Chapter 4, respectively. Each of these Chapters corresponds to one of the papers already published or submitted on the prestigious *IEEE Transactions on Industrial Electronics.* This journal has an impact factor of 6.383, one of the highest in the *IEEE* ranking.

The first Transactions paper already published is:

1) Lara, J., J. Xu, and A. Chandra. 2016a. "Effects of Rotor Position Error in the Performance of Field-Oriented-Controlled PMSM Drives for Electric Vehicle Traction Applications". *IEEE Transactions on Industrial Electronics,* vol. 63, n^{o} 8, p. 4738-4751.

The second Transactions paper already published is:

2) Lara, J., J. Xu, and A. Chandra. 2016b. "A Novel Algorithm Based on Polynomial Approximations for an Efficient Error Compensation of Magnetic Analog Encoders in PMSMs for EVs". *IEEE Transactions on Industrial Electronics,* vol. 63, n^{o} 6, p. 3377-3388.

The third Transactions paper already submitted is:

3) Lara, J., and A. Chandra. 2016c. "Performance Investigation of Two Novel HSFVI Demodulation Algorithms for Encoderless FOC of PMSMs Intended for EV Propulsion: A DSP-Based Experimental Study". Submitted to *IEEE Transactions on Industrial Electronics* on November 2016 (Paper Submission Number: 16-TIE-3349).

Although the three following *IEEE* Conference articles have been already published, they have not been included in the Chapters. However, their content information has contributed to enrich the literature review and the state-of-art of the Transactions papers. The citations of these conference papers are given below:

1) Lara, J. and A. Chandra. 2014a. "Performance study of switching frequency signal injection algorithm in PMSMs for EV propulsion: A comparison in stator and rotor coordinates". In *2014 IEEE 23rd International Symposium on Industrial Electronics (ISIE)*. (1-4 June 2014), p. 865-870.

2) Lara, J. and A. Chandra. 2014b. "Position error compensation in quadrature analog magnetic encoders through an iterative optimization algorithm". In *IECON 2014 - 40th Annual Conference of the IEEE Industrial Electronics Society*. (Oct. 29 2014-Nov. 1 2014), p. 3043-3048.

3) Lara, J., A. Chandra, and J. Xu. 2012. "Integration of HFSI and extended - EMF based techniques for PMSM sensorless control in HEV/EV applications". In *IECON 2012 - 38th Annual Conference on IEEE Industrial Electronics Society*. (25-28 Oct. 2012), p. 3688-3693.

1.6 Thesis summary

A brief description of the content organization of Chapter 2, Chapter 3 and Chapter 4 is given below.

The content of Chapter 2 is organized as follows: Section 2.2 presents the mathematical model of the position error caused by the main nonidealities found in quadrature analog encoders. In section 2.3, the calibration procedure and the proposed PA compensation algorithm are explained in detail. The experimental results obtained from the calibration procedure and the proposed compensation algorithm assisted with a type-2 PLL are shown in section 2.4. The experimental validation with the TM4 EV drive controlling an 80 kW PMSM is presented in section 2.5. Finally, the conclusion and some important remarks are given in section 2.6.

The content of Chapter 3 is organized as follows: Section 3.2 presents the proposed extended and generalized modeling of the torque ripple produced in PMSMs due to the error from the rotor position sensor. The characteristic trajectories in the different operating regions of the PMSM are derived and described in detail in section 3.3. Section 3.4 shows the simulation results obtained from the torque ripple evaluation along the particular trajectories of a finite-speed 400-W SMPMSM-drive and an infinite-speed 80-kW IPMSM-drive intended for high-speed EV propulsion. The rotor position sensor and the rotor position error compensation algorithm used in this study are described in section 3.5. The experimental results obtained with the 400-W SMPMSM-drive previously simulated are shown in section 3.6. In order to evaluate the torque ripple for the general PMSM model, the simulations of section 3.4 are carried out with an 80-kW IPM machine. However, the experimental validation presented in section 3.7 is performed with an 80-kW SMPM machine. Finally, the conclusion and some important remarks are given in section 3.8.

The content of Chapter 4 is organized as follows: The classical pulsating and rotating SVM-based HFSI techniques are analyzed in section 4.2 while the proposed PWM-based HSFSI algorithms in both stator and rotor coordinates are presented in section 4.3. Each of these sections includes its respective high-frequency PMSM model and equations that theoretically support the encoderless FOC of the machine. The MATLAB–SimPowerSystems-based simulations and the experimental results obtained with the 2.5kW PMSM having radially inset rotor magnets are shown next to each other along the text of section 4.2 and section 4.3, thus allowing a simultaneous validation and an easier tracing and comprehension of the characteristic waveforms for the different methods. The quantitative and qualitative performance comparison and analysis for the four HFSI sensorless techniques are presented in section 4.4. This section also includes the simulation results obtained from the encoderless FOC of an 80kW IPMSM intended for EV propulsion. Finally, the conclusion and some important remarks are given in section 4.5.

CHAPTER 2

A NOVEL ALGORITHM BASED ON POLYNOMIAL APPROXIMATIONS FOR AN EFFICIENT ERROR COMPENSATION OF MAGNETIC ANALOG ENCODERS IN PMSMS FOR EVS

Jorge Lara [a], Jianhong Xu [b], Ambrish Chandra [c]

[a,c] Department of Electrical Engineering, École de Technologie Supérieure, 1100 Notre-Dame Ouest, Montréal, Québec, Canada H3C 1K3
[b] TM4 Electrodynamic Systems, 135 Joseph-Armand Bombardier, Boucherville, Québec, Canada J4B 8P1

Article published in « IEEE Transactions on Industrial Electronics » on June 2016.

Abstract

This paper presents a novel algorithm based on polynomial approximations (PAs) for an efficient error compensation of magnetic analog encoders (MAEs) in permanent-magnet synchronous machines (PMSMs) intended for electric vehicle (EV) propulsion. The proposed PA algorithm requires a negligible memory space compared to a very high-resolution look-up table (LUT). The use of polynomials allows compensating every possible input rotor position without carrying out an interpolation or a rounding to the nearest quantized value. The PA algorithm has been implemented to work in real time on a TM4 EV drive controlling an 80 kW PMSM. The performance of the algorithm has been validated at 6000 and 9000 r/min under +85 and ±55 Nm of torque, respectively. Considering an EV gearbox with a ratio of 9.7:1 and tires with a diameter of around 49 cm, the PMSM rotor speed from these tests are equivalent to a vehicle's speed of about 58 and 87 Km/h, respectively. The electromagnetic interference (EMI) effects have been minimized using a type-2 phase-locked loop (PLL). The proposed PA algorithm assisted with the PLL is capable of reducing the total position error to a range as small as ±0.2 mechanical degrees. Bearing in mind that the

machine has five pole pairs, this error is equivalent to ±1° electrical degrees. The combination of these two algorithms is a promising solution for compensating the position error in quadrature analog encoders. The experimental results obtained with the 80 kW PMSM demonstrate the feasibility of low-cost MAEs for achieving high-performance field-oriented control (FOC) of PMSMs in EV drives.

Index Terms — Calibration procedure, electric vehicle (EV), magnetic analog encoder (MAE), permanent magnet synchronous machine (PMSM), phase-locked loop (PLL), polynomial approximation (PA), position-error compensation.

2.1 Introduction

In order to perform field-oriented control (FOC) of permanent-magnet synchronous machines (PMSMs), the orientation of the rotor flux generated by the permanent magnets must be known. This variable is indirectly measured by absolute rotary position sensors such as resolvers and encoders attached to the machine shaft. In electric vehicle (EV) applications, the performance of such sensors is highly demanding because the rotor position measurement is directly related to the torque quality produced by the PMSM. Given that even a costly high-quality encoder or resolver with remarkable resolution, precision, and accuracy and based on any operating principle will present an inherent periodic position error due to different causes (Hanselman, 1990; Lara and Chandra, 2014b; Lin et al., 2011) including the nonideal mechanical mounting of their components on the machine, thus the use of low-cost rotary position sensors improved with efficient position-error compensation algorithms is strongly attracting the attention of academic researchers and industry professionals.

Over the past years, different radial and axial configurations of low-cost linear Hall-effect sensors have been proved to be effective for providing high-resolution and accurate rotor position measurements (Hu et al., 2012; Wu et al., 2014) including electromechanical braking systems (EMB) (Choi et al., 2015), vacuum pumps (Jung and Nam, 2011), and

PMSM integrated starter generators (ISG) for hybrid electric vehicle (HEV) applications (Chen et al., 2007).

The main nonidealities found in the quadrature analog signals from these position sensors must be fairly compensated in order to achieve a high-performance application. Over the past years, interesting online compensation algorithms have been devised to counteract this issue: iterative optimization algorithm (IOA) (Lara and Chandra, 2014b), Kalman filter (KF) (Hu et al., 2012), adaptive notch filter (ANF)-phase-locked loop (PLL) (Jung and Nam, 2011), self-adaption Kalman observer (SAKO) (Shi et al., 2015), autotuning filter (AF) (Qamar et al., 2015), artificial neural networks (ANN) (Kok Kiong and Kok-Zuea, 2005), adaptive ellipse fitting (AEF) (Hoseinnezhad et al., 2007), advanced adaptive digital (AAD)-PLL (Hoang and Jeon, 2011), decoupled double synchronous reference frame (DSRF)-PLL (Bergas-Jan et al., 2012; Xu et al., 2012), gain-phase-offset-correction (GPOC) (Bunte and Beineke, 2004; Faber, 2012), probabilistic learning (Kavanagh, 2001), Fourier analysis (Aksenenko and Matveyev, 2005; Ramakrishnan et al., 2013), and some other special methods (Hwang et al., 2011; Hwang et al., 2010; Mok et al., 2007). In contrast to the online correction algorithms, the static calibration methods are less prone to undergo instability conditions that can unexpectedly lead to dangerous scenarios in a real EV on the road. A traditional static calibration consists in a compensating look-up table (LUT) (Hagiwara et al., 1992; Hanselman, 1991; Ju-Chan et al., 2006; Lin et al., 2011; Tan et al., 2002) that generally stores either the position error or the direct mapping of the measurement from the position sensor under test to the reading of a high accuracy encoder. A better error compensation is possible by increasing the LUT resolution. Nevertheless, the larger amount of memory required to store the data is a tradeoff in embedded applications running on low-cost digital signal processors (DSP), where hardware resources are quite limited.

In this paper, the authors present a novel algorithm for compensating the position error in magnetic analog encoders (MAE) used in PMSMs intended for EV propulsion. The proposed algorithm based on polynomial approximations (PA) quite reduces the size of the required read-only memory (ROM) in comparison with a very high-resolution calibration LUT. The

use of polynomials allows compensating every possible input rotor position without carrying out an interpolation or a quantization operation. Advantageously, the polynomial coefficients are deduced from a calibration procedure that does not require an accurate and high-resolution position sensor for comparison and error-calculation purposes.

This paper is organized as follows. Section 2.2 presents an extended and generalized mathematical model of the position error caused by the main nonidealities found in quadrature analog encoders. In section 2.3, the calibration procedure and the proposed PA compensation algorithm are explained in detail. The experimental results obtained from the calibration procedure and the proposed compensation algorithm assisted with a type-2 PLL are shown in section 2.4. The experimental validation with a TM4 EV drive controlling an 80 kW PMSM is presented in section 2.5. Finally, the conclusion and some important remarks are given in section 2.6.

2.2 Modeling of the encoder position error due to different nonidealities

The rotor position error produced by the main nonidealities contained in the quadrature signals from analog encoders and resolvers has been investigated previously in (Hanselman, 1990; 1991; Hwang et al., 2011; Lara and Chandra, 2014b; Lin et al., 2011; Nasiri-Gheidari and Tootoonchian, 2015; Ramakrishnan et al., 2013). The contribution of this study to the literature on this subject is an extended and more accurate modeling of the position error. The set of equations presented in this paper has been derived considering the general case when the nonidealities are contained in both quadrature signals as well as when the amplitude of the harmonics in the sine and cosine waveforms is different.

The following theoretical analysis of the encoder position error is based on the type-2 PLL of Figure 2.1. Both the linear and nonlinear PLL structures are used for deriving the equations that model the position error. For analysis and design purposes, the simplifying locked condition of the linearized PLL scheme is considered (Harnefors and Nee, 2000).

The loop filter (LF) error E is composed by the phase detector (PD) error e and the disturbance input η that represents the position error from the encoder (Jung and Nam, 2011)

$$E = e + \eta \tag{2.1}$$

The error e is calculated as the difference between the real input position θ and the estimated output position θ' as

$$e = \theta - \theta' \tag{2.2}$$

The speed compensation term ω_r provides a feedforward path to the estimated rotor speed ω' for reducing the dc component of e that arises during acceleration and deceleration.

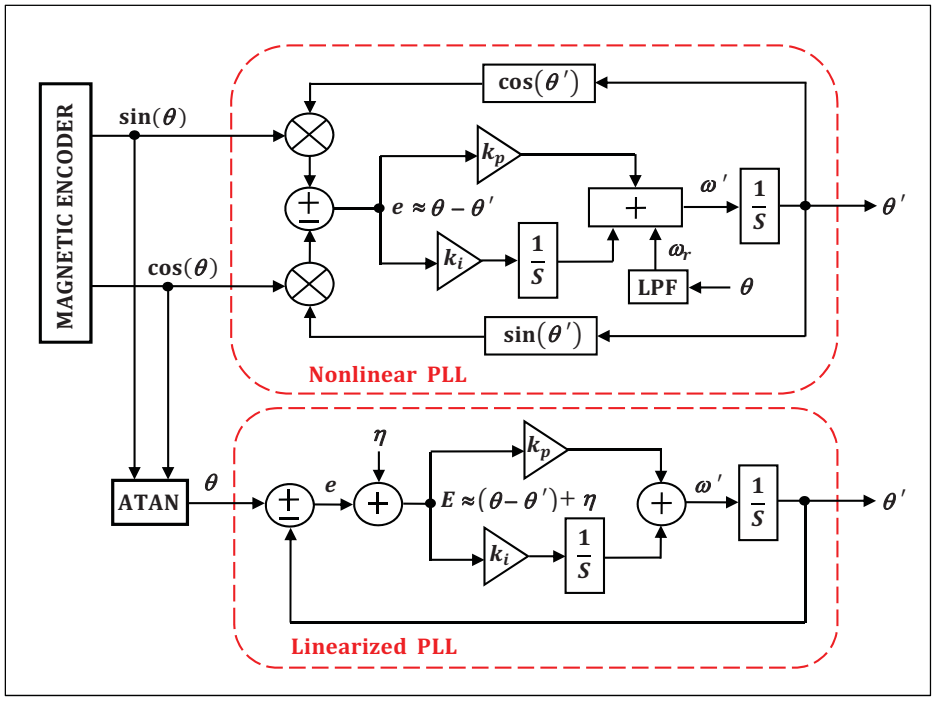

Figure 2.1 Nonlinear and linearized PLL structures used for deriving the position-error expressions that result from the nonidealities of the encoder signals

The deduction of the equations that model the position error due to the different nonidealities begins considering the ideal quadrature signals V_s and V_c from a perfect encoder as

$$V_{\mathrm{s}} = V_{\mathrm{in}} \cdot \sin(\theta) \tag{2.3}$$

$$V_{\mathrm{c}} = V_{\mathrm{in}} \cdot \cos(\theta) \tag{2.4}$$

where the amplitude V_{in} expressed in per unit (PU) is equal to the unity. When the encoder signals (2.3) and (2.4) are input to the PLL of Figure 2.1, the resulting error E is given by (Hanselman, 1990; Harnefors and Nee, 2000)

$$E = V_{\mathrm{in}} \cdot [\sin(e)] \tag{2.5}$$

The action of the PI controller found inside the PLL reduces the error E in (5) to a zero value in steady state. Hence, the equivalent position error e is also taken to zero. In this ideal case and under nonacceleration conditions, the PLL properly tracks the input rotor position. Nevertheless, when nonidealities are present in the quadrature encoder signals, e.g., amplitude mismatch, nonzero dc offset, nonorthogonality, or harmonic distortion, the error e is no longer reduced to zero even when the loop error E is zero. The error expression e that results from these nonidealities is mathematically deduced below.

2.2.1 Amplitude mismatch

The different sensitivity of the Hall-effect elements located inside the chip sensor, the unequal electronic amplification of the encoder signals due to the tolerance of the components used in each circuitry path, and the sensor tilt with respect to the axial plane of the magnetic target produce a pair of quadrature signals U_{s} and U_{c} with a different amplitude. This nonideality is modeled as

$$U_{\mathrm{s}} = V_{\mathrm{in}} \cdot (1 + B_1) \cdot \sin(\theta) \tag{2.6}$$

$$U_c = V_{in} \cdot (1 + A_1) \cdot \cos(\theta) \tag{2.7}$$

The equivalent Lissajous figure from (2.6) and (2.7) is not the ideal circle but an ellipse (Lara and Chandra, 2014b). The resulting error due to this amplitude imbalance is a second harmonic of the rotor position

$$e \approx \left(\frac{A_1 - B_1}{2}\right) \cdot \sin(2\theta) \tag{2.8}$$

2.2.2 Nonzero dc offset

The magnetic offset exhibited by the magnet due to tolerance limitations in the magnetization process, the dc offset drift dependent on temperature, and the residual dc offset inherent to the Hall-effect sensors technology cause the presence of a dc component in the quadrature encoder signals mathematically described as

$$U_s = V_{in} \cdot [\rho + \sin(\theta)] \tag{2.9}$$

$$U_c = V_{in} \cdot [\delta + \cos(\theta)] \tag{2.10}$$

The effect on the Lissajous figure is a displacement of the circle out of the origin (Lara and Chandra, 2014b). The resulting error is given by

$$e \approx \delta \cdot \sin(\theta) - \rho \cdot \cos(\theta) \tag{2.11}$$

If the special condition $\delta = \rho = k_0$ is fulfilled, then (2.11) is simplified to (Hanselman, 1990; Lara and Chandra, 2014b; Lin et al., 2011)

$$e \approx -\sqrt{2} \cdot k_0 \cdot \cos\left(\theta + \frac{\pi}{4}\right) \tag{2.12}$$

2.2.3 Nonorthogonality

The imperfect geometric quadrature placement of the Hall-effect elements in the integrated circuit (IC) sensor during the chip-building process, the unequal delay undergone by each encoder signal along the entire circuitry paths, and the nonideal magnetization of the magnetic target affect the orthogonality between the sine and cosine waveforms now modeled as

$$U_{\mathrm{s}} = V_{\mathrm{in}} \cdot [\sin(\theta + \varphi)] \tag{2.13}$$

$$U_{\mathrm{c}} = V_{\mathrm{in}} \cdot [\cos(\theta + \zeta)] \tag{2.14}$$

The Lissajous figure is accordingly transformed from a circle into a rotated ellipse (Lara and Chandra, 2014b). The general equation that describes the position error generated by the nonideal orthogonality is

$$e \approx -\left(\frac{\zeta + \varphi}{2}\right) + \left(\frac{\zeta - \varphi}{2}\right) \cdot \cos(2\theta) \tag{2.15}$$

Before evaluating (2.15), the phase-shift of the signal considered as the reference has to be set to zero, i.e., $\zeta = 0$ or $\varphi = 0$.

2.2.4 Harmonic distortion

The saturation of the electronics found inside the chip sensor and the nonhomogeneity of the magnetic field lines along the linear range of the magnet cause the analog encoder signals to contain harmonic distortion. The xy static and dynamic misalignment between the Hall-effect elements array center, the magnet midpoint, and the rotational axis of the machine shaft can also take the encoder to work in the nonlinear range of the magnet, thus leading to distorted output waveforms. The general model presented in this study considers the magnitude of the harmonics contained in each signal to be different. Thereby, the distorted sine–cosine signals expressed as a Fourier series with N terms are

$$U_{\mathrm{s}} = V_{\mathrm{in}} \cdot \left[\sum_{m=1}^{N} (1 + B_m) \right] \cdot \sin(m\theta) \tag{2.16}$$

$$U_{\mathrm{c}} = V_{\mathrm{in}} \cdot \left[\sum_{m=1}^{N} (1 + A_m) \right] \cdot \cos(m\theta) \tag{2.17}$$

By using some trigonometric identities and considering $\cos(e) \approx 1$, $\sin(e) \approx e$, and $A_1 = B_1 = 0$, the position error due to the harmonic distortion is accurately modeled by

$$e \approx \frac{\sum_{m=2}^{N} [(1 + A_m) \cdot \cos(m\theta) \cdot \sin(\theta) - (1 + B_m) \cdot \sin(m\theta) \cdot \cos(\theta)]}{1 + \sum_{m=2}^{N} [(1 + A_m) \cdot \cos(m\theta) \cdot \cos(\theta) + (1 + B_m) \cdot \sin(m\theta) \cdot \sin(\theta)]} \tag{2.18}$$

If the harmonics are disregarded and only the first term of the summations in (2.16) and (2.17) is taken into account, then the position error due to the amplitude mismatch of the quadrature fundamental components is modeled as

$$e \approx \frac{(A_1 - B_1) \cdot \sin(\theta) \cdot \cos(\theta)}{A_1 \cdot \cos^2(\theta) + B_1 \cdot \sin^2(\theta) + 1} \tag{2.19}$$

This expression is a more accurate approximation than (2.8).

2.3 Calibration procedure in PMSMs and PA compensation algorithm

This section presents the details of the investigated calibration procedure for MAEs mounted on PMSMs and the proposed compensation algorithm based on PA that is capable of fairly compensating all the errors described in sections 2.2.1-2.2.4.

2.3.1 Calibration procedure in PMSMs

The voltage–frequency (V/f) control is a type of scalar control characterized by an open-loop structure that does not require the rotor position or speed information for operation. This sensorless algorithm is implemented in PMSMs when high-performance dynamics is not required, e.g., pumps, blowers, fans, compressors (Consoli et al., 2013; Moldovan et al., 2011; Perera et al., 2003; Sala-Perez et al., 2013), or in very high-speed applications, where mechanical sensors are unsuitable (Ancuti et al., 2010; Longya and Changjiang, 1998). An optimal V/f control requires a well-designed reference speed curve and the inclusion of stabilizing loops for avoiding overcurrent, instability and loss of synchronism triggered by heavy load starting torques, load steps changes or high acceleration and speed rates. In steady-state conditions, the natural stable operation is reached as the PMSM approaches the low rotor-speed region. Under these circumstances, the V/f control is capable of rotating the PMSM shaft at a very accurate constant speed without the need of measuring the rotor position. This singularity of the V/f scalar control has been exploited in this paper for calibration purposes of a quadrature analog magnetic encoder that provides rotor-position feedback in a FOC-PMSM drive.

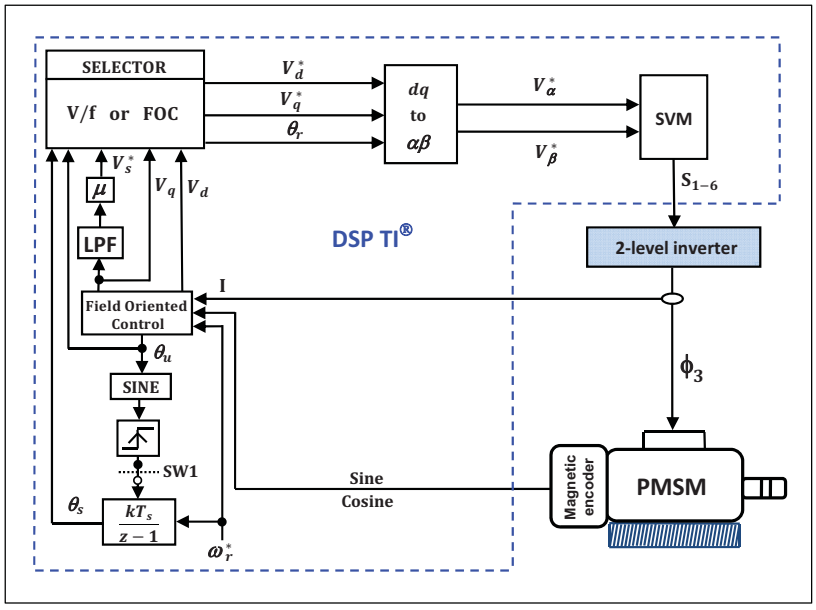

Figure 2.2 Schematic diagram sketching the implementation of the calibration procedure in PMSMs

The implementation of the proposed calibration procedure schematically sketched in Figure 2.2 is explained below. After mounting the magnetic encoder on the PMSM, the rotor-position offset θ_{offset} between the zero of the encoder measurement and the physical orientation of the rotor magnetic flux axis "$+d$" must be corrected. For this aim, the two methods proposed in (Rahman and Hiti, 2005) have been implemented. In spite of the periodic position error from the encoder, the PMSM drive is started-up using FOC. An electrical speed reference of 16 Hz equivalent to ω_r^* = 240 mechanical r/min has been set in the speed closed-loop implementation. Because of the error contained in the rotor position and speed measurements fed back to the FOC algorithm, the real speed of the machine shaft oscillates around the desired value. However, the reference speed ω_r^* and the mean μ of the low-pass filtered (LPF) q-axis voltage V_q provide a very good approximation $V_s{}^*/\omega_r^*$ of the flux required to guarantee stability when switching to the V/f scalar control. This stable state is reached given that the most important particular conditions of the system such as starting load torque, friction, and inverter nonlinearities have been already considered by the FOC. The transition from FOC to V/f control is carried out online by keeping $V_d^* = V_d = 0$ and replacing the voltage reference $V_q{}^* = V_q$ with $V_q{}^* = V_s{}^*$, and the rotor position from the uncalibrated encoder θ_u with a synchronized ideal ramp signal θ_s . The resulting V/f control rotates the PMSM shaft, and therefore, the magnetic target sensed by the encoder at a very accurate constant speed, thus making possible a high-quality identification of the error signals that contain the nonidealities to compensate.

2.3.2 PA compensation algorithm

From the calibration procedure explained in section 2.3.1, once the PMSM rotor speed is being regulated using the V/f control algorithm, one second of the uncompensated sine–cosine encoder signals sampled at a rate of 10 kHz is captured by the DSP. The error signals that contain the nonlinear distortion (NLD) to compensate are then deduced by subtracting the raw signals to a pair of ideal waveforms digitally synthesized. The next step consists in cutting these error signals piecewise at each quadrant intersection and then applying a PA based on the least mean squares (LMS) method to each of the resulting segments for finding

the coefficients of the n-order polynomial $\Phi_{xy}(\theta_{ux})$ that best fits each of the input data arrays $\bar{P}_{xy}$. The subscripts "x" and "y" stand for the quadrant number and either the sine or cosine NLD, respectively. In order to improve the numerical properties of both the polynomial and the fitting algorithm, the following centering and scaling transformation is applied to every input sample i of the uncompensated but normalized rotor position θ_u in each quadrant x as follows

$$\theta_{vx}(i) = \frac{\theta_{ux}(i) - \mu[\,\bar{P}_{xy}]}{\vartheta\,[\,\bar{P}_{xy}]} \tag{2.20}$$

where μ and ϑ are the mean and standard deviation of a given error signal segment P_{xy} . As the number of segments increases, the formed segments along the sine and cosine error signals are each time closer to a straight line. This implies that for a higher number of segments, a lower order of the polynomials is enough to represent the NLD contained in the uncompensated encoder signals. On the other side, if the number of segments decreases, then higher order polynomials are required for accurately following all of the variations present in the error signals. The selection of the number of segments s and the order n for the PA is done bearing in mind the existing tradeoff between the total harmonic distortion (THD) of the sine and cosine encoder signals after the PA compensation, the peak value of the compensated position error, the number of ROM coefficients stored in the DSP, and the total execution time of the PA algorithm.

In Figure 2.3, it can be observed the nonlinear relation among these variables as a function of s and n. The operating point selected in this study is pointed out with the dashed circle and corresponds to s = 4 and n = 5. Given that the number of segments is four, thus a total of eight PAs have been applied to both quadrature error signals. For this, each array $\bar{P}_{xy}$ is approximated as a function of the centered and scaled rotor position array $\overline{\theta}_{vx}$. The resulting matrix from the evaluation of these PAs for either the sine or cosine encoder signal is expressed as

$$\overline{\Phi}_y = [\overline{K}_y]\cdot[\overline{\theta}_p]^T \tag{2.21}$$

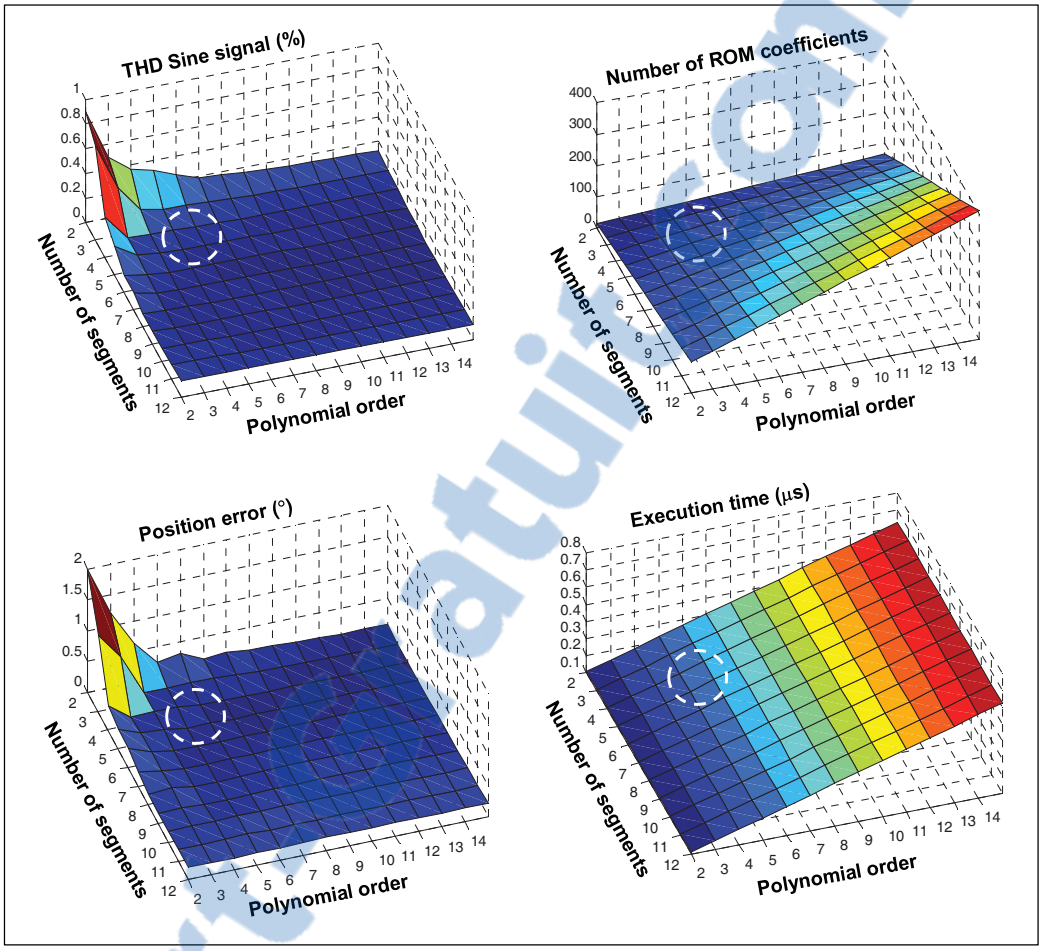

Figure 2.3 Performance of the PA algorithm as a function of the number of segments s and the polynomial order n. The dashed circle points out the selected operating point

The matrix for every transformed rotor-position sample evaluated at $n + 1$ different powers is

$$\overline{\theta}_p = \begin{bmatrix} \theta_{v1}^n & \theta_{v1}^{n-1} & \dots & \theta_{v1}^2 & \theta_{v1} & 1 \\ \theta_{v2}^n & \theta_{v2}^{n-1} & \dots & \theta_{v2}^2 & \theta_{v2} & 1 \\ \theta_{v3}^n & \theta_{v3}^{n-1} & \dots & \theta_{v3}^2 & \theta_{v3} & 1 \\ \theta_{v4}^n & \theta_{v4}^{n-1} & \dots & \theta_{v4}^2 & \theta_{v4} & 1 \end{bmatrix} \tag{2.22}$$

while the matrix containing the polynomial coefficients for either the sine or cosine signal is defined as

$$\overline{K}_y = \begin{bmatrix} k_{1(n)} & k_{1(n-1)} & \dots & k_{1(2)} & k_{1(1)} & k_{1(0)} \\ k_{2(n)} & k_{2(n-1)} & \dots & k_{2(2)} & k_{2(1)} & k_{2(0)} \\ k_{3(n)} & k_{3(n-1)} & \dots & k_{3(2)} & k_{3(1)} & k_{3(0)} \\ k_{4(n)} & k_{4(n-1)} & \dots & k_{4(2)} & k_{4(1)} & k_{4(0)} \end{bmatrix} \tag{2.23}$$

Each of the rows of $\overline{K}_y$ represents a given quadrant. From (2.20) and (2.23), it can be deduced that the total number of coefficients stored in the DSP memory is $2s(n+2)$. Given that only the multiplications between coefficients in the same row of (2.22) and (2.23) are valid operations, (2.21) is simplified to a diagonal matrix. By remarking that three of the rows in (2.22) are zero during each polynomial evaluation since only one quadrant is active at a time, thus the original matrix $\overline{\Phi}_y$ finally becomes a column vector with just one nonzero element that will compensate for the nonideal encoder signal input sample. The exemplification of the polynomial evaluation carried out for the first quadrant is as follows

$$\Phi_y = k_{1(n)} \cdot \theta_{v1}^{n} + k_{1(n-1)} \cdot \theta_{v1}^{n-1} + \cdots\cdots + k_{1(2)} \cdot \theta_{v1}^{2} + k_{1(1)} \cdot \theta_{v1} + k_{1(0)} \tag{2.24}$$

In the DSP implementation, (2.24) is computed in real time by just multiplying a row of (2.23) with a column of the transposed of (2.22). Note that the coefficients from $k_{1(0)}$ to $k_{1(n)}$ are deduced considering concurrently all of the nonidealities contained in the encoder signals. The above example is only for the first quadrant. However, the same principle applies for the rest of the quadrants in either of the two encoder signals as well as for any nonideality.

In order to unload the DSP from unnecessary calculations, solely the $(4n)$ multiplications and the $(2n + 4)$ additions required by the PA algorithm based on (2.20)–(2.26) are computed in real time. Considering that the on-chip random access memory (RAM) of the DSP performs 1 instruction per clock cycle, the time it takes to execute the compensation algorithm is $(6n + 4) / f_{clk}$, where f_{clk} is the clock frequency of the processor.

The compensated signals V_s' and V_c' are obtained by adding the compensating value Φ_s and Φ_c that results from the polynomial evaluation in (2.21) to the uncompensated input samples of the voltage waveforms U_s and U_c , respectively

$$V_s' = U_s + \Phi_s \tag{2.25}$$

$$V_c' = U_c + \Phi_c \tag{2.26}$$

The calibration procedure and the proposed PA compensation algorithm are synthesized in the flowchart of Figure 2.4, whereas the DSP implementation is schematically sketched in Figure 2.5.

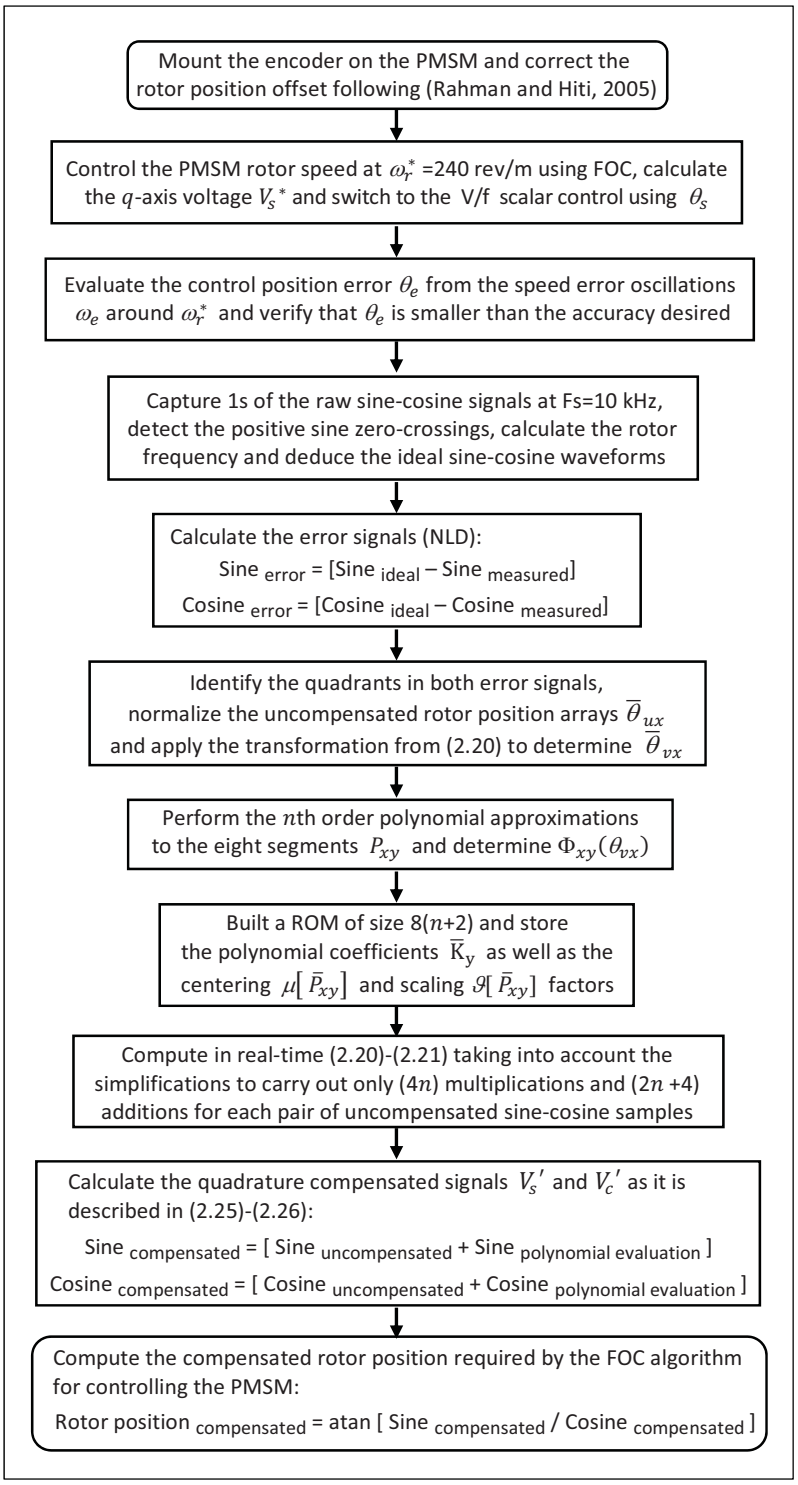

Figure 2.4 Flowchart showing the steps of the calibration procedure in PMSMs as well as of the proposed algorithm based on PA for compensating the rotor position error in analog magnetic encoders

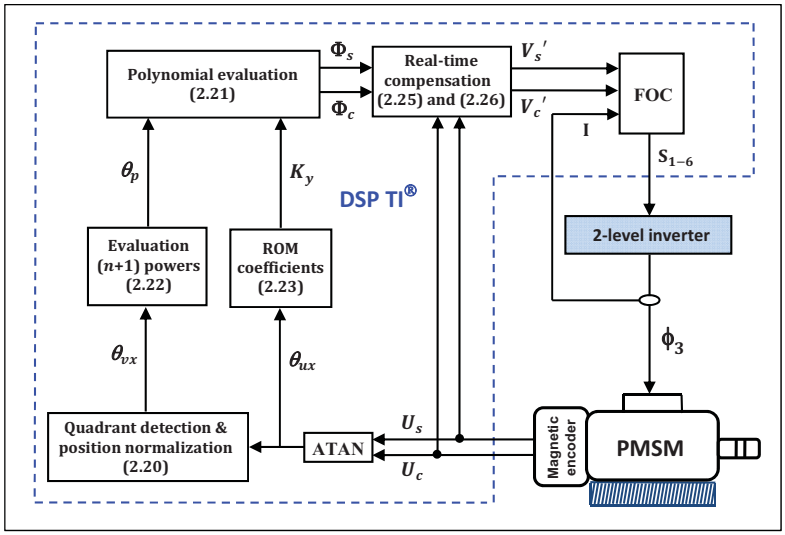

Figure 2.5 Schematic diagram sketching the DSP implementation of the proposed PA compensation algorithm

2.4 Experimental results

The rotor-position-sensing prototype used in the experiments is composed of the elements shown in Figure 2.6. The application-specific integrated circuit (ASIC) is a contactless encoder based on Hall-effect sensors that translate the angular position of a simple two-pole magnet into a pair of sine–cosine analog voltage signals.

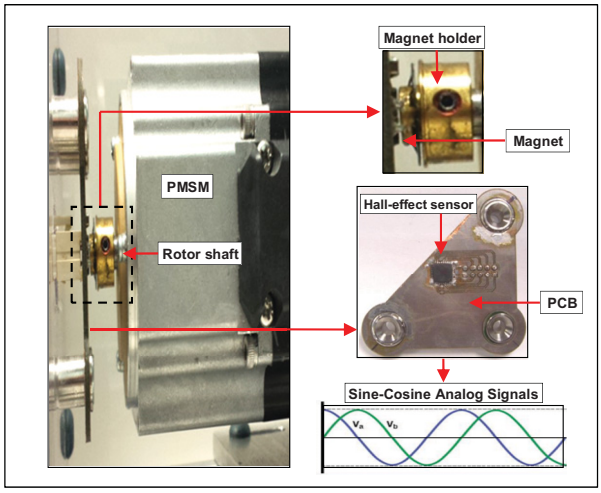

Figure 2.6 Rotor-position-sensing prototype mounted on a three-phase PMSM. The magnet, its holder, and the PCB hosting the Hall-effect IC sensor are shown in this photograph

The magnetic encoder has been mechanically mounted on a three-phase PMSM, while a high-resolution incremental optical encoder providing 10 000 counts/turn has been attached to the rotor shaft of another three-phase PMSM. Both PM machines were tightly coupled and carefully aligned in the same rotational axis, so that the position-error measurement obtained by comparing the reading of the two encoders prevails accurate and reliable in the whole speed range of the tests. The block diagram of the complete experimental test bench built for evaluating the calibration procedure and the proposed PA compensation algorithm is shown in Figure 2.7.

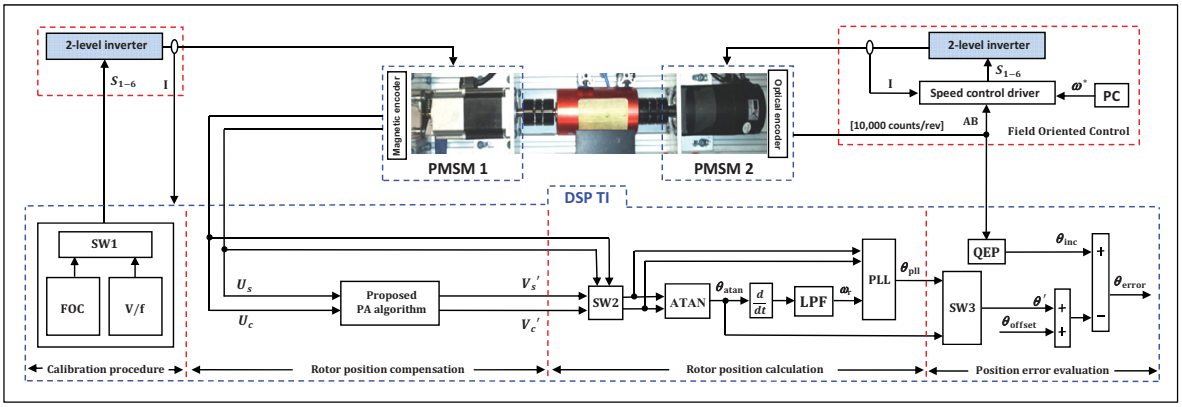

Figure 2.7 Block diagram of the complete experimental test bench used for evaluating the calibration procedure and the proposed PA compensation algorithm

By selecting the position of switch SW3, the rotor position from the optical encoder can be compared to the rotor-position angle obtained by means of either the evaluation of the arctangent function or using a type-2 PLL with speed feedforward compensation. In turn, the SW2 allows applying each of these methods to either the uncompensated raw sine–cosine signals or the compensated signals obtained after applying the proposed PA algorithm. The speed feedforward compensation term ω_r is obtained by low-pass filtering the derivative of the rotor position θ_{atan} as it is depicted in the rotor-position calculation section of Figure 2.7. In order to provide a high-quality speed feedforward compensation, the speed oscillations coming from the rotor position error have been fairly attenuated by using a first-order LPF with a cut-off frequency fc of 10 Hz.

The FOC and the V/f scalar control of the calibration procedure, the PA compensation, the rotor-position calculation, and the position-error evaluation have been implemented to work in real time at 50 μs time step using the DSP TMS320F28335 from Texas Instruments.

2.4.1 Calibration and PA compensation

The position and speed-control errors obtained during the online transition from FOC to V/f control are shown in Figure 2.8. It can be observed how their peak values are notably reduced from 7.5° and 9 r/min to less than 1.5° and 1 r/min, respectively. The high rotor-speed accuracy achieved through the V/f control allows limiting the frequency variation of the sine–cosine encoder signals to a negligible value confined to the range of ±0.017 Hz.

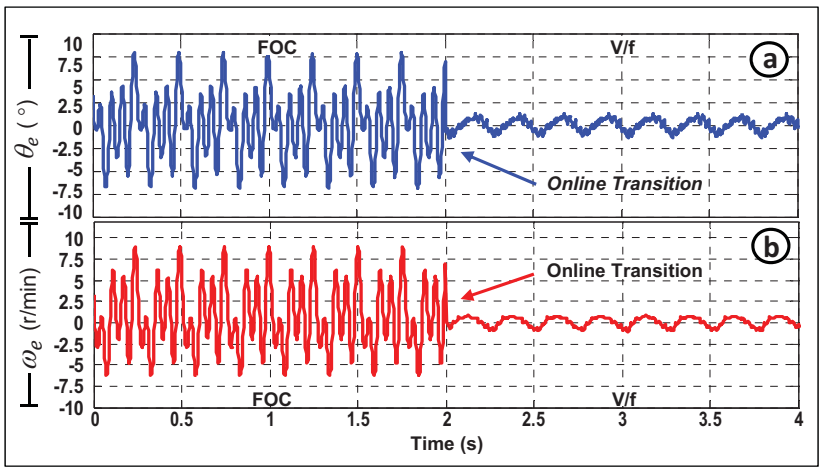

Figure 2.8 Experimental results obtained during the online transition from FOC to V/f control (a) Electrical rotor position-control error θ_e (b) Mechanical speed-control error ω_e

The quadrature encoder signals before and after the compensation as well as the periodic waveforms obtained from the PAs are shown in Figure 2.9. It can also be observed the four segments P_{1s} , P_{2s} , P_{3s} , P_{4s} identified in the sine error signal and the four segments P_{1c} , P_{2c} , P_{3c} , P_{4c} identified in the cosine error signal. Note that the PA signals plus the sine and cosine waveforms before the compensation are equal to the sine and cosine signals after the compensation.

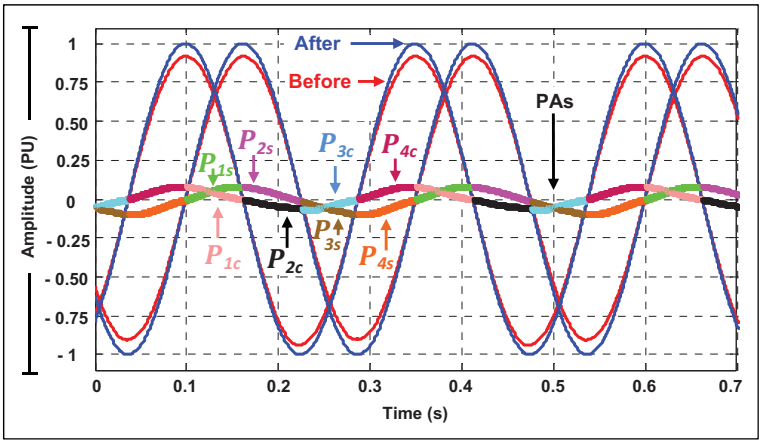

Figure 2.9 Experimental results: sine and cosine encoder signals before and after the PA compensation. The identification of the P_{xy} segments along one period of the error signals is also shown

The harmonic spectra of the quadrature encoder signals before and after the compensation are shown in Figure 2.10. It can be observed that after applying the proposed PA algorithm, the DC offsets as well as the harmonics are reduced to less than 2 mPU, the THD is decreased below 0.3% and the nonorthogonality is compensated from −0.17° to +0.02°. Since the magnitude of the fundamental components becomes very close to unity, the nonideality of amplitude mismatch is now negligible.

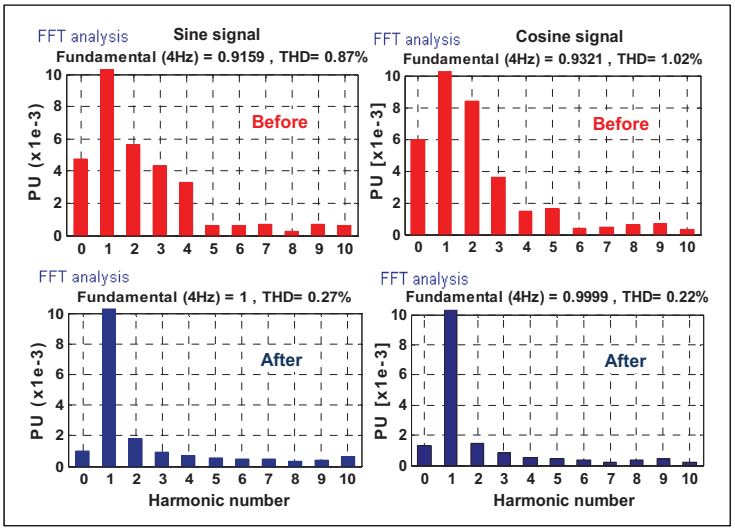

Figure 2.10 Experimental results: harmonic spectra and THD of the sine and cosine encoder signals before and after the compensation

Given that fifth-order PAs were applied to the four segments of each error signal, thus the total number of coefficients stored in the DSP memory is 56. Likewise, the number of fixed-point operations computed in real time comprises only 20 multiplications and 14 additions. Therefore, the F28335 TI processor that operates with f_{clk} = 150 MHz executes the proposed PA compensation algorithm in ≈ 0.23 µs.

The correction effects of the compensation algorithm are readily observed in Figure 2.11. It is noteworthy that by using the investigated calibration procedure and the proposed PA algorithm, the position error is reduced from ±0.8° to less than ±0.2 mechanical degrees.

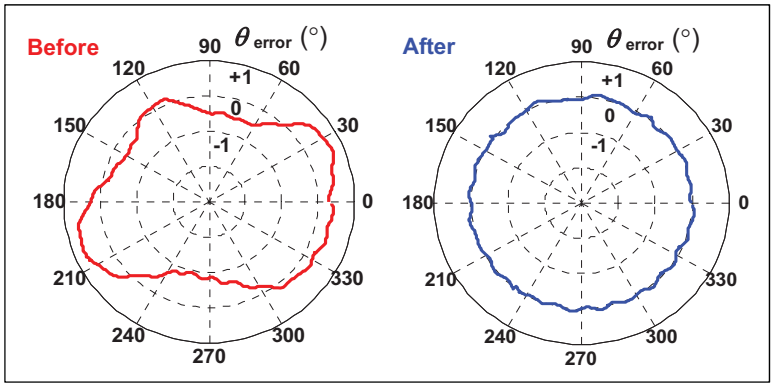

Figure 2.11 Experimental results: rotor position error displayed in a ring shape (Left) Before the compensation (Right) After the compensation

2.4.2 Rotor position error as a function of the PMSM speed

The rotor position error obtained after applying the PA algorithm has been measured in the whole operating speed range of the PMSM following the trapezoidal motion profile presented in Figure 2.12 c). The maximum speed and constant acceleration rates have been set to ±5000 r/min and ±1000 r/min/s^2, respectively. In Figure 2.12 d), it can be observed how the PA algorithm reduces the rotor position error from ±4.3° to ±1.6 electrical degrees and how it remains inside this range along the entire speed for both rotation directions, thus demonstrating the validity of the proposed static compensation under different dynamic conditions.

The use of a PLL processing the sine–cosine encoder signals previously compensated with the PA algorithm not only helps to reduce the remaining position error in the high speed range of the PMSM but will contribute to reject the high-frequency spikes induced in the encoder signals during commutation of the inverter. The high-rate input variations are fairly attenuated by the inherent low-pass filter (LPF) response of the PLL structure (Emura and Lei, 2000). Figure 2.12 e) shows the performance improvement of the PA algorithm through a type-2 PLL with speed feedforward compensation. It can be noted how the high-frequency components from the encoder signals are attenuated by the loop filter of the PLL allowing to reduce the total position error to less than ±1°. The analysis and design of the PLL are presented in the Appendix I.

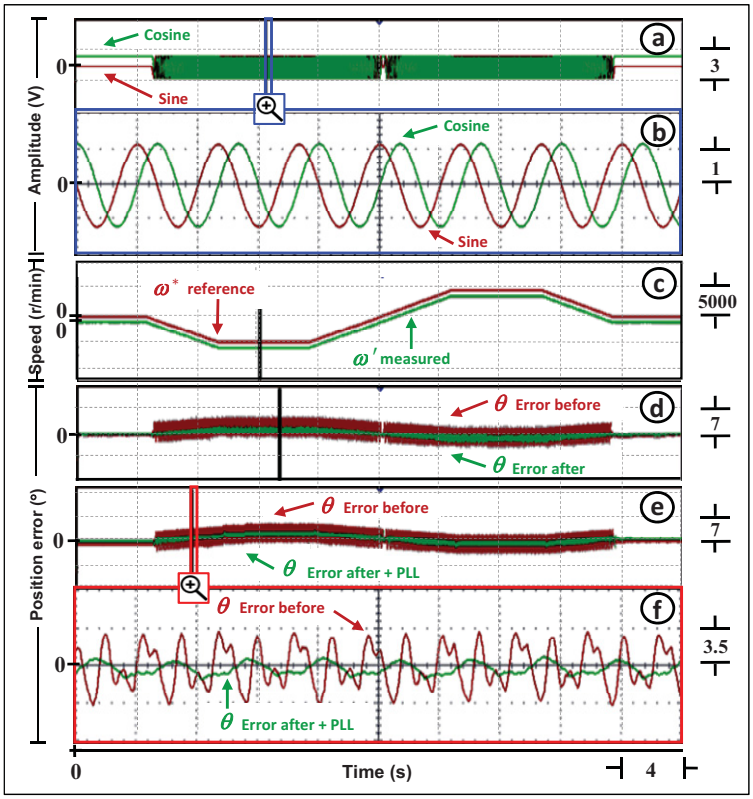

Figure 2.12 Experimental results: dynamic performance of the PA compensation algorithm and improvement through a PLL a) Quadrature signals from the magnetic encoder b) Zoom-in 450x of (a) c) Speed profile d) Position error before and after the compensation e) Position error after the compensation and using the PLL f) Zoom-in 200x of (e) during acceleration

2.5 Validation with 80 kW PMSM

The investigated calibration procedure and the proposed PA compensation algorithm have also been validated with a commercial EV drive controlling an 80 kW PMSM both designed and manufactured by TM4 Electrodynamic Systems. Figure 2.13 shows the rotor-position-sensing prototype mounted on the machine, while Figure 2.14 shows the experimental setup built at TM4 facilities.

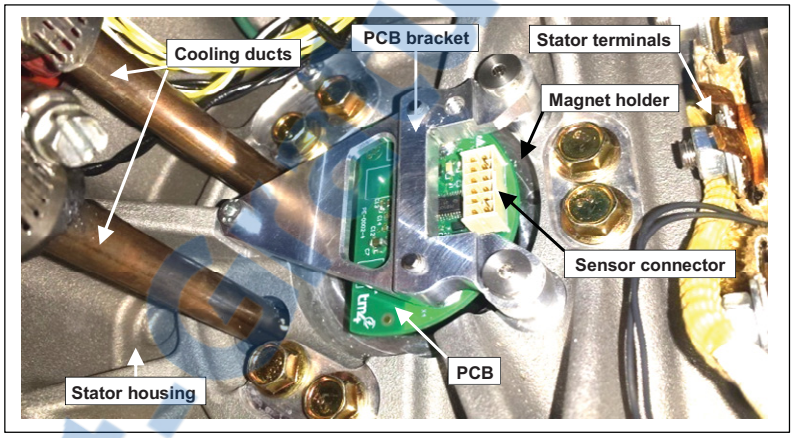

Figure 2.13 Mechanical mounting of the rotor-position-sensing prototype on the 80 kW PMSM. The PCB bracket, the magnet holder, and the PCB hosting the Hall-effect IC sensor are shown in this photograph

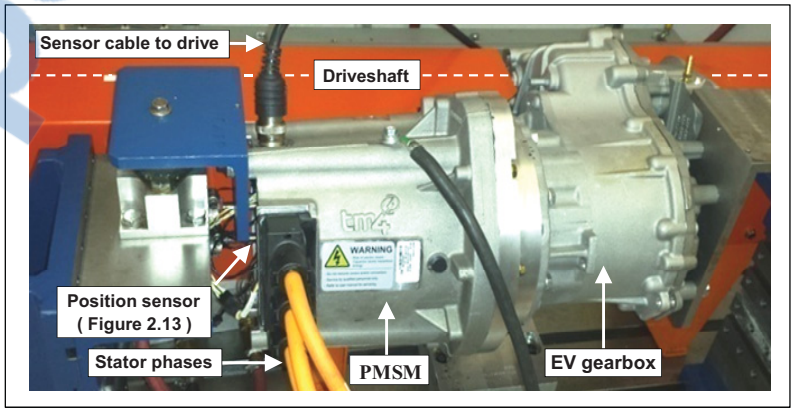

Figure 2.14 Experimental setup built at TM4. The rotor position sensor has been mounted on the back side of the 80 kW PMSM that in turn is coupled to the driveshaft of an induction machine by means of an EV gearbox

In order to evaluate the performance of the proposed PA compensation algorithm, two different tests were performed. The first test only considers the rotor position error from the encoder itself and that is produced by the nonidealities contained in the quadrature analog signals, whereas the second test evaluates the total position error including the EMI generated during the commutation of the inverter with a dc bus rated at 400 V and the flowing of stator currents of up to 300 A_{pk}.

In the tests, the induction machine is controlled in speed mode and the 80 kW PMSM in torque mode. The obtained results for both motoring and regenerative braking operation modes are shown in Figure 2.15. The normalized ramp rotor position (θ), the position error before (B) and after (A) the PA compensation as well as the position error obtained when using the PLL can be observed. At both speeds of 6000 and 9000 r/min and under no commutation conditions, the uncompensated position error varies between ±0.8 mechanical degrees, whereas after applying the proposed PA algorithm, this error is reduced to ±0.2°. When the machine develops the maximum torque of 85 Nm at 6000 r/min and ±55 Nm at 9000 r/min, the effects of the inverter commutation are readily observed. However, given that the nonidealities were previously well compensated with the PA algorithm, the high-frequency spikes are quite reduced by the loop filter of the PLL, thus allowing to achieve a total position error confined to a range as small as ±0.75 electrical degrees.

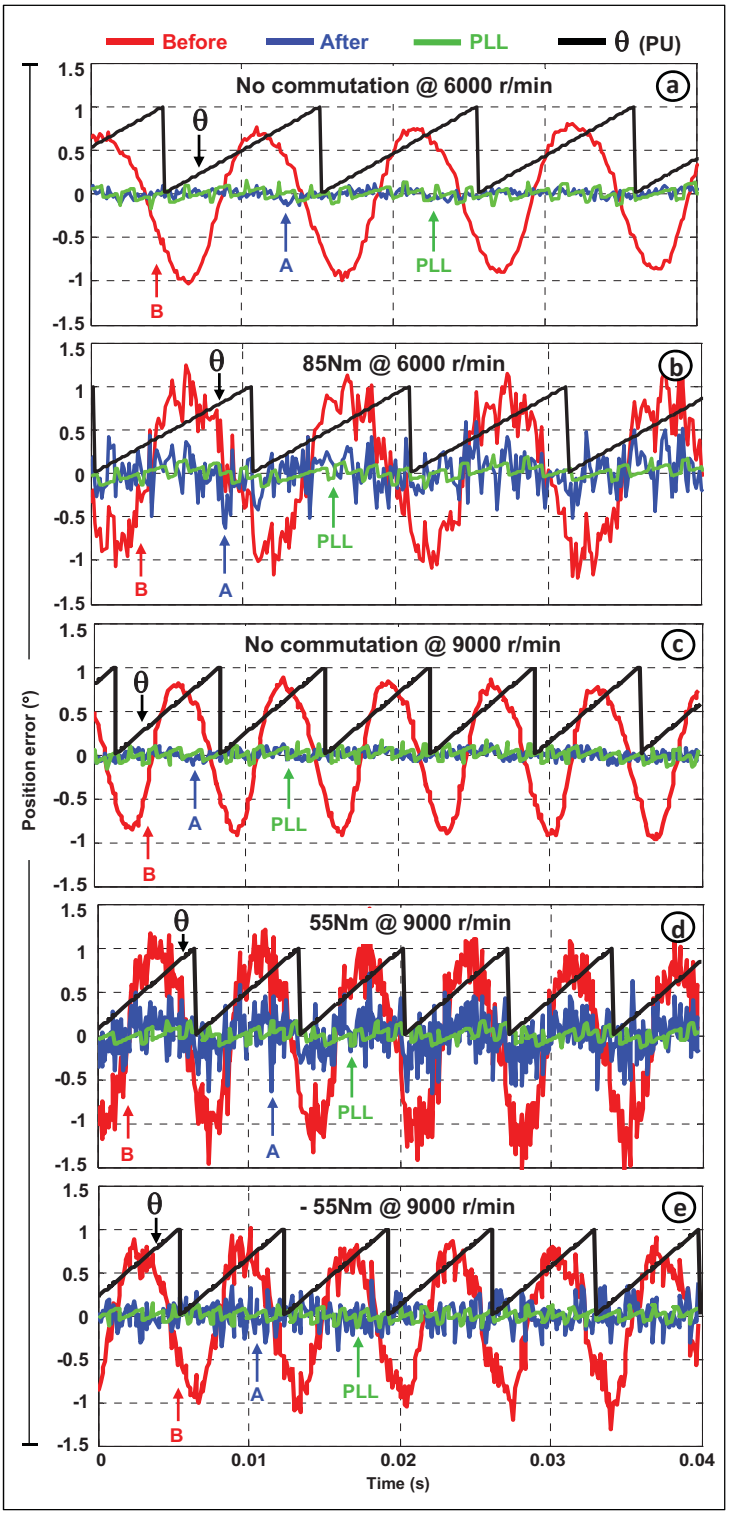

Figure 2.15 Experimental results: Rotor position error before and after the PA compensation as well as when using the PLL a), c) Under no commutation b), d), e) At maximum torque conditions

2.6 Conclusion

A novel algorithm based on PAs for an efficient error compensation of MAEs in PMSMs intended for EV propulsion has been presented in this paper.

The proposed algorithm fairly increases the rotor-position measurement accuracy without carrying out an interpolation or a quantization operation, and advantageously, it only requires storing 56 coefficients for a fifth-order approximation, thereby reducing in around 90% the memory resources required from the DSP compared to a typical high-resolution LUT of 512 points. The PA algorithm is quite efficient bearing in mind that solely 20 multiplications and 14 additions have to be executed in real time, thus consuming less than 0.25 μs of the DSP time step set for executing the FOC algorithm.

The position error of ±0.75 electrical degrees obtained with the TM4 EV drive controlling the 80 kW PMSM demonstrates that the proposed PA algorithm assisted with the type-2 PLL is a promising solution to compensate the position error of MAEs in PMSMs for EV applications.

2.7 Acknowledgment

The authors would like to thank Tony Coulombe, the Team Leader of the Electric and Power Electronics Group at TM4 Inc., for his support and counseling during the development of the project.

CHAPTER 3

EFFECTS OF ROTOR POSITION ERROR IN THE PERFORMANCE OF FIELD-ORIENTED-CONTROLLED PMSM DRIVES FOR ELECTRIC VEHICLE TRACTION APPLICATIONS

Jorge Lara [a], Jianhong Xu [b], Ambrish Chandra [c]

[a,c] Department of Electrical Engineering, École de Technologie Supérieure, 1100 Notre-Dame Ouest, Montréal, Québec, Canada H3C 1K3
[b] TM4 Electrodynamic Systems, 135 Joseph-Armand Bombardier, Boucherville, Québec, Canada J4B 8P1

Article published in « IEEE Transactions on Industrial Electronics » on August 2016.

Abstract

This paper analyzes the effects of the rotor position error in the performance of field-oriented-controlled permanent-magnet synchronous machine (PMSM) drives intended for electric vehicle (EV) traction applications. A special focus is given to the torque ripple generated along the characteristic trajectories in the different operating regions of the PMSM. An extended and generalized model of the torque ripple produced by the PMSM as a function of the rotor position error is analytically deduced. An infinite-speed interior-(I)PMSM drive and a finite-speed surface-mounted (SM)-PMSM drive are considered for the simulations carried out in MATLAB-SimPowerSystems. The experimental results have been validated with a TM4 EV drive controlling an 80-kW SM-PMSM. The torque ripple has been evaluated for both motoring and regenerative braking operation modes under maximum torque conditions going from 100 N · m at 1000 r/min up to 55 N · m at 9000 r/min. The obtained simulation and experimental results demonstrate the good accuracy of the proposed model for evaluating the torque ripple produced in PMSMs due to the error from the rotor position sensor.

Index Terms — Electric vehicle (EV), field-oriented control (FOC), permanent-magnet synchronous machine (PMSM), rotor position error, torque ripple.

3.1 Introduction

Rotor position error plays a very important role in high-performance field-oriented control (FOC) of permanent-magnet synchronous machines (PMSMs) intended for EV traction applications, where the maximum average torque with a minimum torque ripple is demanded over the entire operating speed range of the machine. Because of the inherent position error from the encoder or resolver attached to the PMSM shaft, the direct and quadrature stator currents deduced from the Park's transformation provide a mistaken feedback to the FOC algorithm; thus, producing real stator current vectors characterized by the unwanted effects of torque ripple and air-gap flux variations. Over the past years, different torque ripple minimization techniques roughly categorized into machine design and machine control have been proposed by academicians and industry professionals (Nakao and Akatsu, 2014). On the machine-control side, diverse algorithms based on repetitive control (Mattavelli et al., 2005), artificial neural networks (Flieller et al., 2014), resonant controllers (Xia et al., 2015; Yepes et al., 2015), fuzzy logic (Uddin, 2011), predictive control (Chai et al., 2013; Cho et al., 2015; Zhu et al., 2012), adaptive control (Mohamed and El-Saadany, 2008; Petrovic et al., 2000; Sencer and Shamoto, 2014), and iterative learning control (Weizhe et al., 2004; Weizhe et al., 2005) have been proved to be effective in reducing the amplitude of both torque and speed error oscillations in various PMSM applications. This kind of algorithms counteracts the global effect of numerous sources that contribute concurrently to the torque ripple generation, e.g., asymmetric stator phase resistance (Xu et al., 2014), nonsinusoidal air-gap flux density, rotor permanent-magnet field and stator slots interaction, imperfect current sensing, finite resolution of the pulse width modulation (PWM), among others (Gebregergis et al., 2015; Shaotang et al., 2002; Weizhe et al., 2004; Xu et al., 2014). However, the experimental results obtained in this study with two different PMSMs show that the torque oscillations caused by these sources are negligible compared to the torque ripple produced by just a few electrical degrees of error in the rotor position measurement.

Hence, authors propose in this paper an extended and generalized model of the torque ripple produced by the PMSM as a function of the rotor position error.

In the previous literature, the torque–speed characteristic curves of various IPMSMs have been analyzed considering different errors from the rotary position sensor (Chen et al., 2007; Hao et al., 2013; Rahman and Hiti, 2005). The obtained curves demonstrate how an inaccurate rotor position measurement leads to a severe degradation of the machine-drive performance and how in some cases, the resulting torque, power and efficiency reduction along the flux weakening (FW) region can reach unacceptable levels. For this reason also, this study mainly focuses on the inaccuracy of the position sensor for evaluating the overall performance of FOC PMSM-drives intended for EV applications.

Below the base speed, the influence of the rotor position error on the PMSM-drive performance is negligible. Nevertheless, it becomes increasingly important with rotor speed along the constant power region. Therefore, the performance analysis results are inherently correlated with the FW technique used for the simulations and the experimental tests. In the past, insightful techniques that increase the voltage utilization of the limited dc bus as well as effective and efficient FW algorithms have been devised to extend the PMSM-drives torque–speed characteristics (Bolognani et al., 2014; Bon-Ho et al., 2003; Gallegos-Lopez et al., 2005; Jung et al., 2015; Lin and Lai, 2012; Nalepa and Orlowska-Kowalska, 2012; Wai and Jahns, 2001). The scheme proposed by Wai and Jahns (Wai and Jahns, 2001) has been implemented in this study because of its simplicity and good performance. The original scheme that consists of an integrator with antiwindup has been adapted to operate in both motoring and generating modes.

This paper is organized as follows. Section 3.2 presents an extended and generalized modeling of the torque ripple produced in PMSMs due to the error from the rotor position sensor. The characteristic trajectories in the different operating regions of the PMSM are derived and described in detail in section 3.3. Section 3.4 shows the simulation results obtained from the torque ripple evaluation along the particular trajectories of a finite-speed

400-W SMPMSM-drive and an infinite-speed 80-kW IPMSM-drive intended for high-speed EV propulsion. The rotor position sensor and the rotor position error compensation algorithm used in this study are described in section 3.5. The experimental results obtained with the 400-W SMPMSM-drive previously simulated are shown in section 3.6. In order to evaluate the torque ripple for the general PMSM model, the simulations of section 3.4 were carried out with an 80-kW IPM machine. However, the experimental validation presented in section 3.7 has been performed with an 80-kW SMPM machine. Finally, the conclusion and some important remarks are given in section 3.8.

3.2 Modeling of the torque ripple produced in PMSMs due to the error from the rotor position sensor

The analysis of the rotor position sensor error effects in the PMSM performance is based on the equivalent dq circuit model shown in Figure 3.1.

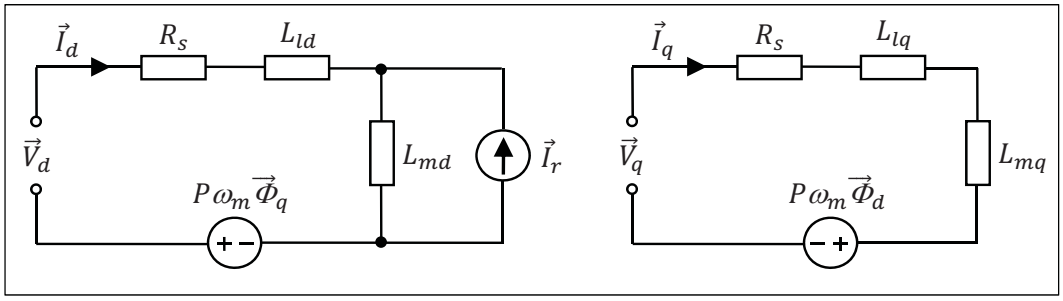

Figure 3.1 Electrical circuit model of the PMSM in the rotating frame

The voltage equations in the rotating frame are expressed as follows

$$\vec{V}_d = R_s\vec{I}_d + \frac{d\,\vec{\Phi}_d}{dt} - P\omega_m\vec{\Phi}_q \tag{3.1}$$

$$\vec{V}_q = R_s\vec{I}_q + \frac{d\,\vec{\Phi}_q}{dt} + P\omega_m\vec{\Phi}_d \tag{3.2}$$

where R_s is the stator winding resistance, $\vec{I}_d$ and $\vec{I}_q$ represent the direct and quadrature dq stator currents, $\vec{\Phi}_d$ and $\vec{\Phi}_q$ stand for the dq magnetic fluxes, ω_m is the mechanical rotor speed, and P is the number of poles pairs of the machine. The magnetic fluxes are in turn a function of the total dq inductances L_d and L_q and the permanent–magnet flux linkage $\vec{\lambda}_r$ as follows

$$\vec{\Phi}_d = L_d \cdot \vec{I}_d + \vec{\lambda}_r \tag{3.3}$$

$$\vec{\Phi}_q = L_q \cdot \vec{I}_q \tag{3.4}$$

The dq leakage inductances L_{ld} and L_{lq} as well as the dq magnetizing inductances L_{md} and L_{mq} are part of the total dq inductances and the rotor flux as follows

$$L_d = L_{ld} + L_{md} \tag{3.5}$$

$$L_q = L_{lq} + L_{mq} \tag{3.6}$$

$$\vec{\lambda}_r = L_{md} \cdot \vec{I}_r \tag{3.7}$$

where $\vec{I}_r$ is a representative constant current source for the rotor magnets. The ideal electromagnetic torque τ_e developed by the PMSM as a function of electrical variables is given by

$$\tau_e = K\left[\vec{\Phi}_d \cdot \vec{I}_q - \vec{\Phi}_q \cdot \vec{I}_d\right] \tag{3.8}$$

and as a function of mechanical variables is defined by

$$\tau_e = J\frac{d\omega_m}{dt} + F\frac{d\theta_m}{dt} + \tau_d + \tau_m \tag{3.9}$$

where K is equal to $3P/2$, J represents the combined moment of inertia of the rotor and the load, F stands for the viscous friction factor, and θ_m is the real mechanical rotor position whereas τ_d and τ_m are the static friction torque and the shaft mechanical torque, respectively.

Note that in the following analysis, the direct and quadrature stator currents in the real and estimated rotor coordinates are denoted with the capital letters $(\vec{I}_d\,, \vec{I}_q)$ and $(\vec{I}_d{}', \vec{I}_q{}')$, respectively, whereas the direct and quadrature stator current references given to the current controllers in the FOC algorithm are denoted with the small letters $(\vec{i}_d\,, \vec{i}_q)$.

The derivation of the equations that model the torque ripple produced in FOC-PMSMs due to the error δ from the rotor position sensor is presented below in three sequential steps by considering 1) the ideal case when $\delta = 0$ and $\vec{I}_d = 0$, 2) the real but particular case when $\delta \neq 0$ and $\vec{I}_d{}' = 0$, and 3) the proposed analysis for the real and general case when $\delta \neq 0$ and $\vec{I}_d{}' \neq 0$.

Assume first the ideal current inverse sequence flowing in a three-phase balanced stator as

$$\vec{I}_a = \vec{I} \cdot sin(\omega_r\, t) \tag{3.10}$$

$$\vec{I}_b = \vec{I} \cdot sin(\omega_r\, t + 120°) \tag{3.11}$$

$$\vec{I}_c = \vec{I} \cdot sin(\omega_r\, t - 120°) \tag{3.12}$$

where $\vec{I}$ is the amplitude of the stator current vector and ω_r represents the real electrical rotor speed. When applying the direct Clarke's transformation to (3.10)–(3.12), the following currents are obtained in the stationary frame $\alpha\beta$

$$\begin{bmatrix} \vec{I}_\alpha \\ \vec{I}_\beta \end{bmatrix} = \begin{bmatrix} \vec{I} \cdot sin(\omega_r\, t) \\ \vec{I} \cdot cos(\omega_r\, t) \end{bmatrix} \tag{3.13}$$

By applying the direct Park's transformation to (3.13) using the real electrical rotor position θ_r and after reducing the resulting expressions considering some trigonometric identities, the direct and quadrature dq stator currents in the real rotating frame become

$$\begin{bmatrix} \vec{I}_d \\ \vec{I}_q \end{bmatrix} = \begin{bmatrix} 0 \\ \vec{I} \end{bmatrix} \tag{3.14}$$

Based on these dq currents, the ideal electromagnetic torque τ_i developed by the PMSM is described as

$$\tau_i = K\left[\vec{\lambda}_r \cdot \vec{I}\right] \tag{3.15}$$

Nevertheless, in reality, the rotor position θ_r' measured by the encoder or the resolver attached to the shaft of the machine deviates from the true position value θ_r due to various nonidealities (Hanselman, 1990; Lara and Chandra, 2014b; Lara et al., 2016b; Lin et al., 2011; Ramakrishnan et al., 2013) such as the misalignment of the sensor components mounted on the PMSM. If considering in the Park's transformation, the position error δ defined as

$$\delta = \theta_r - \theta_r' \tag{3.16}$$

then the measured stator currents no longer lie on the real rotating frame dq but on the estimated one $d'q'$ as it is depicted in Figure 3.2.

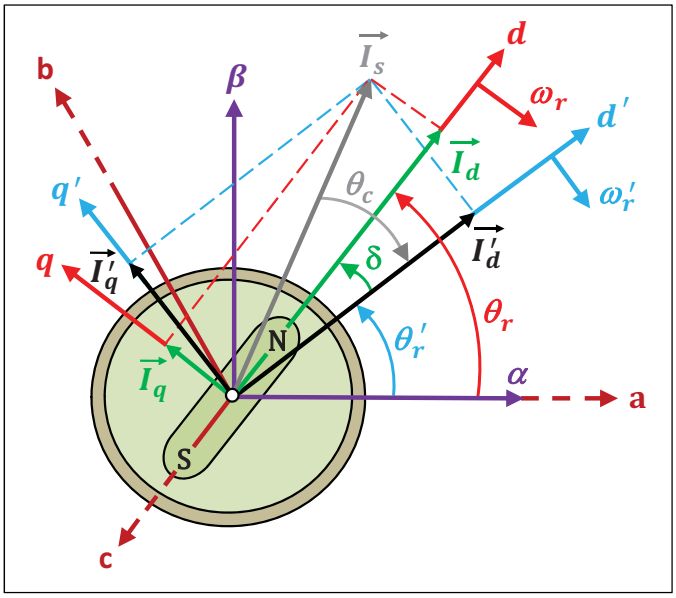

Figure 3.2 Space vector diagram showing the relation between the stationary abc and $\alpha\beta$ coordinates and the real dq and estimated $d'q'$ rotating frames

If the estimated dq currents are now vector controlled to follow the same currents as in (3.14)

$$\begin{bmatrix} \vec{I}_d{}' \\ \vec{I}_q{}' \end{bmatrix} = \begin{bmatrix} 0 \\ \vec{I} \end{bmatrix} \tag{3.17}$$

then the currents flowing through the stator windings of the machine are (Hwang et al., 2011)

$$\begin{bmatrix} \vec{I}_d \\ \vec{I}_q \end{bmatrix} = \begin{bmatrix} \vec{I} \cdot sin(\delta) \\ \vec{I} \cdot cos(\delta) \end{bmatrix} \tag{3.18}$$

By substituting these current components in (3.8), the expression for the real torque τ_r developed by the PMSM is written as (Mok et al., 2007)

$$\tau_r = K\left[\vec{\lambda}_r \cdot \vec{I}\right] + K\left[\vec{\lambda}_r \cdot \vec{I}\right][cos(\delta) - 1] + K(L_d - L_q) \cdot \vec{I}^2 \, sin(\delta)\, cos(\delta) \tag{3.19}$$

The second and third terms in (3.19) model the undesired torque ripple generated by the PMSM due to the measurement error from the rotary position sensor. It can be noted that for the ideal case when $\delta = 0$, (3.19) becomes (3.15).

In the constant torque region of an interior PMSM, the maximum torque per ampere (MTPA) technique sets a negative d-axis current reference $\vec{i}_d$ in the current controller of the FOC algorithm for maximizing the total torque production taking advantage of the reluctance torque exhibited by this type of machine due to its saliency properties. In PMSM-drives for EV applications, the implementation of the flux weakening technique (FWT) in the first FW region (FW1) is essential for extending the base rotor speed as well as for increasing the torque production in the also called constant power region without violating the dc bus voltage constraint. In order to achieve this using FOC, the current reference $\vec{i}_d$ is also set to a negative value that varies nonlinearly with rotor speed. In an infinite-speed PMSM-drive, the maximum torque per volt (MTPV) technique is implemented for operating from the critical speed ω_C up to the theoretical infinite speed with the minimum flux requirement. In this second FW region (FW2), the $\vec{i}_d$ reference always remains negative. The critical speed ω_C (Sul, 2011) theoretically represents the point at which the constant power region ends and the torque starts decreasing in inverse proportion to the square of the rotor speed. As from ω_C , the operating speed is restricted by only voltage constraints (Gallegos-Lopez et al., 2005; Morimoto et al., 1990; Preindl and Bolognani, 2015; Soong and Miller, 1994; Sul, 2011). The equation to calculate ω_C in infinite-speed PMSM-drives is derived in the Appendix II. In the implementation of the techniques of MTPA, FW1, and MTPV/FW2, the vector control condition $\vec{I}_d{}' = 0$ assumed in the previous literature for finding (3.19) is no longer satisfied. Therefore, in this paper, authors propose an extended and generalized modeling of the torque ripple produced in PMSMs due to the error from the rotor position sensor. The proposed model is valid for both SMPM and IPM machines working in any of the aforementioned scenarios.

By considering the vector control general condition $\vec{I}_d{}' \neq 0$ in (3.17), the vector of the real dq currents is expressed as

$$\begin{bmatrix} \vec{I}_d \\ \vec{I}_q \end{bmatrix} = \begin{bmatrix} \cos(\delta) & \sin(\delta) \\ -\sin(\delta) & \cos(\delta) \end{bmatrix} \begin{bmatrix} \vec{I}_d{}' \\ \vec{I}_q{}' \end{bmatrix} \tag{3.20}$$

By substituting (3.20) into (3.8) and after applying some trigonometric identities, the extended and generalized torque modeling equation is written as follows

$$\tau_g = \tau_f + \tau_{\varepsilon_1} + \tau_{\varepsilon_2} \tag{3.21}$$

$$\tau_f = K\left[\vec{\lambda}_r \cdot \vec{I}_q\right] + K\,(\Delta L)\,\vec{I}_d \cdot \vec{I}_q \tag{3.22}$$

$$\tau_{\varepsilon_1} = K\left[\vec{\lambda}_r \cdot \vec{I}_q{}'\right][cos(\delta) - 1] - K\left[\vec{\lambda}_r \cdot \vec{I}_d{}'\right] sin(\delta) \tag{3.23}$$

$$\tau_{\varepsilon_2} = K(\Delta L)\ \vec{I}_d{}' \cdot \vec{I}_q{}'\,[cos(2\delta) - 1] + \frac{K}{2}(\Delta L)\left[\left(\vec{I}_q{}'\right)^2 - \left(\vec{I}_d{}'\right)^2\right] sin(2\delta) \tag{3.24}$$

where τ_f is the ideal torque (3.8) deduced under the assumption that $\delta = 0$; thus, $\vec{I}_q{}' = \vec{I}_q$ and $\vec{I}_d{}' = \vec{I}_d$ are valid only in (3.22), τ_{ε_1} stands for the fundamental torque ripple that is a function of the first-harmonic component of the rotor position error, while τ_{ε_2} represents the reluctance torque ripple that is a function of the second-harmonic component of the rotor position error. The structural anisotropy found in IPMSMs gives rise to the torque ripple component τ_{ε_2} satisfying the condition $\Delta L = (L_d - L_q) \neq 0$.

3.3 Characteristic trajectories in the different operating regions of the PMSM

In the constant torque region, the maximum torque is limited by the phase current constraint defined as

$$\vec{I}_d{}^2 + \vec{I}_q{}^2 \leq \vec{I}_{max}{}^2 \tag{3.25}$$

where $\vec{I}_{max}$ is the maximum current of the PMSM-drive. In this region, the MTPA technique aims to generate a given torque using the minimum magnitude of the stator current vector. The d-axis current that satisfies this condition is found by substituting $\vec{I}_q$ from (3.25) into (3.22), then differentiating τ_f with respect to $\vec{I}_d$ and finally equating to zero. The

resulting second-order equation expressed as a function of the dq currents defines the MTPA trajectory as follows

$$\Delta L \cdot \vec{I}_d^{\,2} + \vec{\lambda}_r \cdot \vec{I}_d - \Delta L \cdot \vec{I}_q^{\,2} = 0 \tag{3.26}$$

given that $L_d < L_q$, the useful solution from this hyperbola equation is the negative $\vec{I}_d$ current so that the reluctance torque contributes to increase the total torque developed by the IPMSM (Morimoto et al., 1994; Sue and Pan, 2008). The intersection of the MTPA trajectory and the current limit circle is deduced by solving (3.26) with the condition (3.25) (Preindl and Bolognani, 2015). The d-axis current for a desired torque τ_f along the MTPA trajectory is obtained by solving the following fourth-order equation that results when substituting $\vec{I}_q$ from (3.26) into (3.22) (Jung et al., 2013)

$$\Delta L^3 \cdot \vec{I}_d^{\,4} + \left(3\,\vec{\lambda}_r \Delta L^2\right) \cdot \vec{I}_d^{\,3} + \left(3\,\vec{\lambda}_r^{\,2} \Delta L\right) \cdot \vec{I}_d^{\,2} + \vec{\lambda}_r^{\,3} \cdot \vec{I}_d - \Delta L \left(K' \tau_f\right)^2 = 0 \tag{3.27}$$

with $K^{'} = 1/K$. In the first FW region, the maximum torque is obtained when operating along the current limit circle satisfying simultaneously the current condition (3.25) and the following phase voltage constraint (Morimoto et al., 1990)

$$\vec{V}_d^{\,2} + V_q^{\,2} \leq \vec{V}_{max}^{\,2} \tag{3.28}$$

where in case of using space vector modulation (SVM), the linear range for a given dc bus voltage V_{dc} limits the maximum voltage $\vec{V}_{max}$ to $V_{dc}/\sqrt{3}$. Assuming a negligible voltage drop due to the stator resistance terms in (3.1) and (3.2) and considering steady-state conditions, (3.28) is rewritten as follows

$$\left(L_d \cdot \vec{I}_d + \vec{\lambda}_r\right)^2 + L_q^{\,2} \cdot \vec{I}_q^{\,2} \leq \left(\frac{\vec{V}_{max}}{\omega_r}\right)^2 = \left(\vec{\phi}_r\right)^2 \tag{3.29}$$

Note that the diameter of this voltage limit ellipse decreases with the increasing of the rotor speed ω_r . The d-axis current for a desired torque τ_f at a given speed in the first FW region

is found by solving the following fourth-order equation that results when substituting $\vec{I}_q$ from (3.22) into (3.29) (Hoang et al., 2013)

$$(L_d \Delta L)^2 \cdot \vec{I}_d^{\,4} + \left(2\,\vec{\lambda}_r L_d \Delta L\right)(L_d + \Delta L) \cdot \vec{I}_d^{\,3} + \left[\left(L_d \cdot \vec{\lambda}_r^{\,2}\right)(L_d + 4\Delta L) - \vec{U} \cdot \Delta L^2\right] \cdot \vec{I}_d^{\,2} + \left(2\vec{\lambda}_r\right)\left(L_d \cdot \vec{\lambda}_r^{\,2} - \vec{U} \cdot \Delta L\right) \cdot \vec{I}_d + L_q^{\,2}\left(K' \tau_f\right)^2 - \vec{U} \cdot \vec{\lambda}_r^{\,2} = 0 \tag{3.30}$$

where $\vec{U} = \vec{\phi}_r^{\,2} - \vec{\lambda}_r^{\,2}$. In the first FW region, the d-axis current for a given rotor speed ω_r at the maximum torque is obtained by solving (3.29) with the condition (3.25). In infinite-speed PMSM-drives (Soong and Miller, 1994), the second FW region is limited only by the voltage constraint (3.28). Hence, the MTPV technique aims to generate a given torque using the minimum magnitude of the stator voltage vector. The MTPV trajectory is derived by substituting $\vec{I}_q$ from (3.22) into (3.29), then differentiating the flux $\vec{\phi}^2$ with respect to $\vec{I}_d$ and equating to zero (Bon-Ho et al., 2003). The resulting second-order equation expressed as a function of the dq currents is given by

$$\left(L_d^{\,2} \cdot \Delta L\right) \cdot \vec{I}_d^{\,2} + \left(\vec{\lambda}_r \cdot L_d\right)(L_d + \Delta L) \cdot \vec{I}_d + L_d \vec{\lambda}_r^{\,2} - \left(L_q^{\,2} \cdot \Delta L\right) \cdot \vec{I}_q^{\,2} = 0 \tag{3.31}$$

One of the zero crossings of this hyperbola occurs at the point of infinite speed $\vec{I}_d = -(\vec{\lambda}_r / L_d)$. The intersection of the MTPV trajectory and the current limit circle is deduced by solving (3.31) with the condition (3.25) whereas the d-axis current for a desired torque τ_f along the MTPV trajectory is obtained by solving the following fourth-order equation that results when substituting $\vec{I}_q$ from (3.22) into (3.31)

$$\left(L_d^{\,2} \cdot \Delta L^3\right) \cdot \vec{I}_d^{\,4} + \left(\vec{\lambda}_r L_d \Delta L^2\right)\left(4L_d - L_q\right) \cdot \vec{I}_d^{\,3} + 3\vec{\lambda}_r^{\,2} L_d \Delta L (L_d + \Delta L) \cdot \vec{I}_d^{\,2} + \left(\vec{\lambda}_r^{\,3} L_d\right)(L_d + 3\Delta L) \cdot \vec{I}_d + L_d \cdot \vec{\lambda}_r^{\,4} - \left(L_q^{\,2} \Delta L\right)\left(K' \tau_f\right)^2 = 0 \tag{3.32}$$

The d-axis current along the MTPV trajectory for a given rotor speed ω_r is found by solving the following second-order equation that results when substituting $\vec{I}_q$ from (3.31) into (3.29)

$$2\left(L_d{}^2 \cdot \Delta L\right)\cdot \vec{I}_d{}^2 + \vec{\lambda}_r L_d (L_d + 3\Delta L)\cdot \vec{I}_d + \vec{\lambda}_r{}^2 (L_d + \Delta L) - \Delta L \left(\frac{\vec{V}_{max}}{\omega_r}\right)^2 = 0 \qquad (3.33)$$

The equations for the SMPMSM are derived by substituting $L_d = L_q = L$ and $\Delta L = 0$ into (3.26), (3.27) and (3.29)–(3.33).

3.4 Torque ripple evaluation along the characteristic trajectories of the PMSM

A simulated 80-kW IPMSM intended for EV propulsion and the 400-W SMPMSM used in experiments have been considered to carry out the torque ripple evaluation. The parameters of these machines are given in Table I of the Appendix II. The characteristic trajectories along the different operating regions for both PMSMs are shown in Figure 3.3. In order to simplify the visualization of all the trajectories, the number of displayed curves has been limited by considering a static operating point of the motor parameters.

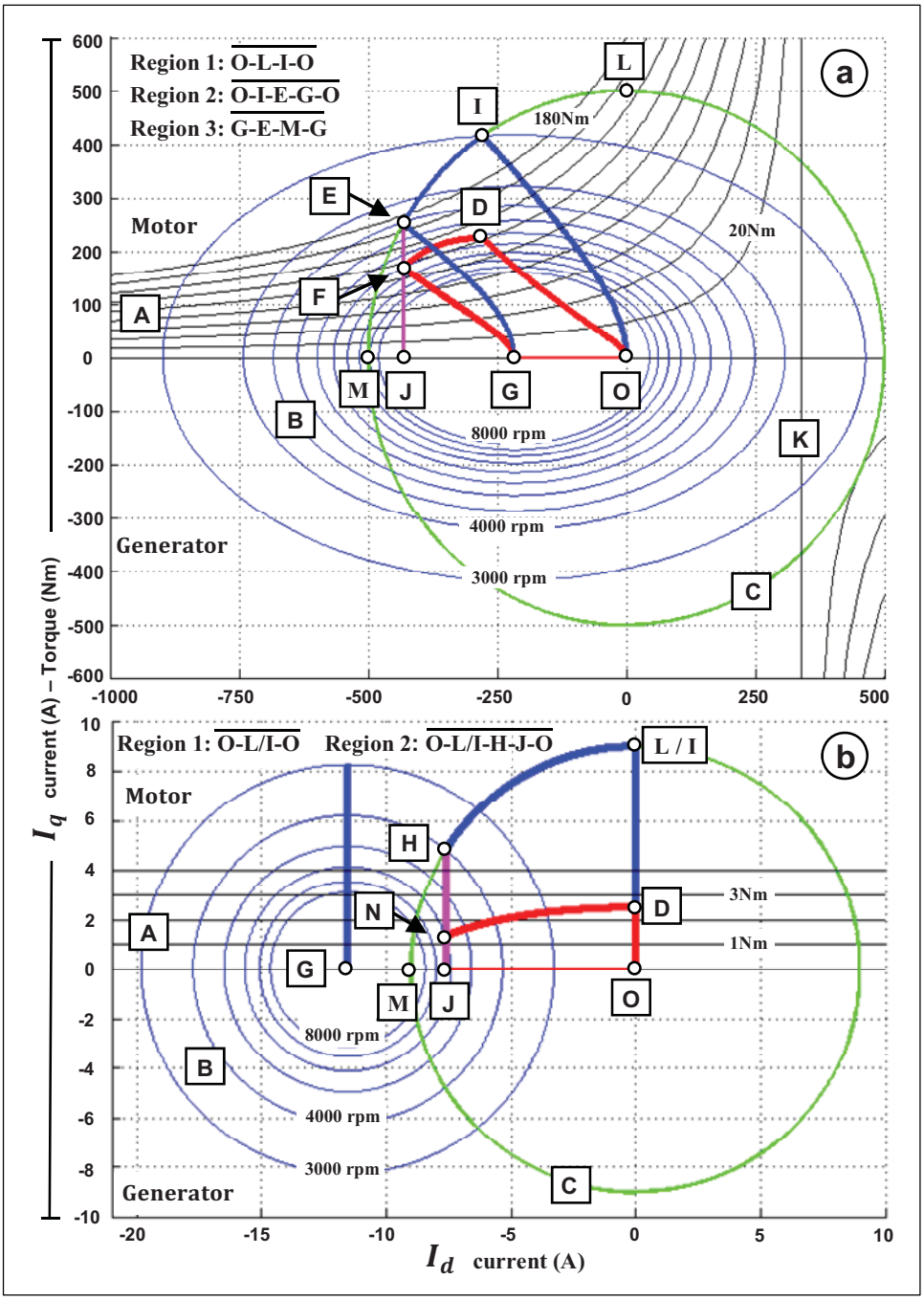

Figure 3.3 Characteristic trajectories and operating regions of: a) 80-kW IPMSM intended for EV applications b) 400-W SMPMSM used in the experimental tests

For the 80-kW IPMSM, the constant torque hyperbolas, the voltage limit ellipses, and the current limit circle are denoted in Figure 3.3 a) with the letters A, B, and C. Note that the point of infinite speed $\vec{I}_d = -(\vec{\lambda}_r/L_d)$, the maximum demagnetizing current and the torque

hyperbola asymptote are also marked with the letters G, J, and K. The maximum torque of 225 N·m is pointed out with the letter D. Likewise, the letters I and E indicate the base speed ω_B and the critical speed ω_C of about 3000 and 4500 r/min, respectively. In this EV IPMSM-drive, the dc bus voltage is limited to 350 V. If considering the y-axis units in [A], then the MTPA, the FW1, and the MTPV/FW2 trajectories are defined by the segments $\overline{\mathrm{OI}}$, $\overline{\mathrm{IE}}$, and $\overline{\mathrm{EG}}$. If considering the y-axis units in [N·m], then these trajectories are equivalent to the segments $\overline{\mathrm{OD}}$, $\overline{\mathrm{DF}}$ and $\overline{\mathrm{FG}}$. The area enclosed by these segments corresponds to the optimal operating region of the IPM machine.

For the 400-W SMPMSM used in experiments, the saliency ratio $\eta = L_q/L_d$ is equal to unity. Accordingly, the characteristic voltage limit ellipses turn out into circles whereas the constant torque hyperbolas become straight lines as it is observed in Figure 3.3 b). The dc bus voltage and the maximum stator current magnitude have been limited to 72 V and 1.8 times the rated current, respectively. Considering these constraints as well as the torque requirement in the constant power region of 1.2 N·m, the maximum speed for the SMPMSM-drive used in the experimental tests is restricted to 4000 r/min. The maximum demagnetizing current applied to the machine is about −8 A. The operating point at these maximum conditions of current, torque, and speed is pointed out in Figure 3.3 b) with the letters H [A] and N [N·m]. Note that unlike the 80-kW IPMSM-drive, in the 400-W SMPMSM drive the point of infinite speed G located at $\vec{I}_d = -11.5$ A lies out of the current limit circle radius of 9 A.

Bearing in mind the machine-drive characteristics of the 80-kW IPMSM and the 400-W SMPMSM, the torque ripple components generated along their particular trajectories have been evaluated as a function of the rotor position error δ by solving simultaneously the equations deduced in section 3.2 and section 3.3. Figure 3.4 shows the torque ripple obtained when substituting the stator currents from (3.25), (3.26) and (3.31) into (3.23) and (3.24), while considering a sinusoidal position error δ with a peak value ρ equal to 1 electrical degree. It can be observed that the torque ripple produced by the 80-kW IPMSM is insignificant below the base speed $\omega_B \approx$ 3000 r/min [$\overline{\mathrm{OD}}$]. From thereon, the torque

oscillations gradually increase along the first FW trajectory [$\overline{DF}$] reaching 4N·m at the critical speed $\omega_C \approx 4500$ r/min and finally they progressively decrease throughout the second FW trajectory [$\overline{FG}$] until dropping near 50% at the point of infinite speed. For the 400-W SMPMSM, the torque ripple is also negligible in the constant torque region [$\overline{OD}$] even under the maximum motoring torque of 2.5 N·m. Then, the torque oscillations gradually increase with rotor speed in the constant power region along the first FW trajectory [$\overline{DN}$] reaching an amplitude of around 0.037 N·m at 4000 r/min.

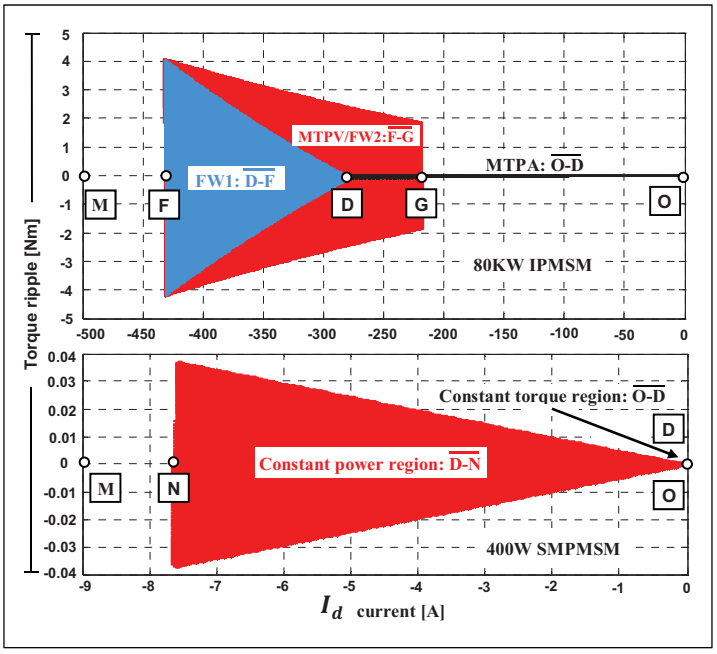

Figure 3.4 Torque ripple generated along the characteristic trajectories of the 80-kW IPMSM (top) and the 400-W SMPMSM (bottom) for a sinusoidal position error that varies between ±1°

If the torque ripple τ_{ripple} is expressed in percentage as the ratio of the torque oscillations magnitude to the mean value $\overline{\mu}$ of the maximum torque τ_{max} as follows

$$\tau_R = \left| \frac{max(\tau_{ripple}) - min(\tau_{ripple})}{\overline{\mu}[\tau_{max}]} \right| \text{x}100\% \tag{3.34}$$

then the pair of PM machines afore analyzed considering $\rho = 1°$ produce a torque ripple of around 3.6% and 3%, respectively. Figure 3.5 shows the torque ripple τ_R obtained when varying the rotor position error peak value ρ from zero up to 5° in steps of half a degree. It can be deduced that in order to achieve a high-performance PMSM-drive with a torque ripple smaller than 5%, the allowable error range for the position sensor attached to the shaft of the 80-kW IPMSM and the 400-W SMPMSM are ±1.4° and ±1.7°, respectively.

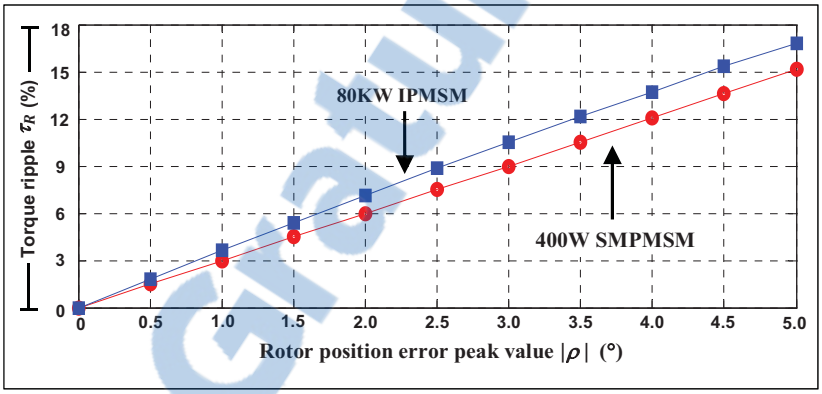

Figure 3.5 Torque ripple produced by the analyzed PMSMs as a function of the peak value of the periodical error from the rotor position sensor

By following the experimental scheme depicted in Figure 3.11, the FOC of both PM machines has been simulated in MATLAB-SimPowerSystems for the ideal case when $\rho = 0°$ as well as for the two real cases when $\rho = 2°$ and $\rho = 4°$. The oscillations contained in the corresponding periodical position error δ have been modeled using the Fourier series (3.35) of the rotor position errors obtained experimentally. In the simulation, the PMSMs under test are controlled in torque mode, while setting the torque reference τ_e^* to the maximum values of 225 and 2.5 N·m, respectively. The coupled machine running in speed mode generates a ramp speed change at a rate of 1000 r/min/s^2 going from standstill up to the maximum speed of each machine. Bearing in mind the practical conditions in a real EV, the theoretical infinite speed of the 80-kW IPMSM-drive has been restricted to 12 000 r/min. In case of the finite-speed 400-W SMPMSM-drive, the design characteristics have limited its maximum operating speed to 4000 r/min. Figure 3.6 and Figure 3.7 show the resulting dq current components and the motoring torque produced in the whole operating speed range of the

machines. It can be observed how the torque ripple increases with rotor speed along the constant power region and how the torque oscillations produced by the IPMSM start decreasing beyond the critical speed agreeing with the results previously presented in Figure 3.4. The maximum torque ripple τ_R produced by the two PMSMs simulated for the three different position errors has a quite good matching with the percentages of Figure 3.5 formerly calculated with (3.21)–(3.24).

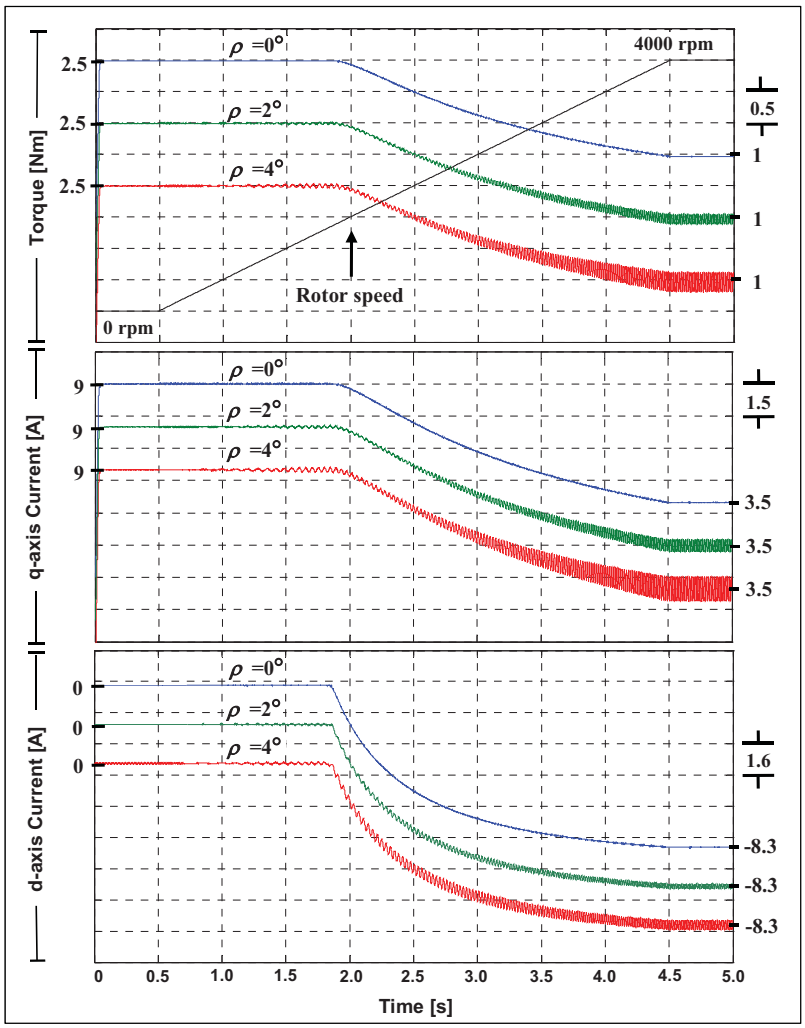

Figure 3.6 Simulation results obtained with the 400-W SMPMSM. Torque and dq currents for three different rotor position error peak values ρ

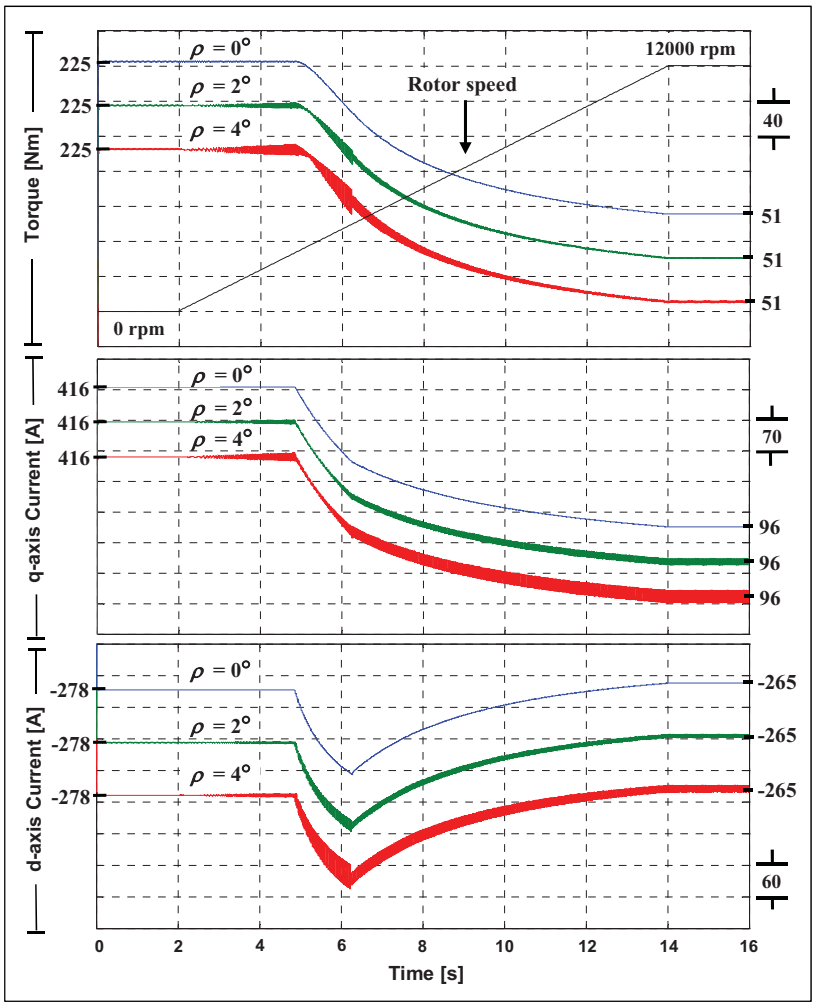

Figure 3.7 Simulation results obtained with the 80-kW IPMSM. Torque and dq currents for three different rotor position error peak values ρ

3.5 Rotor position sensor and rotor position error compensation algorithm

3.5.1 Rotor position sensor

The rotor position sensor mounted on the 400-W SMPMSM and the 80-kW SMPMSM used in experiments is a magnetic quadrature encoder based on an application-specific-integrated circuit (ASIC). The Hall-effect elements contained inside the ASIC translate the angular position of a two-pole magnet into a pair of sine–cosine analog voltage signals. The magnet rotates radially over the IC surface as it is shown in Figure 3.8.

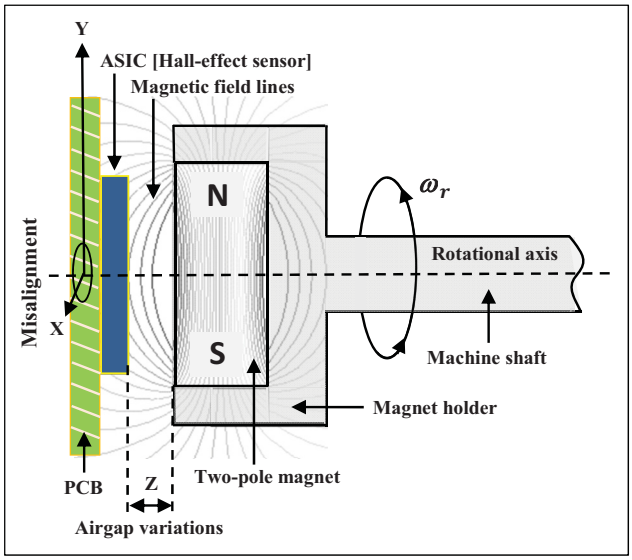

Figure 3.8 Sketch of the on-axis rotor position measurement. The ASIC, the magnet, and the machine shaft are all aligned with the rotational axis

The imperfect mechanical mounting of the encoder parts on the machine, the nonhomogeneity of the magnetic field lines from the magnet and the unequal electronic amplification of the encoder voltage outputs due to the tolerance of the components used in each circuitry path are only some of the causes that bias the encoder signals from the ideal sine-cosine waveforms. These unwanted phenomena give rise to the encoder nonidealities of amplitude mismatch, nonzero dc offset, nonorthogonality, and harmonic distortion (Lara et al., 2016b). The effect from these nonidealities is a periodical rotor position error δ that repeats every mechanical revolution (Hanselman, 1990; Lara and Chandra, 2014b; Lara et al., 2016b; Lin et al., 2011; Ramakrishnan et al., 2013). This position error is modeled by a Fourier series as follows

$$\delta = A_0 + \sum_{n=1}^{M} A_n \cdot [sin(n \cdot \theta_r + \vartheta_n)] \tag{3.35}$$

The dc component A_0 originated by the misalignment between the rotor magnetic flux axis "+d" and the position sensor 0° measurement can be accurately corrected using the two methods proposed in (Rahman and Hiti, 2005). Nevertheless, the remaining periodical error must be properly reduced with some kind of compensation algorithm in order to achieve a

high-performance FOC-PMSM drive given that the oscillations contained in the rotor position error δ give rise to the unwanted torque ripple produced by the machine.

3.5.2 Rotor position error compensation algorithm

The algorithm implemented in this study for compensating the periodical rotor position error from the magnetic analog encoder is a technique based on polynomial approximations (PA). The details of the PA compensation algorithm are presented in (Lara et al., 2016b).

The experimental results obtained from the encoder mounted on the 400-W and 80-kW SMPMSMs working at different conditions of torque and speed are shown in Figure 3.9. Note that the encoder signals before (B) the compensation plus the PA are equal to the encoder signals after (A) the compensation.

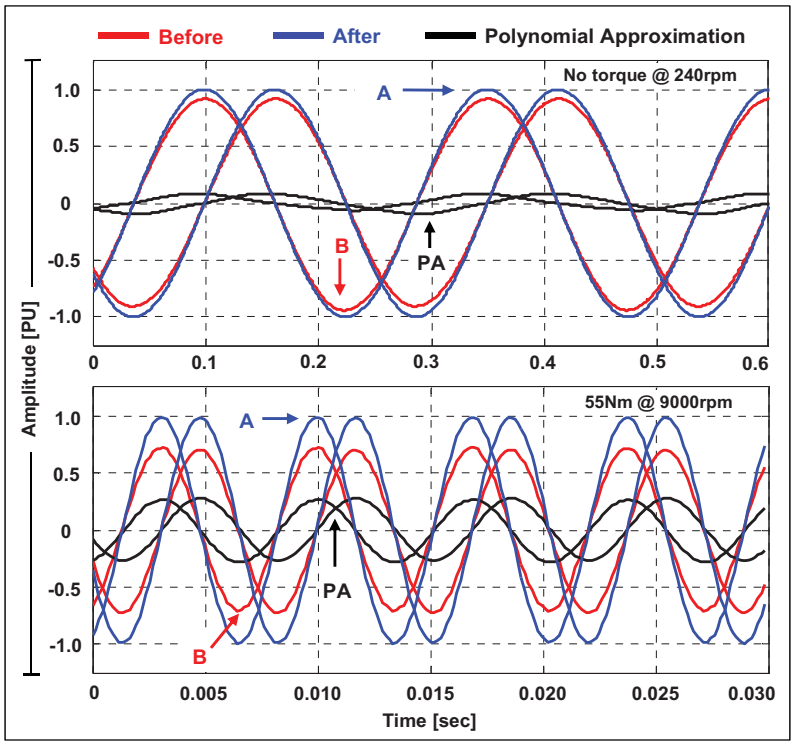

Figure 3.9 Experimental results: Sine–cosine encoder signals before and after the PA compensation for the analog magnetic encoder mounted on (top) 400-W SMPMSM (bottom) 80-kW SMPMSM

The equivalent Lissajous figures are shown in Figure 3.10. It is noteworthy that thanks to the PA algorithm, the nonidealities contained in the encoder signals have been fairly compensated.

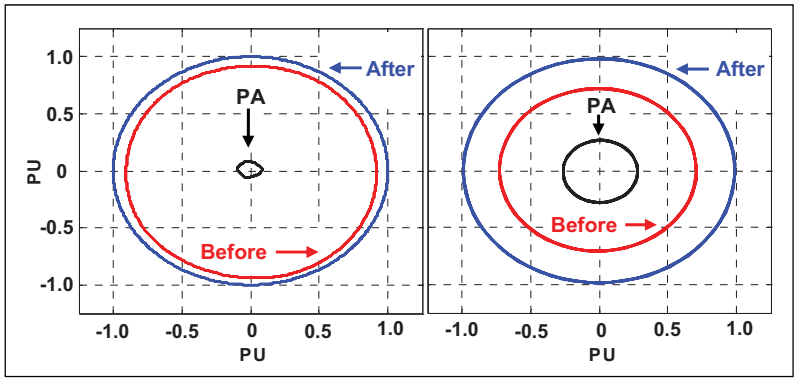

Figure 3.10 Experimental results: Lissajous figure before and after the PA compensation for the analog magnetic encoder mounted on (left) 400-W SMPMSM (right) 80-kW SMPMSM

3.6 Experimental results

The overview of the scheme followed to evaluate the torque ripple produced by the PMSMs due to the error from the rotor position sensor is depicted in Figure 3.11, while a photograph of the test bench built is shown in Figure 3.12. The machine under test, a three-phase wye-connected 400-W SMPMSM has been tightly coupled to another SMPMSM controlled by a high-performance industrial drive. Two reconfigurable banks of rechargeable lead-acid batteries Enerwatt WP12-12 are used to feed the dc bus of the two-level inverter based drives.

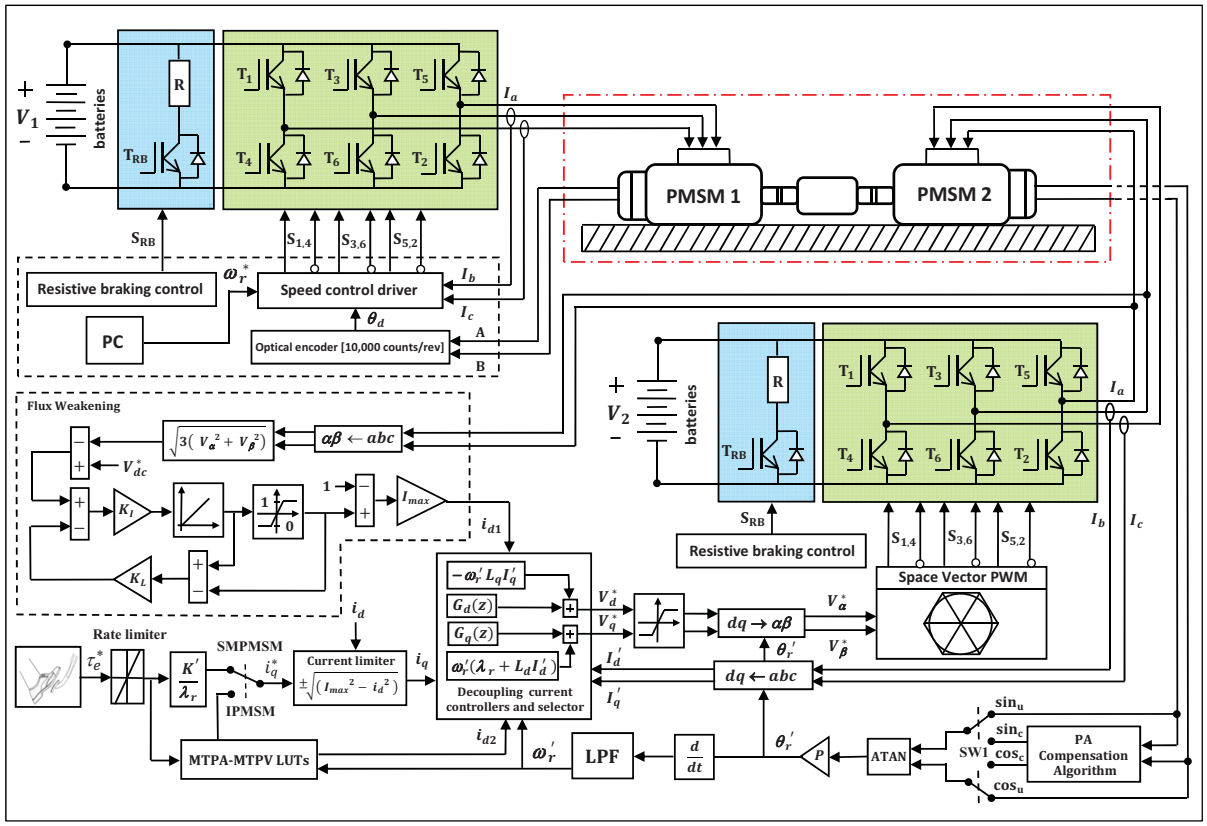

Figure 3.11 General overview of the scheme followed to carry out the evaluation of the torque ripple produced by the 400-W SMPMSM and the 80-kW IPMSM due to the error from the rotor position sensor

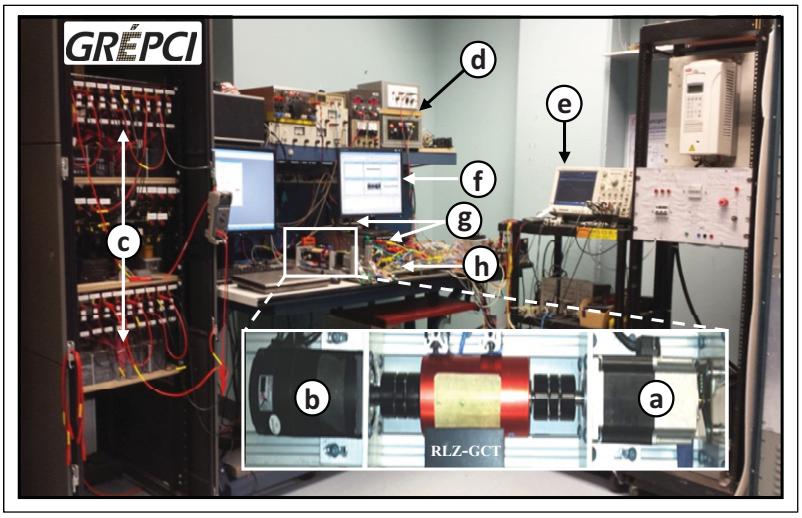

Figure 3.12 Experimental setup used for the tests: a) 400-W SMPMSM under study b) Industrial SMPMSM c) Rechargeable battery banks d) DC voltage sources e) Scope f) Control panel developed in code composer studio (CCS) g) Two-level inverters h) TI DSP-based control board

In order to control the stator currents at each 12° when the machine is operating at the maximum speed of 4000 r/min, the inverter switching frequency f_{sw} has been set to 8 kHz. The time step to execute the FOC algorithm fully implemented in the TI DSP TMS320F28335 is 125 µs.

In the experiments, the industrial SMPMSM-drive is programmed to follow the trapezoidal speed profile shown in Figure 3.13 a), while the 400-W SMPMSM under study is controlled in torque mode to develop the maximum motoring and regenerative braking symmetrical torque of 0.9N·m at the maximum speed of ±4000 r/min. The effects of the rotor position sensor error have been evaluated for the four-quadrant operation of the machine according to the compensation status waveform shown in Figure 3.13 f). The on and off states correspond to the compensated and uncompensated rotor position cases with $\rho = 2°$ and $\rho = 4°$, respectively. The resulting torque as well as the direct and quadrature stator currents obtained from the FOC of the 400-W SMPMSM are shown in graphics b, c and d, e of Figure 3.13. It is noteworthy the fairly good matching between the simulation and the experimental results.

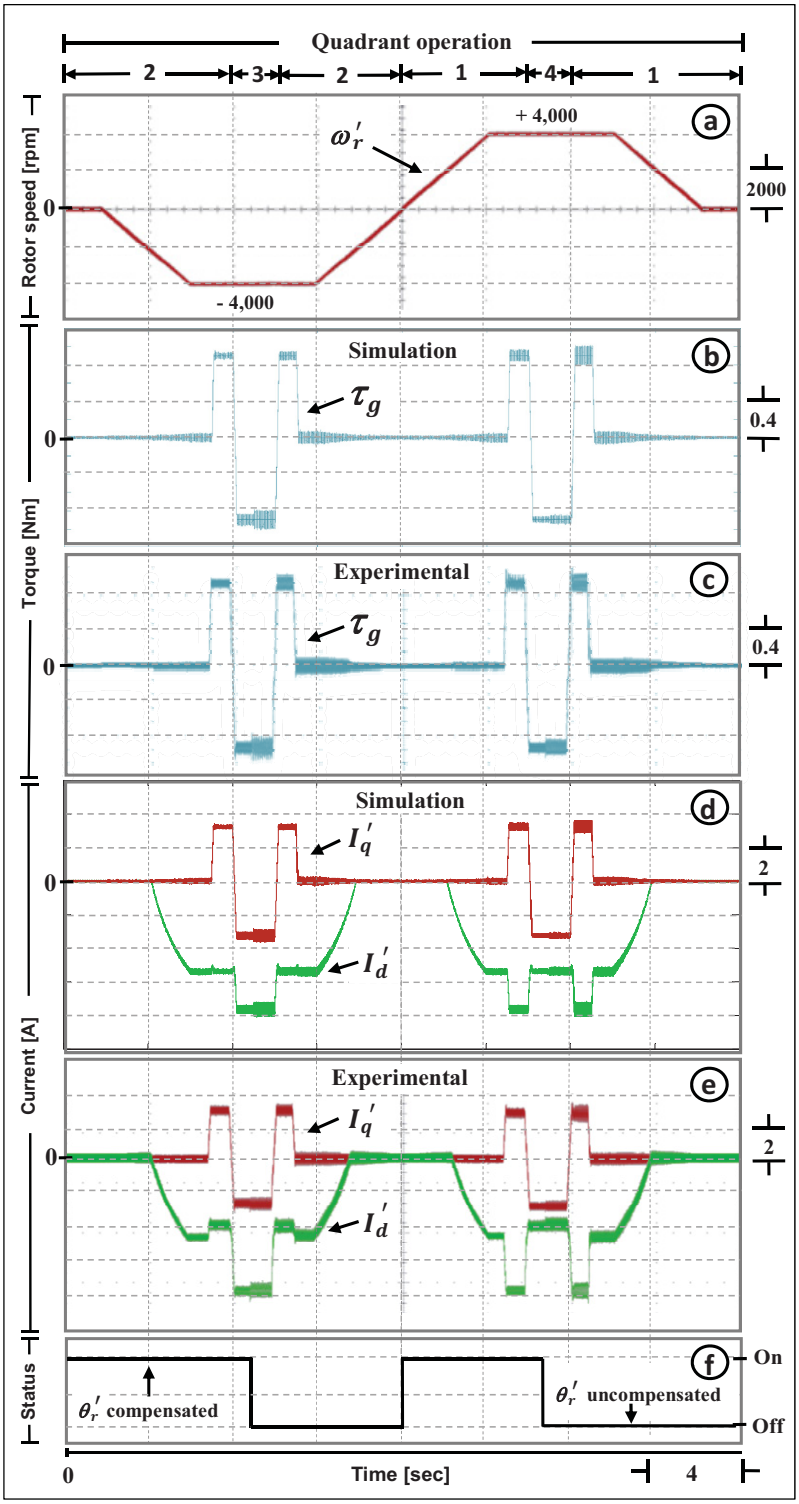

Figure 3.13 Simulation and experimental results obtained with the 400-W SMPMSM. Effects of the rotor position sensor error in the torque and the $d'q'$ currents for the four-quadrant operation of the machine

In the following test, the rotor speed is kept constant at −3000 r/min and the torque reference τ_e^* is step-changed from ±1.2 to ∓1.2 N·m while alternating from the uncompensated to the compensated rotor position. The stator voltage and current waveforms of phase a as well as the ripple of voltage, current, and torque produced under these conditions are shown in Figure 3.14. It can be noted that the torque ripple is smaller in the generating mode than in the motoring mode given that less defluxing current on the d'-axis is required for satisfying the dc bus voltage constraint. Regarding the torque ripple magnitude when the transition of the rotor position occurs at t = 5 s, it decreases from ±0.1 to ±0.05 N·m. These experimental results agree well with the curves of Figure 3.6 previously obtained through simulations.

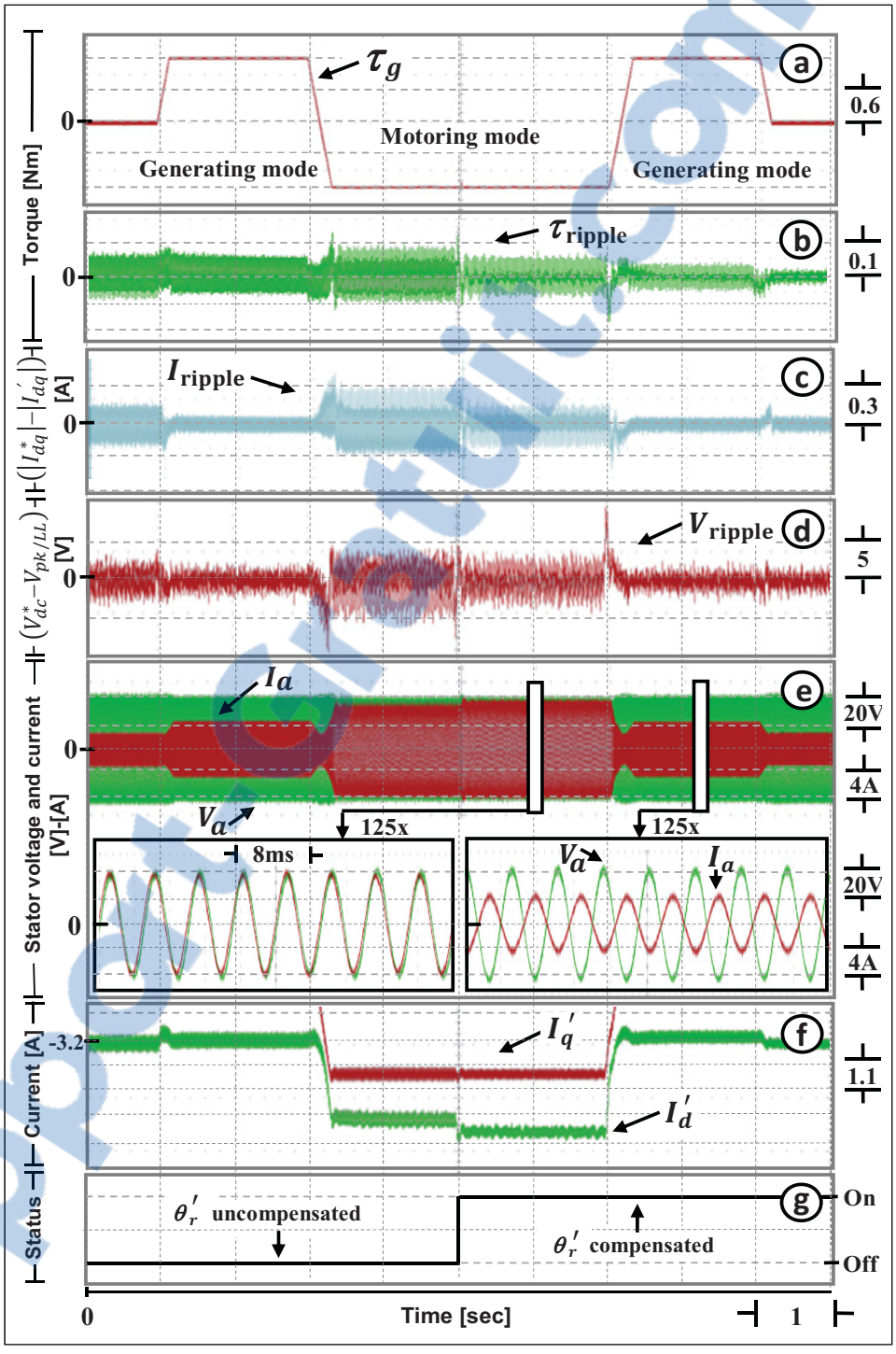

Figure 3.14 Experimental results obtained with the 400-W SMPMSM. Torque, current, and voltage ripples produced during the motoring and generating torque step-changes at −3000 r/min, while changing from the uncompensated to the compensated rotor position

3.6.1 Frequency-domain analysis of the torque ripple and the rotor position error

The time- and frequency-domain analysis of the rotor position error before and after the PA compensation as well as of the torque ripple produced by the 400-W SMPMSM due to these position errors is described below.

The frequency analysis has been performed at −3000 r/min (50Hz) under maximum symmetrical torque conditions for both motoring and generating operation modes. The obtained simulation and experimental results are shown in Figure 3.15.

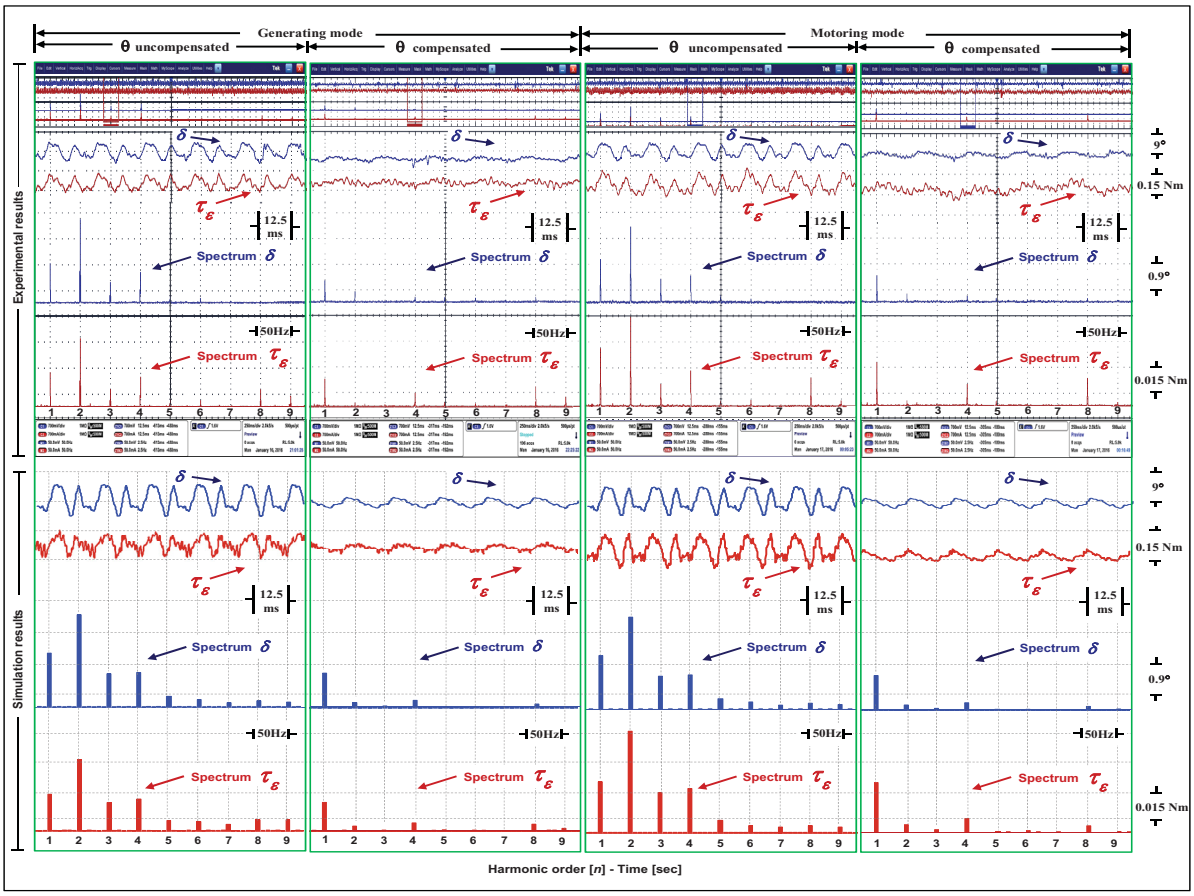

Figure 3.15 Experimental and simulation results: Time- and frequency-domain analysis of the rotor position error δ and the torque ripple τ_ε produced by the 400-W SMPMSM

In Y-connected three-phase PMSMs, the imperfect sinusoidal air-gap flux density produces multiples of sixth-order harmonics in the torque equation expressed in the rotating frame (Gebregergis et al., 2015; Rojas et al., 2010; Shin et al., 2012; Weizhe et al., 2004). Likewise, given that there are six zero crossings per electrical cycle in a three-phase machine, the dead-time effect also produces a sixth-order torque ripple harmonic component (Shaotang et al., 2002). Considering the four poles pairs of the 400-W SMPMSM, the multiples of sixth-order electrical harmonics would appear as multiples of twenty-fourth-order harmonics in the frequency analysis of Figure 3.15 since the fundamental component is evaluated over a mechanical revolution. However, the harmonics beyond the ninth-order are not shown in the figure because their magnitude was not significant for the analysis. The negligible magnitude of the twenty-fourth harmonic component and its multiples means: 1) the assumption of a sinusoidal flux distribution producing a sinusoidal back-electromotive force (BEMF) is a valid approximation in the proposed model, and 2) the dead-time effect has an insignificant contribution to the torque ripple generation.

The torque ripple harmonics produced due to the cogging effect appear at frequencies that are multiple of $N_{ps} \cdot f_r$ (Rojas et al., 2010; Shin et al., 2012; Sun et al., 2011; Weizhe et al., 2004), where f_r is the mechanical rotor frequency and N_{ps} is the least common multiple (LCM) between the number of poles and slots. Considering the 8 poles and 12 slots of the 400-W SMPMSM, the cogging torque harmonics are thus multiple of 24. These high-order harmonics are fairly reduced by the inertia of the shaft with the increasing of the machine speed. Hence, the interaction between the rotor permanent–magnet field and the stator slots is also negligible in this study.

It is noteworthy the quite good matching between the simulation and the experimental results and how the first harmonics of the torque ripple are significantly reduced when the position error is compensated. This fairly high correlation demonstrates that the effect of the rotor position error in the torque ripple is much more significant than other uncertainties such as the current sensor inaccuracy, the finite word-length (FWL) effect, the finite PWM resolution, the PWM switching, the inverter dead-time, the asymmetric stator phase

resistance, the cogging effect, and the nonsinusoidal air-gap flux density (Gebregergis et al., 2015; Shaotang et al., 2002; Weizhe et al., 2004; Xu et al., 2014).

3.7 Experimental validation with an 80-kW SMPMSM

The torque ripple modeling has been also validated with an EV-drive controlling an 80-kW SMPMSM designed and manufactured by the company TM4. Figure 3.16 shows the complete experimental setup built at TM4 facilities.

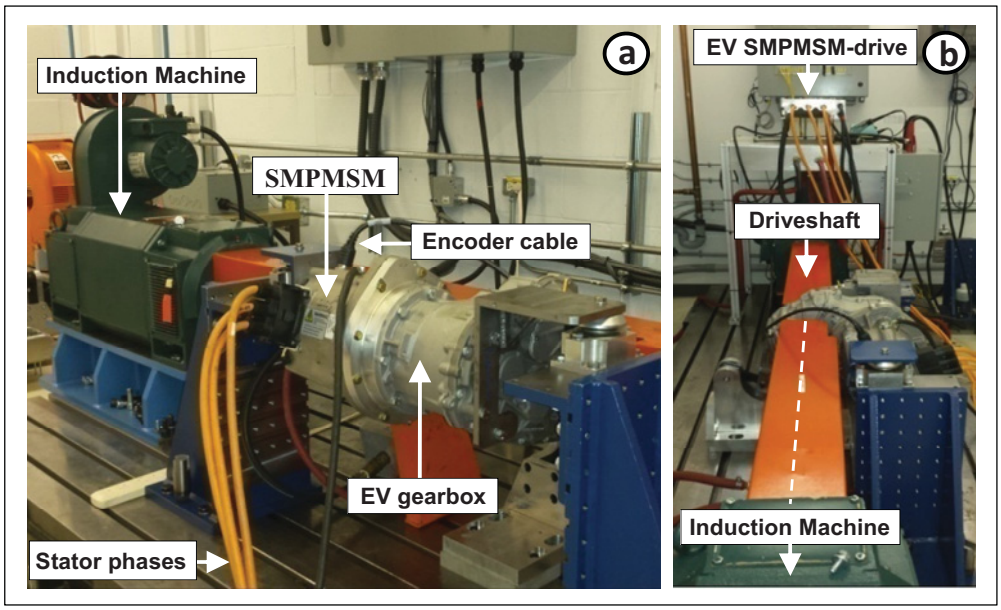

Figure 3.16 Experimental setup built at TM4. The rotor position sensor is mounted on the back-side of the 80-kW SMPMSM that in turn is coupled to the driveshaft of an induction machine by means of an EV gearbox with a ratio of 10:1 a) Front view b) Lateral view

The mechanical torque ripple obtained for both motoring and regenerative braking operation modes under the maximum torque conditions going from 100 N·m at 1000 r/min up to 55 N·m at 9000 r/min is shown in Figure 3.17. It is noteworthy that thanks to the compensation of the error from the magnetic analog encoder mounted on the 80-kW SMPMSM, the torque ripple magnitude has been reduced in all the cases to the range of ±1 N·m.

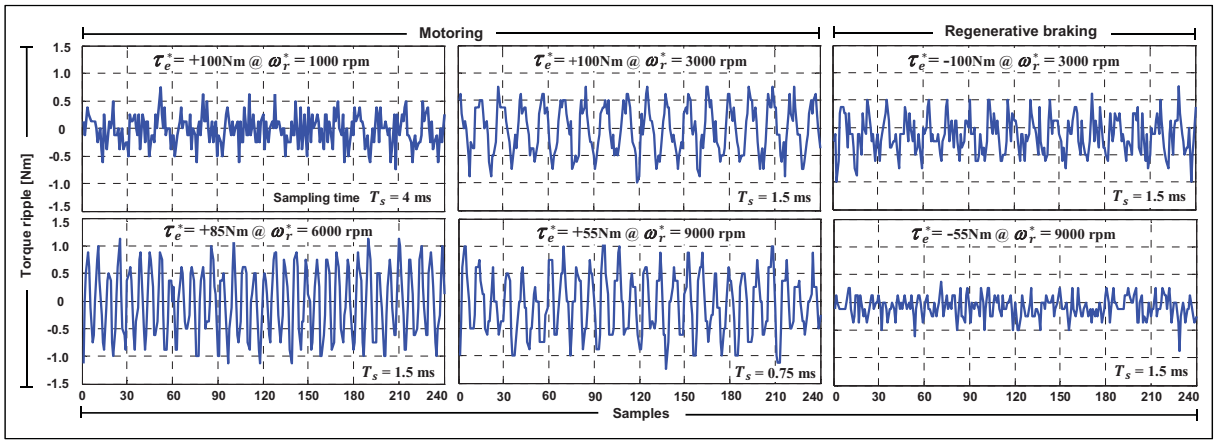

Figure 3.17 Experimental results: Mechanical torque ripple produced by the 80-kW SMPMSM at different speeds for both motoring and generating operation modes

Figure 3.18 shows the time- and frequency-domain analysis of the rotor position error and the torque ripple generated by the 80-kW SMPMSM during the online transition from the uncompensated to the compensated rotor position. This analysis has been performed at 9000 r/min under 55 N·m of motoring torque. It can be observed how the compensation of the rotor position error allows decreasing instantaneously the torque oscillations from 5 N·m to less than 2 N·m. It is noteworthy also how the first-order harmonic of the torque ripple decreases when the first-order harmonic of the rotor position error is reduced through the activation of the PA compensation algorithm. As in the case of the frequency analysis results obtained with the 400-W SMPMSM, this fairly high correlation also demonstrates that the rotor position error has a quite bigger influence on the torque ripple generation than other type of uncertainties [14]–[17].

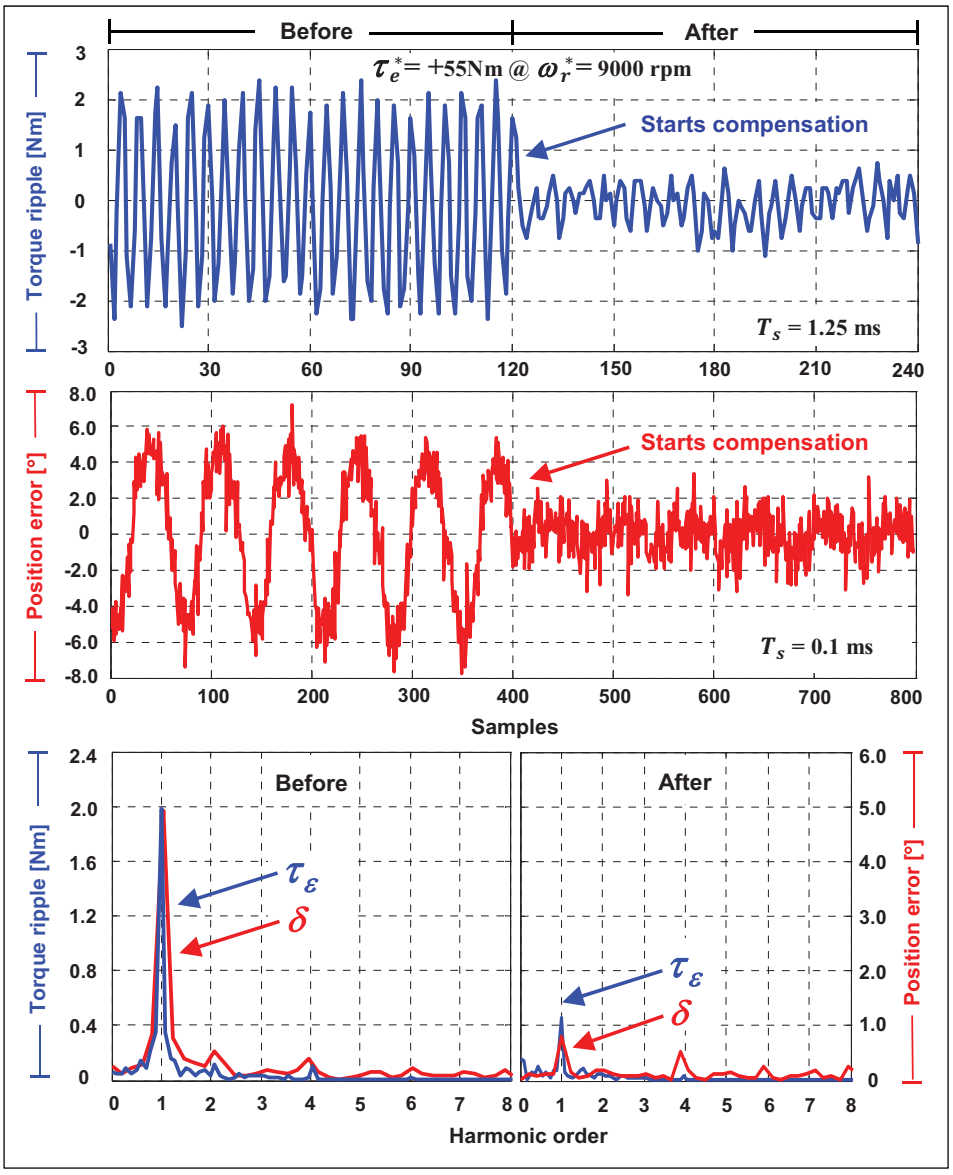

Figure 3.18 Experimental results: Time- and frequency-domain analysis of the rotor position error δ and the torque ripple τ_ε produced by the 80-kW SMPMSM before and after the activation of the PA compensation algorithm

The maximum dynamic rotor eccentricity and the maximum radial misalignment undergone by the rotor position sensor parts are given by the maximum radial clearance of the rotor bearings. In order to evaluate the impact of this clearance on the encoder misalignment and its accuracy, the rotor position error has been measured at different speeds going from 300 up to 9000 r/min.

In Figure 3.19, it can be observed that the waveform of the compensated rotor position error is fairly uniform and how it remains below 1 electrical degree for the whole speed range of the tests in spite of the different dynamic conditions undergone by all of the involved mechanical elements. Hence, the encoder misalignment and the equivalent rotor position error are marginally influenced by the rotor eccentricity and the inherent mechanical vibrations.

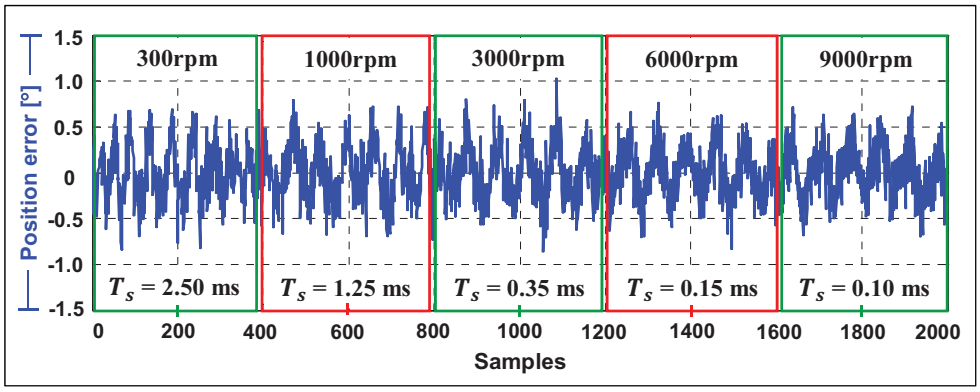

Figure 3.19 Experimental results: Compensated rotor position error at different speeds ω_r^* under no commutation of the inverter for evaluating the influence of the rotor eccentricity and the mechanical vibrations on the encoder accuracy

3.8 Conclusion

The effects of the rotor position error in the performance of FOC PMSM-drives intended for EV traction applications have been analyzed in this paper.

The extended and generalized model developed for evaluating the torque ripple produced in PMSMs due to the error from the rotor position sensor has been verified in simulation for a finite-speed SMPMSM-drive and an infinite-speed IPMSM-drive. The experimental results obtained with the 400-W SMPMSM and the 80-kW demonstrate the accuracy of the proposed model.

The compensation of the error from the rotary position sensor mounted on the 80-kW SMPMSM from TM4 allowed reducing the equivalent torque ripple percentage to an interval between 1% and 3% for the entire operating speed range of the machine working under the maximum symmetrical motoring and generating torque.

Thanks to the torque ripple modeling and the rotor position error compensation algorithm based on PA, the maximum limit condition of 5% demanded in high-performance EV PMSM-drives has been successfully evaluated and fulfilled.

CHAPTER 4

PERFORMANCE INVESTIGATION OF TWO NOVEL HSFVI DEMODULATION ALGORITHMS FOR ENCODERLESS FOC OF PMSMS INTENDED FOR EV PROPULSION: A DSP-BASED EXPERIMENTAL STUDY

Jorge Lara [a], Ambrish Chandra [b]

[a,b] Department of Electrical Engineering, École de Technologie Supérieure,
1100 Notre-Dame Ouest, Montréal, Québec, Canada H3C 1K3

Article submitted to « IEEE Transactions on Industrial Electronics » on November 2016
Paper Submission Number: 16-TIE-3349

Abstract

This paper investigates the performance of two novel Half Switching Frequency Voltage Injection (HSFVI) demodulation algorithms for encoderless Field Oriented Control (FOC) of Permanent Magnet Synchronous Machines (PMSM) intended for Electric Vehicle (EV) propulsion. The proposed rotating and pulsating HSFVI demodulation algorithms do not require voltage measurements or approximations for estimating the rotor position angle. The proposed HSFVI algorithms based on Pulse Width Modulation (PWM) have been quantitatively and qualitatively compared by MATLAB–SimPowerSystems simulations as well as experimentally against the two equivalent classical High Frequency Signal Injection (HFSI) approaches based on Space Vector Modulation (SVM). A 2.5kW PMSM with radially inset rotor magnets has been used for experimentally evaluating and validating the performance analysis and the comparison of the four algorithms fully implemented to work in real-time on a TI C2000 Digital Signal Processor (DSP). The results obtained with an 80kW Interior (I)-PMSM intended for EV propulsion also show that the proposed algorithms allow a better machine control performance in terms of a smaller torque ripple generation and a faster current control loop.

Index Terms — Electric vehicle (EV), encoderless control, high frequency signal injection (HFSI), permanent magnet synchronous machine (PMSM).

4.1 Introduction

The performance of FOC-PMSMs heavily depends on the accuracy and resolution of the rotor position sensor (Lara et al., 2016a). High quality encoders and resolvers can fulfill this requirement in demanding applications (Lara and Chandra, 2014b) such as PMSM-drives for light and heavy-duty electric vehicle (LHDEV) traction applications (Lara et al., 2016b). Nevertheless, the sensor components are prone to mechanical and electrical failures that can put the vehicle out of service or even lead to severe dangerous scenarios. In this regard, the use of rotor position sensorless algorithms working as a backup of the position sensor can positively contribute to the fault-tolerant and reliability enhancement in LHDEV PMSM-traction drives (Kano et al., 2013).

The High Frequency Signal Injection (HFSI) methods rely on the geometrical and saturation saliency properties of the machine (Ha, 2008). The variation of the high frequency inductances (HFI) as a function of the rotor position makes possible the estimation at standstill as well as in the low-speed range where the Back-Electromotive Force (BEMF)-based algorithms are inherently unsuitable. The HFSI methods are also feasible for the high speed range provided that the HFI are relatively small so that the voltage required from the DC bus for injection purposes is not a concern (Gao et al., 2009; Masaki et al., 2002).

Over the last years, researchers have done a significant step-forward regarding the HFSI algorithms for encoderless FOC of PMSMs. The exhaustive classification presented in (Briz and Degner, 2011) considers important aspects such as the continuity of the excitation, the machine winding connection, the number of sensors required for either voltage or current injection, the frame of coordinates as well as the type of modulation. In Voltage Source Converter (VSC)-based algorithms working with SVM, the injection frequency range commonly varies around 400Hz-1kHz (Ji-Hoon et al., 2004; Ji-Hoon et al., 2003; Lara et al.,

2012; Liu and Zhu, 2014; Luo et al., 2016; Wang et al., 2013; Xu and Zhu, 2016a; 2016b; Yu-seok et al., 2005) whereas in the algorithms working with PWM, the injection frequency is near the switching frequency (Gabriel et al., 2013; Kano et al., 2012; Kim et al., 2016; Kim et al., 2011b; Kim and Sul, 2011; Yoon et al., 2011) or even they become equal (Kim et al., 2011a; 2012; Lara and Chandra, 2014a; Masaki et al., 2002). The frequency range of the injected signal in the methods using PWM is much higher than in those using SVM. This difference is mainly because the HF demodulation algorithms in the PWM-based methods do not involve digital filters. By doing so, the top injection frequency is inherently limited given that for a constant sampling rate, the number of samples decreases as the frequency of the injected signal increases, thus deteriorating the performance of the filters. In order to overcome this issue, the use of analog filters for HF demodulation purposes has been recently proposed in (Jung and Ha, 2015). The PWM modulation is also preferred over SVM when the HF demodulation algorithm is sensitive to the inverter nonlinearities, e.g. the dead-time effect can give rise to a severe deterioration of the rotor position estimation (Briz and Degner, 2011; Gabriel et al., 2013). The use of higher frequencies using PWM-based algorithms is likewise motivated due to the audible nuisance caused by the sound that arises from the vibration of the stator windings of the machine. If the frequency of the injected signal reaches the upper pitch audibility limit of human ear of around 20 kHz, the hassle acoustic frequency can be virtually unnoticeable (Gabriel et al., 2013; Jung and Ha, 2015; Kim et al., 2012).

In previous literature on the subject (Kim et al., 2011a; 2012; Kim et al., 2016; Kim et al., 2011b; Ogasawara and Akagi, 1998; Petrovic et al., 2003), the HF demodulation algorithms working in the stationary reference frame require both voltage and current measurements given that they are based on the inductance matrix of the PMSM model that contains the valuable rotor position information. This dependency on stator voltage measurements makes the demodulation particularly susceptible not only to measurement errors due to the inaccuracy and limited bandwidth of the voltage sensors but to the imprecise extraction and computing of the mean value from the high frequency voltage pulse over a carrier period. A special acquisition system with a sampling frequency much higher than the switching frequency is required to achieve accurate results. Moreover, when the voltage references from the FOC are used instead

of the measured values, the rotor position estimation is inherently degraded given that the nonlinearities of the inverter are fully disregarded. Likewise, the HF sensorless algorithms based on zero-sequence voltage components (ZSVC) (Xu and Zhu, 2016a; 2016b) not only require extra-hardware but access to the neutral point of the machine, which is not typically available in industrial drives (Briz and Degner, 2011). The ZSVC-based methods are inherently unfeasible for implementation in PMSMs with delta-connected windings.

In this paper, authors propose two half switching frequency demodulation algorithms in the stationary and rotating coordinates that advantageously do not require voltage measurements for estimating the rotor position angle. The use of only current measurements sampled with the same sampling rate and the same sensors used for the fundamental currents to perform FOC simplifies its implementation and allows avoiding voltage measurement issues as well as voltage assumptions and approximations. The no need of extra-hardware and the capability of working indistinctly with PMSMs having either delta- or wye-connected windings allow an easier integration of the proposed algorithms with most of the PMSM-drives currently available in industry.

This paper is organized as follows. The classical pulsating and rotating SVM-based HFSI techniques are analyzed in section 4.2 while the proposed PWM-based HSFSI algorithms in both stator and rotor coordinates are presented in section 4.3. Each of these sections includes its respective high-frequency PMSM model and equations that theoretically support the encoderless FOC of the machine. The MATLAB–SimPowerSystems-based simulations and the experimental results obtained with a 2.5kW PMSM having radially inset rotor magnets are shown next to each other along the text of section 4.2 and section 4.3, thus allowing a simultaneous validation and an easier tracing and comprehension of the characteristic waveforms for the different methods. The quantitative and qualitative performance comparison and analysis for the four HFSI sensorless techniques are presented in section 4.4. This section also includes the simulation results obtained from the encoderless FOC of an 80kW IPMSM intended for EV propulsion. Finally, the conclusion and some important remarks are given in section 4.5.

4.2 Model of SVM-based high frequency signal injection for encoderless FOC of PMSM

4.2.1 Pulsating Voltage Signal Injection: dq-HFSVM

The PMSM model in the real dq rotor coordinates is described as follows

$$\begin{bmatrix} V_d \\ V_q \end{bmatrix} = \begin{bmatrix} R_s + \frac{d}{dt}L_d & -\omega_r L_q \\ \omega_r L_d & R_s + \frac{d}{dt}L_q \end{bmatrix} \begin{bmatrix} I_d \\ I_q \end{bmatrix} + \begin{bmatrix} 0 \\ \omega_r \Phi_r \end{bmatrix} \tag{4.1}$$

According to the space vector diagram of Figure 4.1, after applying the voltage and current transformations (4.2) and (4.3) to (4.1) considering the rotor position error $\delta = \theta_r - \theta_r'$

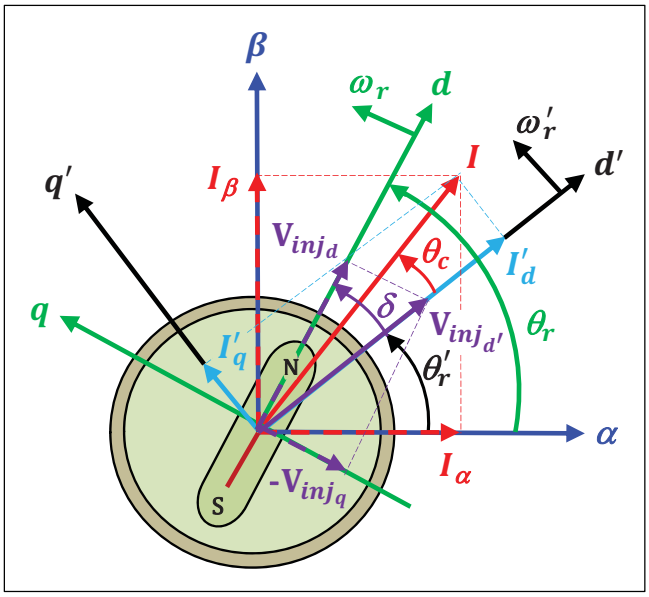

Figure 4.1 Space vector diagram showing the real dq and estimated $d'q'$ rotating reference frames with respect to the stationary abc and $\alpha\beta$ coordinates

$$\begin{bmatrix} V_d' \\ V_q' \end{bmatrix} = \begin{bmatrix} cos(\delta) & -sin(\delta) \\ sin(\delta) & cos(\delta) \end{bmatrix} \begin{bmatrix} V_d \\ V_q \end{bmatrix} \tag{4.2}$$

$$\begin{bmatrix} I_d \\ I_q \end{bmatrix} = \begin{bmatrix} cos(\delta) & sin(\delta) \\ -sin(\delta) & cos(\delta) \end{bmatrix} \begin{bmatrix} I_d' \\ I_q' \end{bmatrix} \tag{4.3}$$

the PMSM model in the estimated $d'q'$ rotor coordinates is written as follows (Lara et al., 2012)

$$\begin{bmatrix} V'_d \\ V'_q \end{bmatrix} = \left\{ R_s + \omega_r \begin{bmatrix} -c_2 & -c_3 \\ c_1 & c_2 \end{bmatrix} + \frac{d}{dt} \begin{bmatrix} c_1 & c_2 \\ c_2 & c_3 \end{bmatrix} \right\} \begin{bmatrix} I'_d \\ I'_q \end{bmatrix} + \omega_r \Phi_r \begin{bmatrix} -sin(\delta) \\ cos(\delta) \end{bmatrix} \tag{4.4}$$

$$c_1 = [\Sigma L + \Delta L \, cos(2\delta)] \tag{4.5}$$

$$c_2 = \Delta L \, sin(2\delta) \tag{4.6}$$

$$c_3 = [\Sigma L - \Delta L \, cos(2\delta)] \tag{4.7}$$

where $\Sigma L = (L_d + L_q)/2$ and $\Delta L = (L_d - L_q)/2$. If the high frequency voltage signal is injected on the estimated d'-axis as follows

$$\begin{bmatrix} V'_{d_{hf}} \\ V'_{q_{hf}} \end{bmatrix} = \begin{bmatrix} V_{inj} \, cos(\omega_{hf} t) \\ 0 \end{bmatrix} \tag{4.8}$$

and assuming $R_s \ll Z_{hf}$ and $\omega_{hf} \gg \omega_r$, the high frequency estimated currents flowing through the PMSM stator windings are given by

$$\begin{bmatrix} I'_{d_{hf}} \\ I'_{q_{hf}} \end{bmatrix} = \frac{1}{L_{d_{hf}} L_{q_{hf}}} \begin{bmatrix} \Sigma L_{hf} - \Delta L_{hf} \, cos(2\delta) & -\Delta L_{hf} \, sin(2\delta) \\ -\Delta L_{hf} \, sin(2\delta) & \Sigma L_{hf} + \Delta L_{hf} \, cos(2\delta) \end{bmatrix} \int \begin{bmatrix} V'_{d_{hf}} \\ V'_{q_{hf}} \end{bmatrix} dt \tag{4.9}$$

By substituting (4.8) into (4.9), the relation between the rotor position error and the high frequency currents is described as

$$\begin{bmatrix} I'_{d_{hf}} \\ I'_{q_{hf}} \end{bmatrix} = \frac{V_{inj} \, sin(\omega_{hf} t)}{L_{d_{hf}} L_{q_{hf}} \omega_{hf}} \begin{bmatrix} \Sigma L_{hf} - \Delta L_{hf} \, cos(2\delta) \\ -\Delta L_{hf} \, sin(2\delta) \end{bmatrix} \tag{4.10}$$

In order to estimate the rotor position from $I'_{q_{hf}}$ in (4.10), the heterodyning demodulation process shown in Figure 4.2 is used (Al-nabi et al., 2013; Foo and Rahman, 2010; Ji-Hoon et al., 2004; Ji-Hoon et al., 2003). If assuming $2\delta \approx 0 \rightarrow \sin(2\delta) \approx 2\delta$, then the rotor position error function obtained after the LPF is finally written as

$$f(\delta) \approx \left[\frac{-\Delta L_{hf} V_{inj}}{L_{d\,hf} L_{q\,hf} \omega_{hf}}\right] \delta \tag{4.11}$$

By controlling $f(\delta)$ to zero, the estimated rotor position is kept close to the real one, i.e. $\delta \approx 0$, and thereby making possible the encoderless FOC of PMSM.

Figure 4.2 presents the demodulation algorithm for exploiting the property described in (4.11) whereas Figure 4.3 shows the encoderless FOC of PMSM using the estimated rotor position θ_r'.

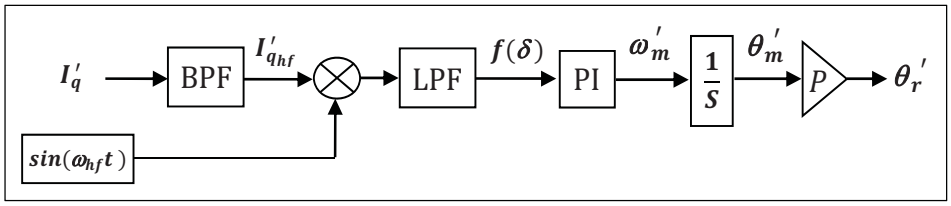

Figure 4.2 Demodulation structure used for the SVM-based HFSI technique in the estimated rotating reference frame $d'q'$

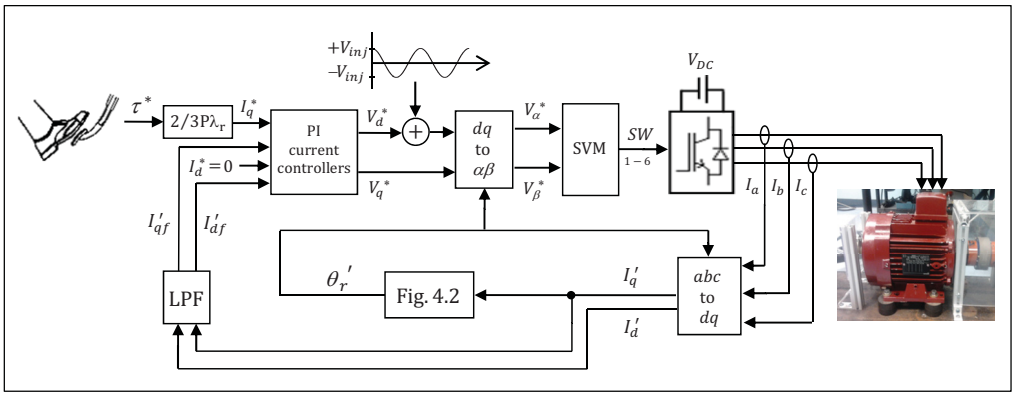

Figure 4.3 Encoderless FOC strategy of PMSM using the SVM-based HFSI technique in the estimated rotating reference frame $d'q'$

Figure 4.4 shows the 2.5kW PMSM used for experimentally validating the four HFSI techniques presented in this paper. It can be observed the eight permanent magnets radially inset in the rotor as well as the identification of the d and q axes. The machine parameters and the description of the full experimental setup are presented in the Appendix III.

Figure 4.4 Four-pole pairs PMSM used in experiments for testing the HFSI techniques. The permanent magnets are radially inset in the rotor

The high frequency inductance curves of Fig. 4.5 have been obtained following the procedure reported by (Ji-Hoon et al., 2003). According to the results shown in this figure, the difference between the high frequency direct $L_{d_{hf}}$ and quadrature $L_{q_{hf}}$ inductances at 555Hz is only 17%. However, such a small inductance variation has been enough to achieve acceptable FOC-PMSM performance even under maximum torque conditions.

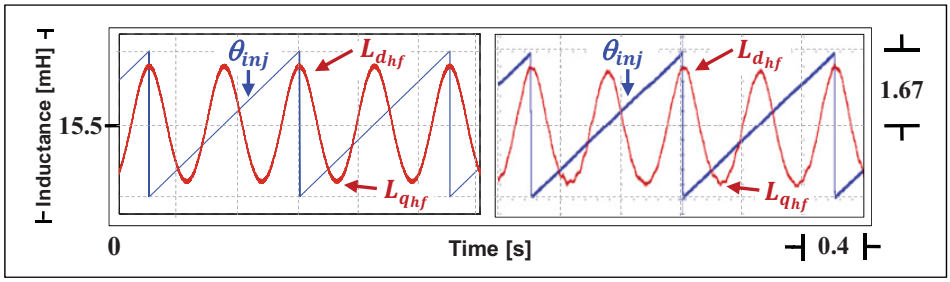

Figure 4.5 Inductance variation as a function of the injection angle θ_{inj}. Measurements carried out under no load and setting V_{inj}= 21.6V_{pk} , f_{inj}= 555Hz and f_s= 5 kHz (Left) Simulation (Right) Experimental

Figure 4.6 shows the characteristic waveforms of the dq-HFSVM injection technique. These results have been obtained by changing the injection angle θ_{inj} of V_{inj} according to a ramp profile, thereby scanning the saliency properties of the machine along a full electrical cycle while the rotor remains at standstill (Holtz, 2008). It can be observed the good matching between the simulation and experimental results as well as the modeling validation of the high frequency currents $I'_{d_{hf}}$ and $I'_{q_{hf}}$ from (4.10) and the error function $f(\delta)$ from (4.11) obtained using the demodulation structure of Figure 4.2.

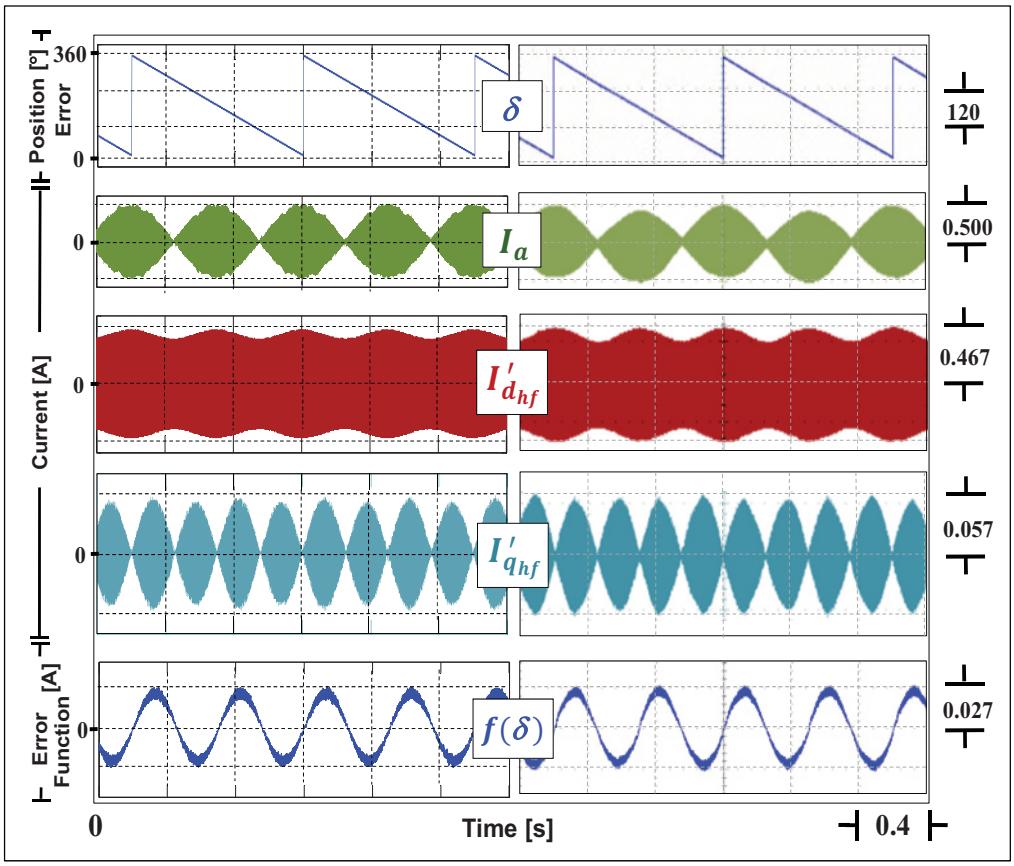

Figure 4.6 Results for the dq-HFSVM under no load at standstill
(Left) Simulation (Right) Experimental

The results of Figure 4.7 alike validate the premise that by controlling $f(\delta)$ to zero through a PI controller as in Figure 4.2, $I'_{q_{hf}}$ is also kept around zero and the estimated position θ'_r allows the encoderless FOC of the PMSM.

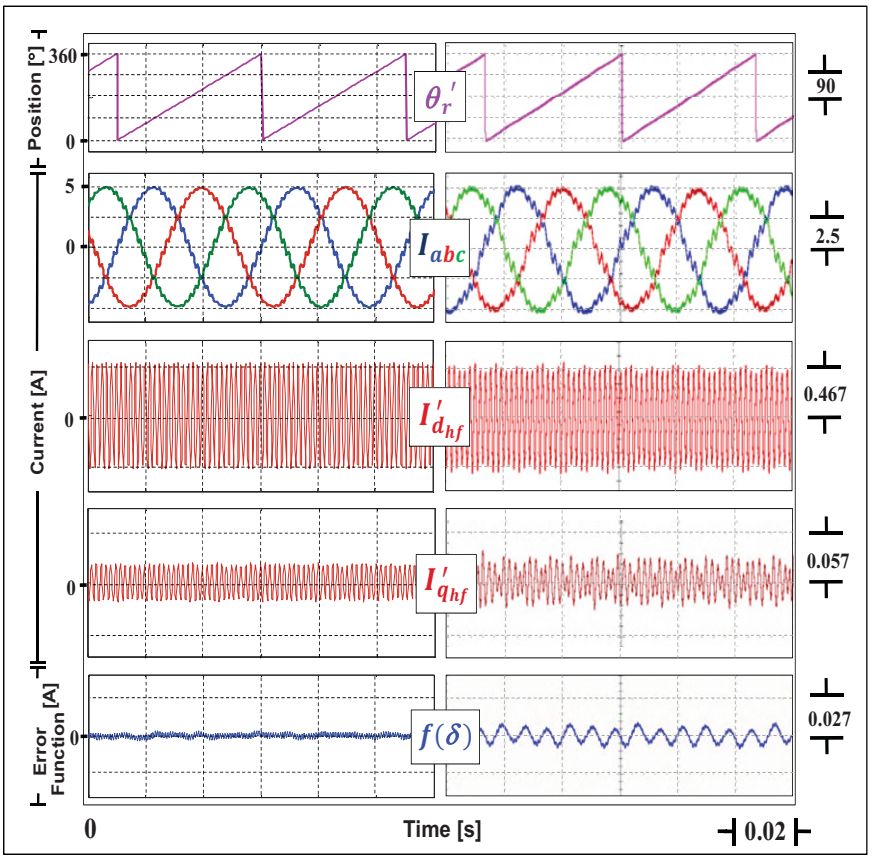

Figure 4.7 Results for the dq-HFSVM under full load torque of 9 N·m at $\omega_r^* = 300$ rpm (Left) Simulation (Right) Experimental

4.2.2 Rotating Voltage Signal Injection: $\alpha\beta$ - HFSVM

The PMSM model in the stationary reference frame is described as follows (Kim et al., 2012; Lara and Chandra, 2014a)

$$\begin{bmatrix} V_\alpha \\ V_\beta \end{bmatrix} = R_s \begin{bmatrix} I_\alpha \\ I_\beta \end{bmatrix} + \frac{d}{dt} L_s \begin{bmatrix} I_\alpha \\ I_\beta \end{bmatrix} + \Phi_r \frac{d}{dt} \begin{bmatrix} cos(\theta_r) \\ sin(\theta_r) \end{bmatrix} \tag{4.12}$$

where the inductance matrix L_s is defined as

$$L_s = \begin{bmatrix} \Sigma L + \Delta L\, cos(2\theta_r) & \Delta L\, sin(2\theta_r) \\ \Delta L\, sin(2\theta_r) & \Sigma L - \Delta L\, cos(2\theta_r) \end{bmatrix} \tag{4.13}$$

Applying the derivative operator in (4.12), it is written as

$$\begin{bmatrix} V_\alpha \\ V_\beta \end{bmatrix} = R_s \begin{bmatrix} I_\alpha \\ I_\beta \end{bmatrix} + L_s \frac{d}{dt} \begin{bmatrix} I_\alpha \\ I_\beta \end{bmatrix} + 2\Delta L\, \omega_r L_n \begin{bmatrix} I_\alpha \\ I_\beta \end{bmatrix} + \Phi_r \omega_r \begin{bmatrix} -sin(\theta_r) \\ cos(\theta_r) \end{bmatrix} \tag{4.14}$$

$$L_n = \begin{bmatrix} -sin(2\theta_r) & cos(2\theta_r) \\ cos(2\theta_r) & sin(2\theta_r) \end{bmatrix} \tag{4.15}$$

If the high frequency voltage signal vector is injected on the $\alpha\beta$-axis as follows

$$\begin{bmatrix} V_{\alpha_{hf}} \\ V_{\beta_{hf}} \end{bmatrix} = V_{inj} \begin{bmatrix} cos(\omega_{hf} t\,) \\ sin(\omega_{hf} t\,) \end{bmatrix} \tag{4.16}$$

and assuming $R_s \ll Z_{hf}$ and $\omega_{hf} \gg \omega_r$, the high frequency currents flowing through the PMSM stator windings are given by

$$\begin{bmatrix} I_{\alpha_{hf}} \\ I_{\beta_{hf}} \end{bmatrix} = \frac{1}{L_{d_{hf}} L_{q_{hf}}} \begin{bmatrix} \Sigma L_{hf} - \Delta L_{hf}\, cos(2\theta_r\,) & -\Delta L_{hf}\, sin(2\theta_r\,) \\ -\Delta L_{hf}\, sin(2\theta_r\,) & \Sigma L_{hf} + \Delta L_{hf}\, cos(2\theta_r\,) \end{bmatrix} \int \begin{bmatrix} V_{\alpha_{hf}} \\ V_{\beta_{hf}} \end{bmatrix} dt \tag{4.17}$$

By substituting (4.16) into (4.17), the relation between the rotor position and the high frequency currents is described as

$$\begin{bmatrix} I_{\alpha_{hf}} \\ I_{\beta_{hf}} \end{bmatrix} = \frac{V_{inj}}{L_{d_{hf}} L_{q_{hf}} \omega_{hf}} \begin{bmatrix} \Sigma L_{hf}\, sin(\omega_{hf} t\,) - \Delta L_{hf} sin\big(\omega_{hf} t - 2\theta_r\big) \\ -\Sigma L_{hf}\, cos(\omega_{hf} t\,) - \Delta L_{hf} cos\big(\omega_{hf} t - 2\theta_r\big) \end{bmatrix} \tag{4.18}$$

In order to estimate the rotor position from (4.18), the heterodyning demodulation process shown in Figure 4.8 is used (Jansen and Lorenz, 1995; Kim et al., 2011a; 2012; Kim et al., 2016; Kim and Sul, 2011). By assuming $2\delta \approx 0 \rightarrow \sin(2\delta) \approx 2\delta$, the rotor position error function $f(\delta)$ obtained after the LPF is given by

$$f(\delta) \approx \left[\frac{2\Delta L_{hf} V_{inj}}{L_{d_{hf}} L_{q_{hf}} \omega_{hf}} \right] \delta \tag{4.19}$$

Figure 4.8 presents the demodulation algorithm for exploiting the relation described in (4.19) whereas Figure 4.9 shows the encoderless FOC of PMSM using the estimated rotor position θ_r'.

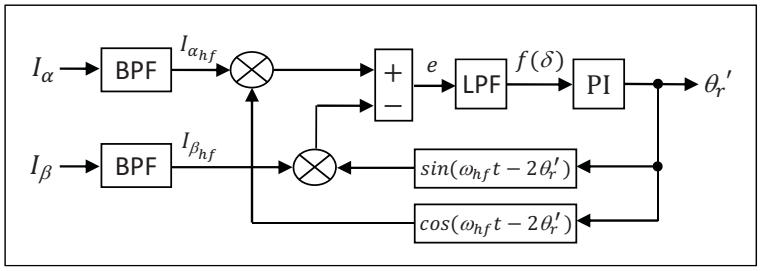

Figure 4.8 Demodulation structure used for the SVM-based HFSI technique in the stationary reference frame $\alpha\beta$

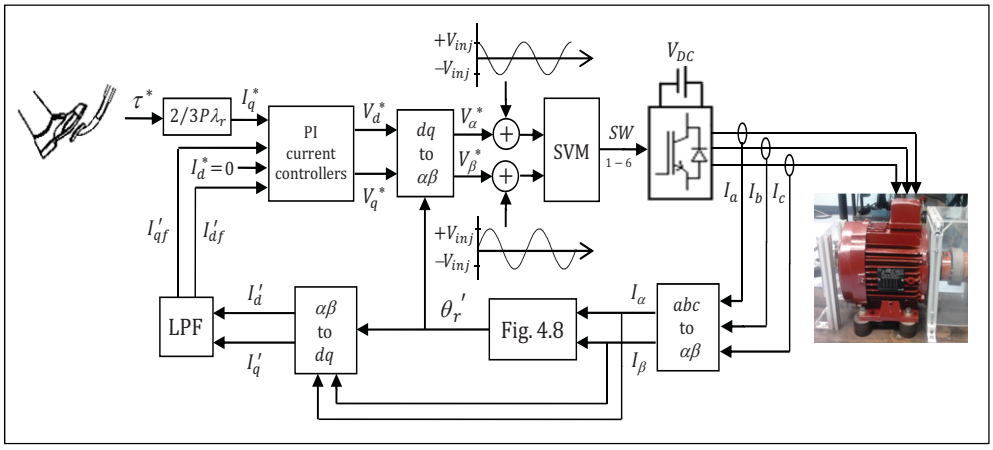

Figure 4.9 Encoderless FOC strategy of PMSM using the SVM-based HFSI technique in the stationary reference frame $\alpha\beta$

The characteristic waveforms of the $\alpha\beta$-HFSVM injection technique shown in Figure 4.10 validate the modeling of the high frequency currents $I_{\alpha_{hf}}$ and $I_{\beta_{hf}}$ from (4.18) as well as the error function $f(\delta)$ from (4.19) obtained using the demodulation structure of Figure 4.8. The results of Figure 4.11 alike validate the premise that by controlling $f(\delta)$ to zero through the PI controller of Figure 4.8, the estimated rotor position θ_r' allows the encoderless FOC of the PMSM.

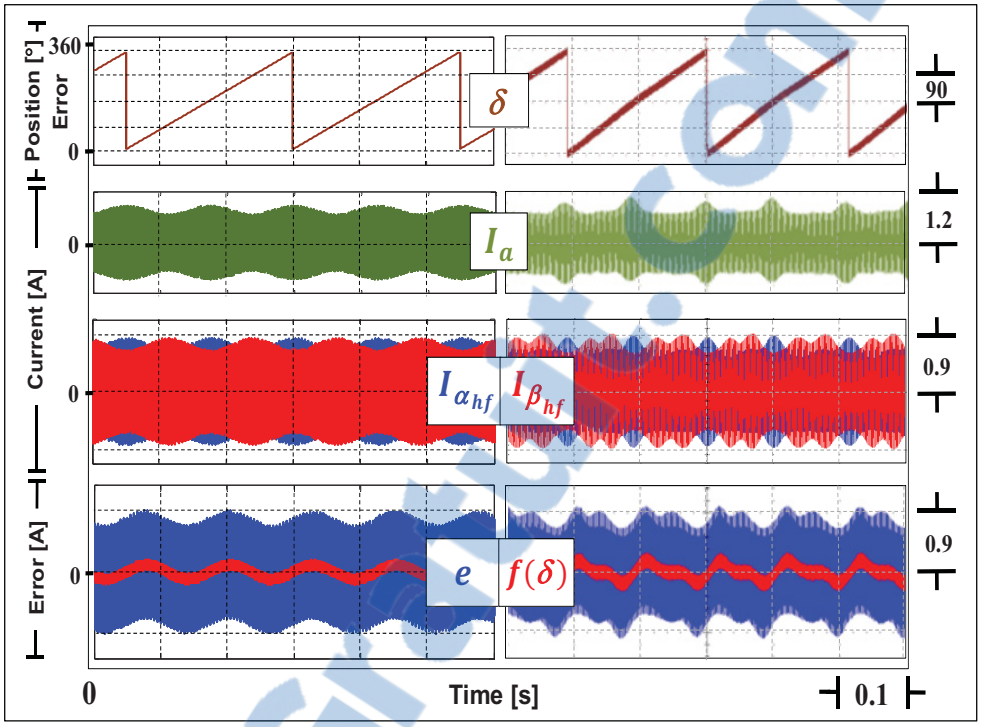

Figure 4.10 Results for the $\alpha\beta$-HFSVM under no load at $\omega_r^* = 60$rpm (Left) Simulation (Right) Experimental

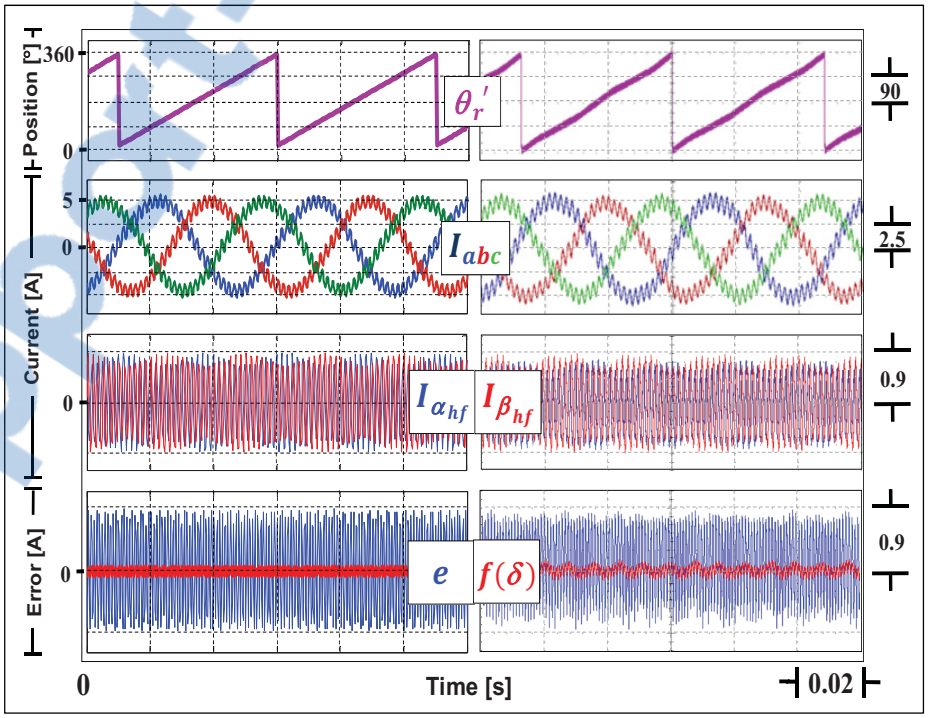

Figure 4.11 Results for the $\alpha\beta$-HFSVM under full load torque of 9 N·m at $\omega_r^* = 300$ rpm (Left) Simulation (Right) Experimental

4.3 Model of PWM-based half switching frequency signal injection for encoderless FOC of PMSM

4.3.1 Rotating Voltage Signal Injection: $\alpha\beta$ - HSFPWM

The proposed injection pattern in the stationary reference frame is shown in Figure 4.12. The voltage vectors V_1 and V_2 are composed by the fundamental component V_m that controls the machine as well as by the half PWM carrier frequency formed by the voltages $+V_{inj}$ and $-V_{inj}$ injected at the times T_k and T_{k+1}, respectively. The current sampling time interval $\Delta T_k = \Delta T_{k+1}$ is considered small enough so that the following assumptions are valid during two consecutive PWM periods: a) the machine parameters remain constant b) the fundamental current component changes linearly c) the change in rotor position is negligible at low speeds and d) the change in rotor speed is negligible in high inertia machine shafts.

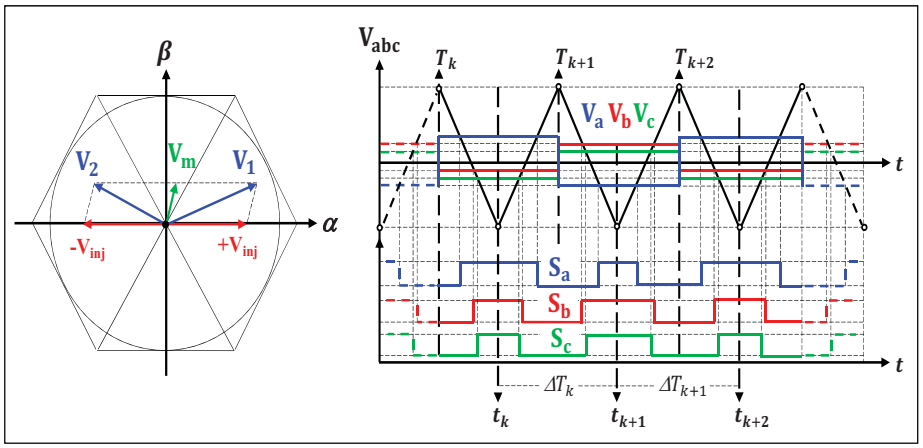

Figure 4.12 Voltage references in the spatial $\alpha\beta$ and temporal abc frames. The switching signals S_{abc} and the current sampling instants t_k are also shown

Solving for the time derivative of currents in (4.14)-(4.15), the PMSM model is expressed as follows

$$\frac{d}{dt}\begin{bmatrix} I_\alpha \\ I_\beta \end{bmatrix} = \frac{1}{L_d L_q}\left\{[M_1]\left[\begin{bmatrix} V_\alpha \\ V_\beta \end{bmatrix} - R_s\begin{bmatrix} I_\alpha \\ I_\beta \end{bmatrix} + \omega_r \Phi_r \begin{bmatrix} -sin(\theta_r) \\ cos(\theta_r) \end{bmatrix}\right] - 2\omega_r \Delta L[M_2]\begin{bmatrix} I_\alpha \\ I_\beta \end{bmatrix}\right\} \quad (4.20)$$

where the matrices M_1 and M_2 are defined as

$$M_1 = \begin{bmatrix} \Sigma L - \Delta L\, cos(2\theta_r) & -\Delta L\, sin(2\theta_r) \\ -\Delta L\, sin(2\theta_r) & \Sigma L + \Delta L\, cos(2\theta_r) \end{bmatrix} \tag{4.21}$$

$$M_2 = \begin{bmatrix} -\Sigma L\, sin(2\theta_r) & -\Delta L + \Sigma L\, cos(2\theta_r) \\ \Delta L + \Sigma L cos(2\theta_r) & \Sigma L\, sin(2\theta_r) \end{bmatrix} \tag{4.22}$$

By replacing the continuous derivative operator with the discretized notation, the stator current difference ΔI in the interval ΔT_k is express as follows

$$\begin{bmatrix} \Delta I_\alpha^{\Delta T_k} \\ \Delta I_\beta^{\Delta T_k} \end{bmatrix} = \frac{\Delta T_k}{L_d^{\Delta T_k} L_q^{\Delta T_k}} \left\{ [M_1]^{\Delta T_k} \left[\begin{bmatrix} V_\alpha^{\Delta T_k} \\ V_\beta^{\Delta T_k} \end{bmatrix} - R_s^{\Delta T_k} \begin{bmatrix} I_\alpha^{\Delta T_k} \\ I_\beta^{\Delta T_k} \end{bmatrix} + \omega_r^{\Delta T_k} \Phi_r^{\Delta T_k} \begin{bmatrix} sin(\theta_r^{\Delta T_k}) \\ -cos(\theta_r^{\Delta T_k}) \end{bmatrix} \right] - 2\,\omega_r^{\Delta T_k} \Delta L^{\Delta T_k} [M_2]^{\Delta T_k} \begin{bmatrix} I_\alpha^{\Delta T_k} \\ I_\beta^{\Delta T_k} \end{bmatrix} \right\} \tag{4.23}$$

By considering V_m constant during two consecutive PWM periods and injecting $|V_{inj}|$ at the angle θ_{inj}, the HF stator current difference between the first two intervals is given by

$$\begin{bmatrix} \Delta I_\alpha^{\Delta T_k} - \Delta I_\alpha^{\Delta T_{k+1}} \\ \Delta I_\beta^{\Delta T_k} - \Delta I_\beta^{\Delta T_{k+1}} \end{bmatrix} = \frac{2\Delta T V_{inj}}{L_{d_{hf}} L_{q_{hf}}} \begin{bmatrix} M_{1_{hf}} \end{bmatrix} \begin{bmatrix} cos(\theta_{inj}) \\ sin(\theta_{inj}) \end{bmatrix} \tag{4.24}$$

After applying some trigonometric identities in (4.24), it is reduced to (Masaki et al., 2002)

$$\begin{bmatrix} \Delta I_\alpha^{[\Delta T_k - \Delta T_{k+1}]} \\ \Delta I_\beta^{[\Delta T_k - \Delta T_{k+1}]} \end{bmatrix} = \frac{2\Delta T V_{inj}}{L_{d_{hf}} L_{q_{hf}}} \begin{bmatrix} \Sigma L_{hf}\, cos(\theta_{inj}) - \Delta L_{hf}\, cos(2\theta_r - \theta_{inj}) \\ \Sigma L_{hf}\, sin(\theta_{inj}) - \Delta L_{hf}\, sin(2\theta_r - \theta_{inj}) \end{bmatrix} \tag{4.25}$$

It can be noted that both current differences contain the valuable rotor position information. Solving for twice the real rotor position in (4.25), the following expression is obtained

$$2\theta_r = \theta_{inj} + atan\left[\frac{(L_{d_{hf}}L_{q_{hf}})\Delta I_{\beta}^{[\Delta T_k - \Delta T_{k+1}]} - 2\Delta T V_{inj}\Sigma L_{hf} sin(\theta_{inj})}{(L_{d_{hf}}L_{q_{hf}})\Delta I_{\alpha}^{[\Delta T_k - \Delta T_{k+1}]} - 2\Delta T V_{inj}\Sigma L_{hf} cos(\theta_{inj})}\right] \quad (4.26)$$

Given that in practice, the theoretical real position θ_r becomes into the approximation $\widetilde{\theta_r}$ and bearing in mind that $\theta_{inj} \in \{0,\pi\}$, (4.26) is simplified as

$$2\widetilde{\theta_r} = \theta_{inj} + atan\left[\frac{\Delta I_{\beta}^{[\Delta T_k - \Delta T_{k+1}]}}{\Delta I_{\alpha}^{[\Delta T_k - \Delta T_{k+1}]} + sign(V_{inj})\cdot K_{\alpha\beta}}\right] \quad (4.27)$$

where

$$K_{\alpha\beta} = \frac{2\Delta T V_{inj}\Sigma L_{hf}}{L_{d_{hf}}L_{q_{hf}}} \quad (4.28)$$

Figure 4.13 presents the demodulation algorithm for exploiting the relation described in (4.27) whereas Figure 4.14 shows the encoderless FOC of PMSM using the rotor position approximation $\widetilde{\theta_r}$. Note that the PLL is required to derive $\widetilde{\theta_r}$ from the double angle input position. A Luenberger observer or a state filter can also be used for this purpose (Kim et al., 2012; Kim and Sul, 2011). In any case, the gain feedback must be set to 2, in order to get half in the forward path. Advantageously, a well-designed type-2 PLL with speed feedforward compensation can also in turn fairly reduce the periodical position error as the speed increases as well as the offset position error that arises during acceleration and deceleration (Lara et al., 2016b).

The high frequency inductance curves of Fig. 4.15 have been obtained following the procedure reported by (Ji-Hoon et al., 2003). According to the results shown in this figure, the difference between the high frequency direct $L_{d_{hf}}$ and quadrature $L_{q_{hf}}$ inductances at 2.5 kHz is around 32%. This higher inductance variation compared to the 555Hz injection case has allowed achieving a better FOC-PMSM performance for the same tests under maximum torque conditions.

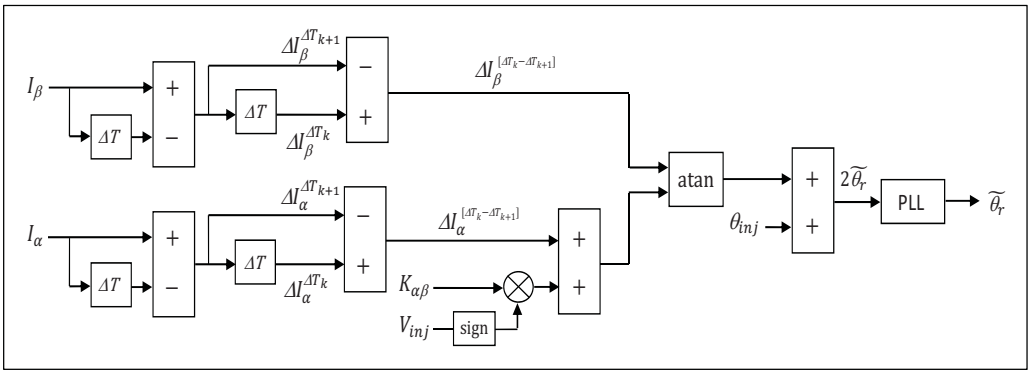

Figure 4.13 Demodulation structure used for the PWM-based HSFSI technique in the stationary reference frame $\alpha\beta$

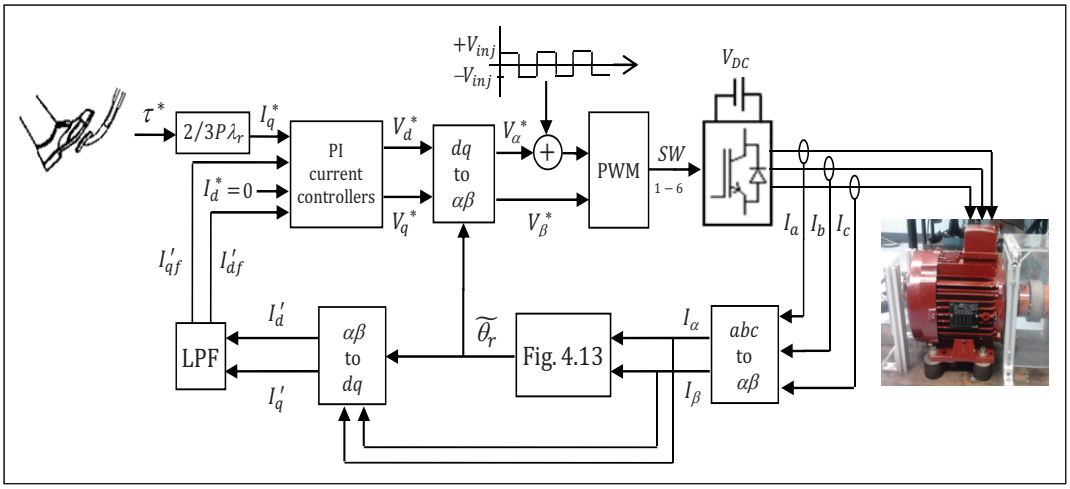

Figure 4.14 Encoderless FOC strategy of PMSM using the PWM-based HSFSI technique in the stationary reference frame $\alpha\beta$

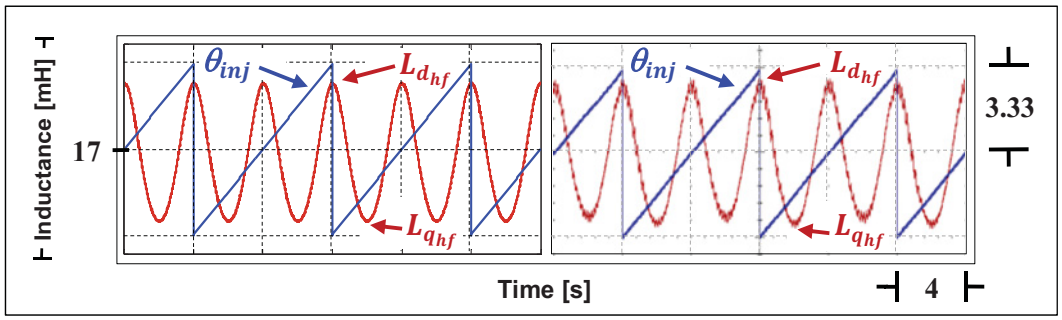

Figure 4.15 Inductance variation as a function of the injection angle θ_{inj}. Measurements carried out under no load and setting V_{inj}= 50.0V$_{pk}$, f_{inj}= 2.5kHz and f_s = 12.5 kHz (Left) Simulation (Right) Experimental

The characteristic waveforms of the $\alpha\beta$-HSFPWM injection technique shown in Figure 4.16 validate the modeling of the high frequency currents $\Delta I_{\alpha}^{[\Delta T_k - \Delta T_{k+1}]}$ and $\Delta I_{\beta}^{[\Delta T_k - \Delta T_{k+1}]}$ from (4.25) that allow calculating the rotor position approximation $\widetilde{\theta_r}$ as of (4.27)-(4.28). The results of Figure 4.17 show the performance of the encoderless FOC using $\widetilde{\theta_r}$ while the PMSM develops its maximum motoring torque.

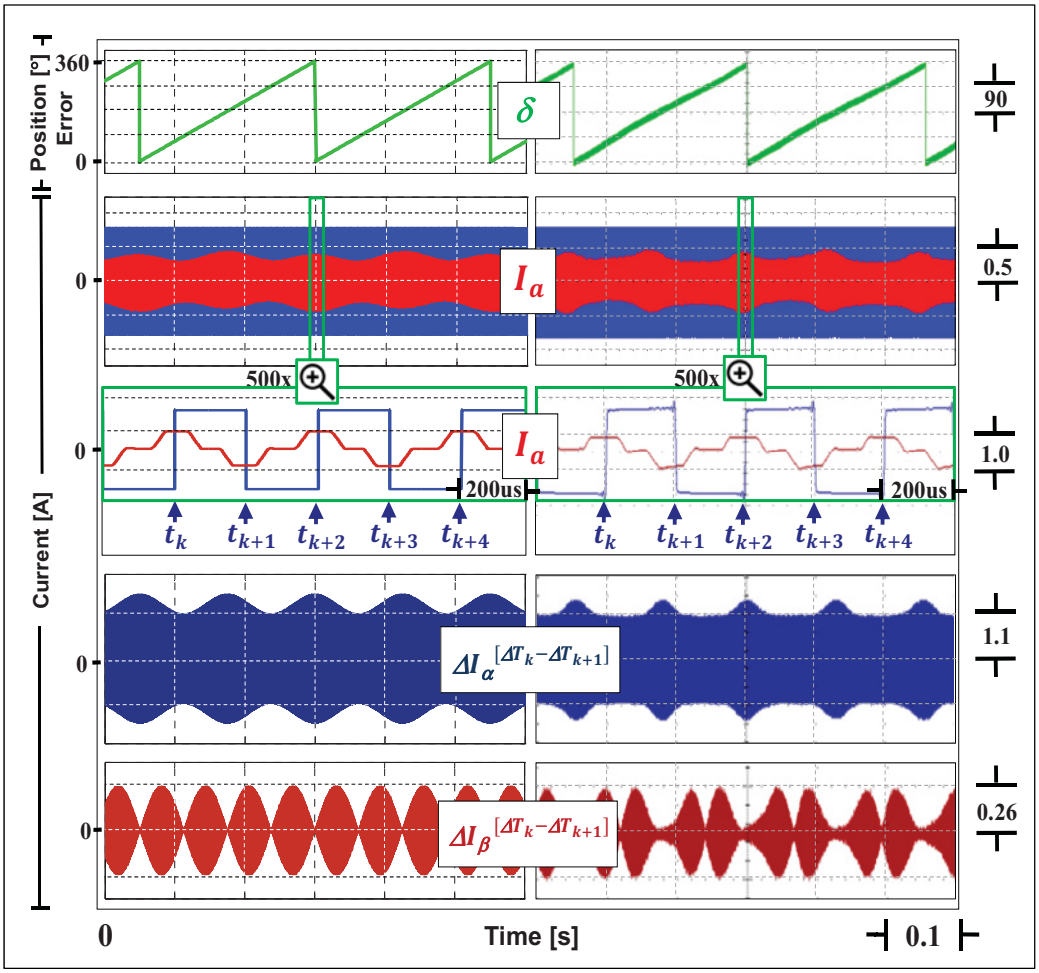

Figure 4.16 Results for the $\alpha\beta$-HSFPWM under no load at $\omega_r^* = 60$rpm. It can be observed the current sampling instants t_k in the 500x zoom-in graphs (Left) Simulation (Right) Experimental

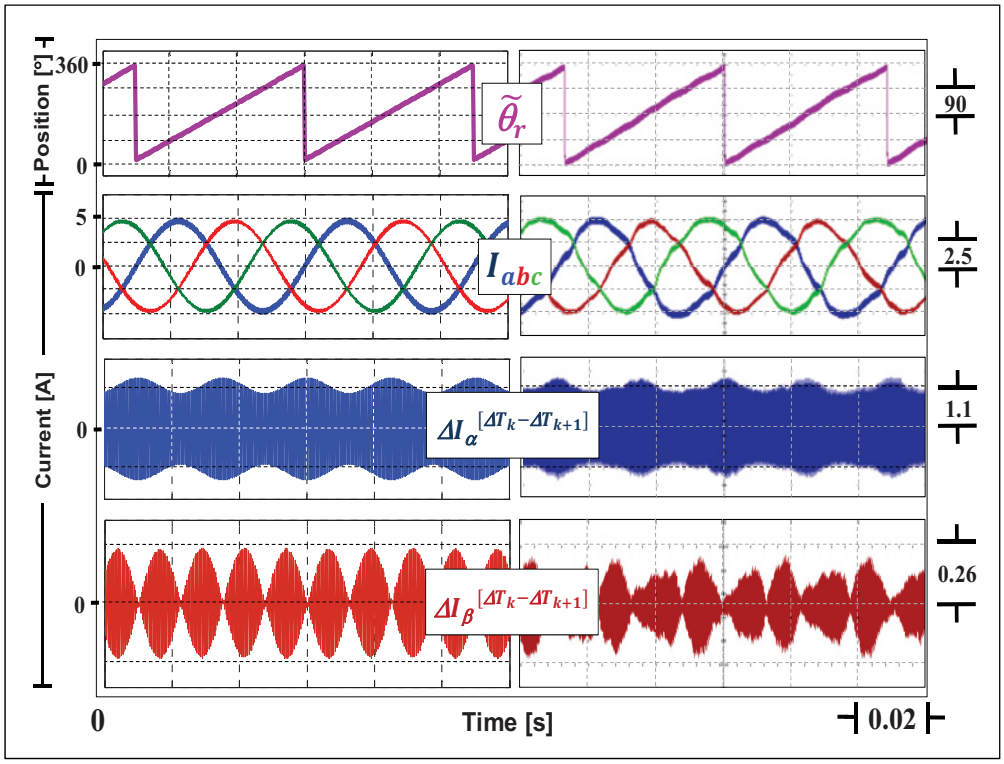

Figure 4.17 Results for the $\alpha\beta$-HSFPWM under full torque of 9 N·m at ω_r^* =300rpm (Left) Simulation (Right) Experimental

4.3.2 Pulsating Voltage Signal Injection: dq - HSFPWM

By transforming the current variables in (4.25) from the stationary $\alpha\beta$ reference frame to the real dq rotating reference frame using (4.29)

$$\begin{bmatrix} I_d \\ I_q \end{bmatrix} = \begin{bmatrix} cos(\theta_r) & sin(\theta_r) \\ -sin(\theta_r) & cos(\theta_r) \end{bmatrix} \begin{bmatrix} I_\alpha \\ I_\beta \end{bmatrix} \tag{4.29}$$

and replacing $\theta_r - \theta_{inj}$ with δ, the following expression is obtained

$$\begin{bmatrix} \Delta I_d^{[\Delta T_k - \Delta T_{k+1}]} \\ \Delta I_q^{[\Delta T_k - \Delta T_{k+1}]} \end{bmatrix} = \frac{2\Delta T V_{inj}}{L_{d_{hf}} L_{q_{hf}}} \begin{bmatrix} \left(\Sigma L_{hf} - \Delta L_{hf}\right) cos(\delta) \\ -\left(\Sigma L_{hf} + \Delta L_{hf}\right) sin(\delta) \end{bmatrix} \tag{4.30}$$

By transforming the current variables in (4.30) to the estimated $d'q'$ rotating reference frame using (4.31)

$$\begin{bmatrix} I'_d \\ I'_q \end{bmatrix} = \begin{bmatrix} cos(\delta) & -sin(\delta) \\ sin(\delta) & cos(\delta) \end{bmatrix} \begin{bmatrix} I_d \\ I_q \end{bmatrix} \tag{4.31}$$

the differences of current are given by

$$\begin{bmatrix} \Delta I'_d{}^{[\Delta T_k - \Delta T_{k+1}]} \\ \Delta I'_q{}^{[\Delta T_k - \Delta T_{k+1}]} \end{bmatrix} = \frac{2\Delta T V_{inj}}{L_{d_{hf}} L_{q_{hf}}} \begin{bmatrix} \Sigma L_{hf} - \Delta L_{hf}\, cos(2\delta) \\ -\Delta L_{hf}\, sin(2\delta) \end{bmatrix} \tag{4.32}$$

Solving for δ in (4.32) using both the direct and quadrature components and assuming $2\delta \approx 0 \rightarrow \tan(2\delta) \approx 2\delta$, then the rotor position error function is given by

$$f(\delta) = \frac{\Delta I'_q}{2\Delta I'_d - K_{dq}} \tag{4.33}$$

where

$$K_{dq} = \frac{4\Delta T V_{inj} \Sigma L_{hf}}{L_{d_{hf}} L_{q_{hf}}} \tag{4.34}$$

By controlling the magnitude of $f(\delta)$ to zero, the estimated rotor position is kept close to the real one, i.e. $\delta \approx 0$, thus making possible the encoderless FOC of the PMSM. Figure 4.18 presents the demodulation algorithm for exploiting the relation described in (4.33) whereas Figure 4.19 shows the encoderless FOC of PMSM using the estimated rotor position θ_r'.

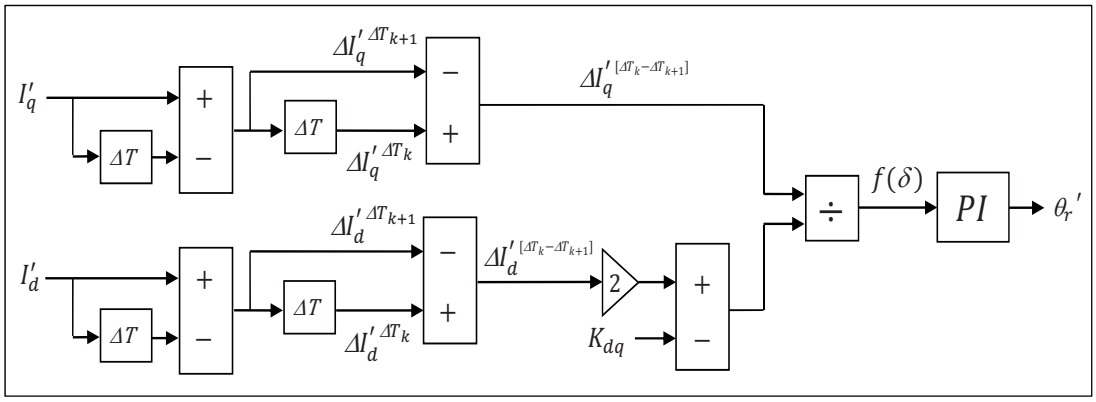

Figure 4.18 Demodulation structure used for the PWM-based HSFSI technique in the estimated rotating reference frame $d'q'$

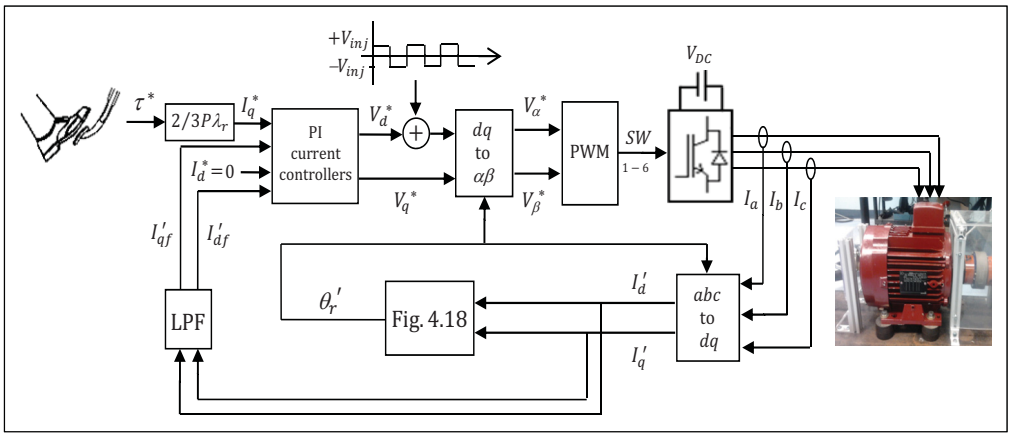

Figure 4.19 Encoderless FOC strategy of PMSM using the PWM-based HSFSI technique in the estimated rotating reference frame $d'q'$

The characteristic waveforms of the dq-HSFPWM injection technique shown in Figure 4.20 validate the modeling of the high frequency currents $\Delta I_d'^{[\Delta T_k - \Delta T_{k+1}]}$ and $\Delta I_q'^{[\Delta T_k - \Delta T_{k+1}]}$ from (4.32) as well as the error function $f(\delta)$ from (4.33) obtained using the demodulation structure of Figure 4.18.

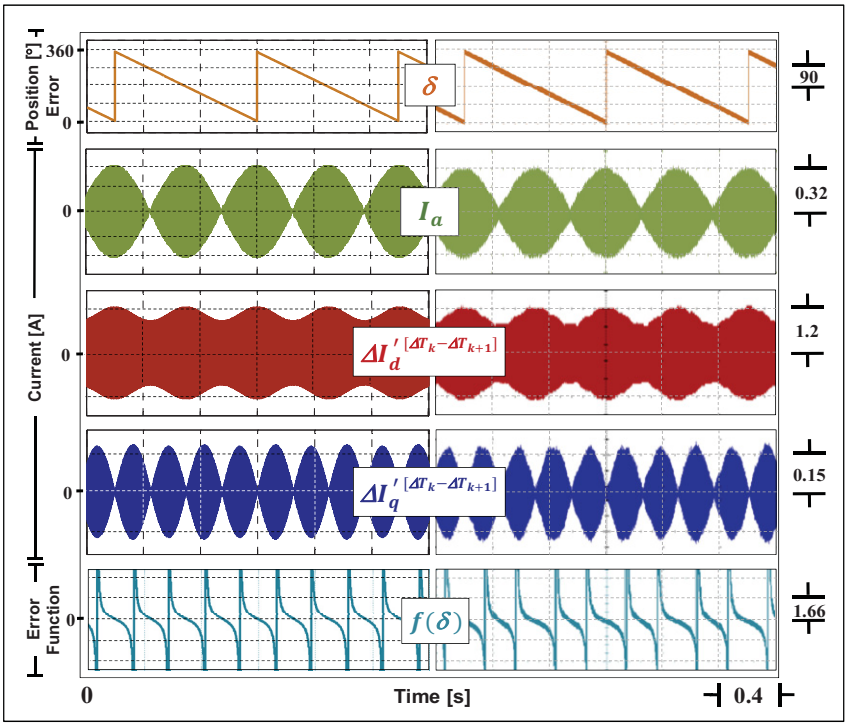

Figure 4.20 Results for the dq-HSFPWM under no load at standstill (Left) Simulation (Right) Experimental

The results of Figure 4.21 show the performance of the encoderless FOC using θ_r' while the PMSM develops its maximum motoring torque.

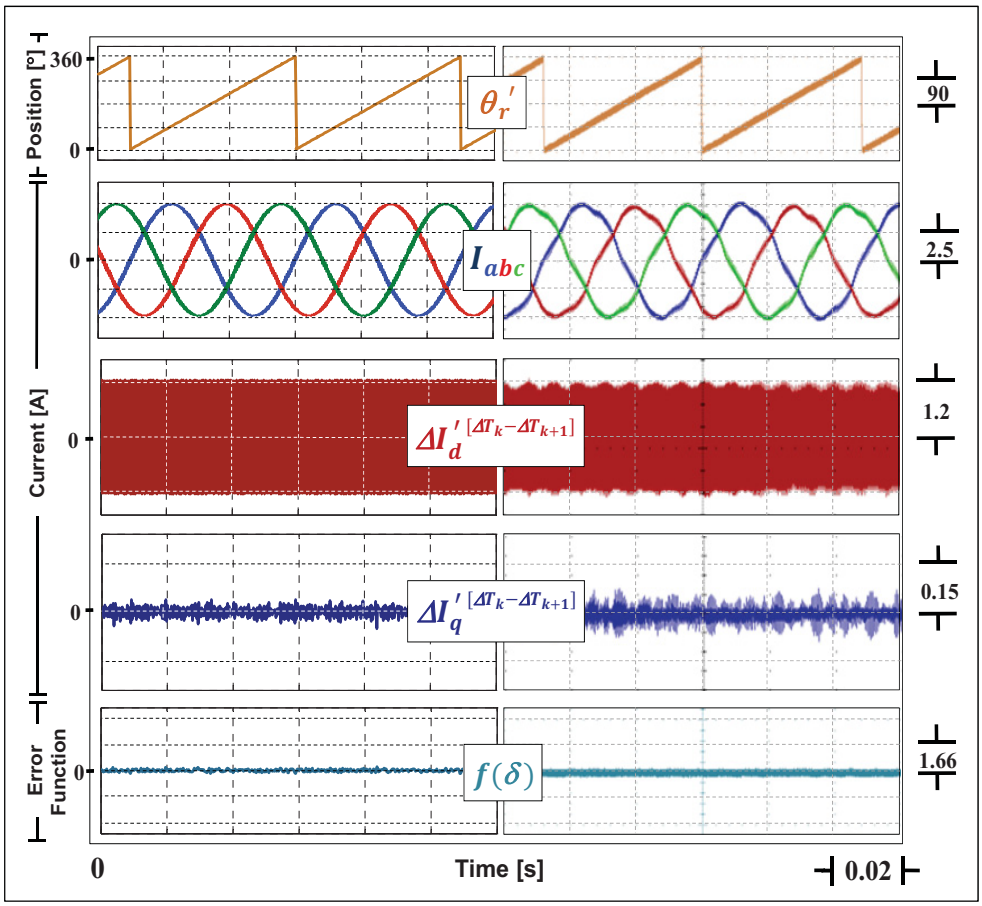

Figure 4.21 Results for the dq-HSFPWM under full load torque of 9 N·m at $\omega_r^* = 300$rpm (Left) Simulation (Right) Experimental

4.4 Analysis and performance comparison of the four HFSI techniques

The periodical rotor position error obtained for the four HFSI techniques at 300rpm under no load is shown in Figure 4.22. It can be observed that the dq-HSFPWM and the $\alpha\beta$-HFSVM techniques present the smallest and the biggest error, respectively.

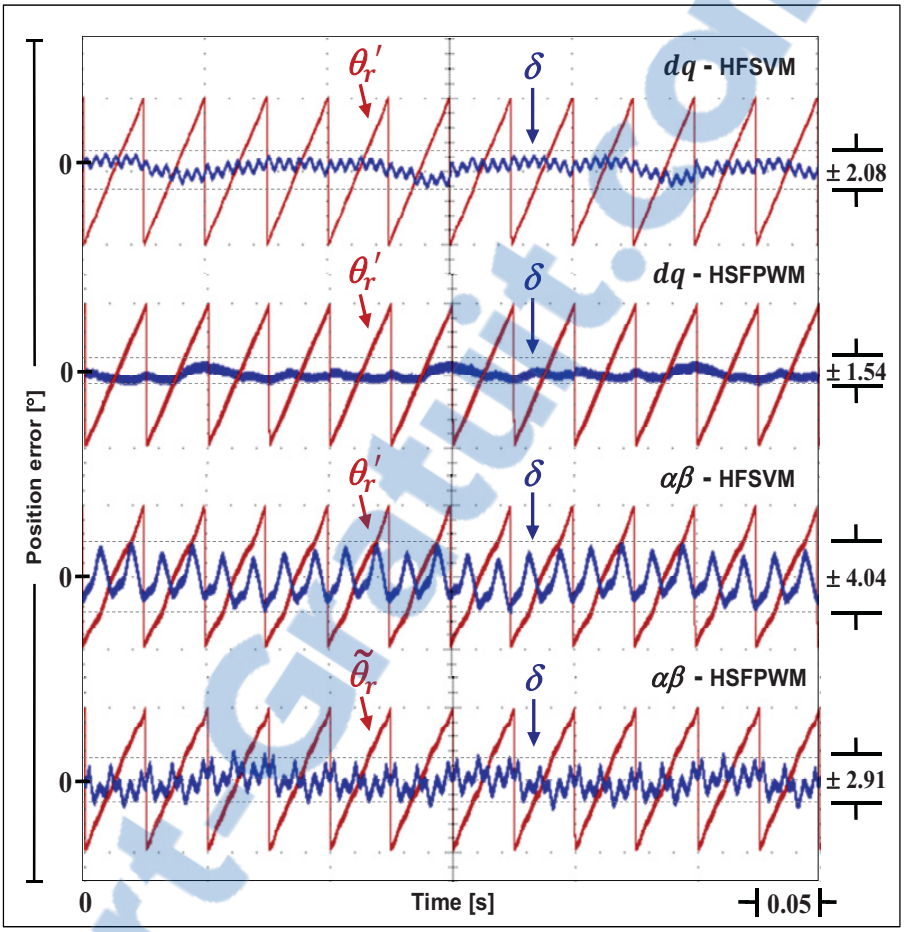

Figure 4.22 Comparison of the experimental rotor position error obtained for the four HFSI techniques. The test has been carried out under no load at $\omega_r^* = 300$ rpm

The response of the four HFSI techniques to full motoring and generating torque step-changes at 300rpm is shown in Figure 4.23. It can be observed that the proposed techniques working with an injection frequency of 2.5 kHz present a better overall performance in terms of torque ripple and rotor position error. Regarding the rotor position offset error that arises from the cross-saturation effect, it has been fairly compensated by evaluating online the function $f(I_q')$ previously built from offline q'-axis current and position error measurements (Xu and Zhu, 2016b).

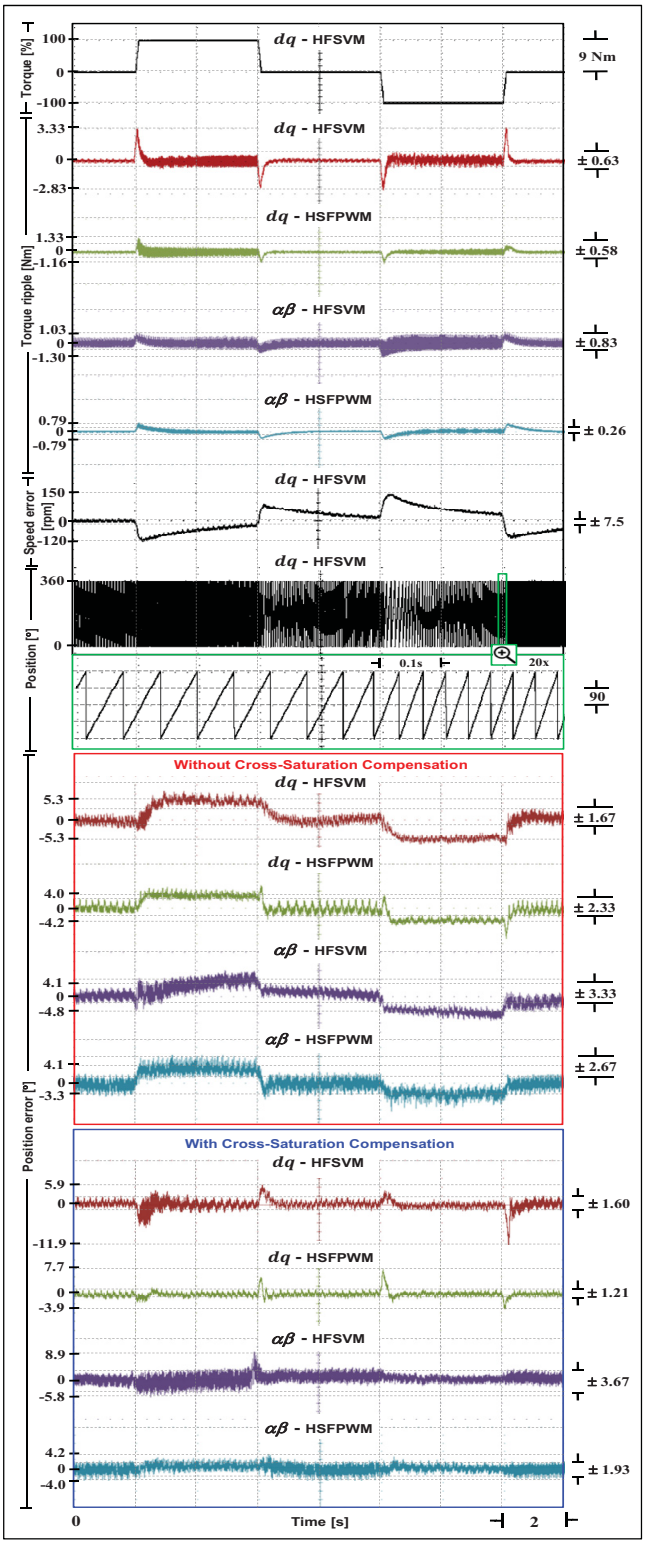

Figure 4.23 Experimental results obtained with the 2.5kW PMSM: Performance of the four HFSI techniques under 100% torque step-changes at $\omega_r^* = 300$rpm for both motoring and generating operation modes

The current control bandwidth for the four HFSI techniques is shown in Figure 4.24. It can be noted that the algorithms working in the stationary reference frame $\alpha\beta$ have the highest bandwidths with 322Hz and 385Hz while the proposed $\alpha\beta$-HSFPWM technique presents the fastest rise-time of around 900μs. The qualitative and quantitative performance comparison of the four HFSI techniques are given in Table I and Table II of the Appendix III, respectively.

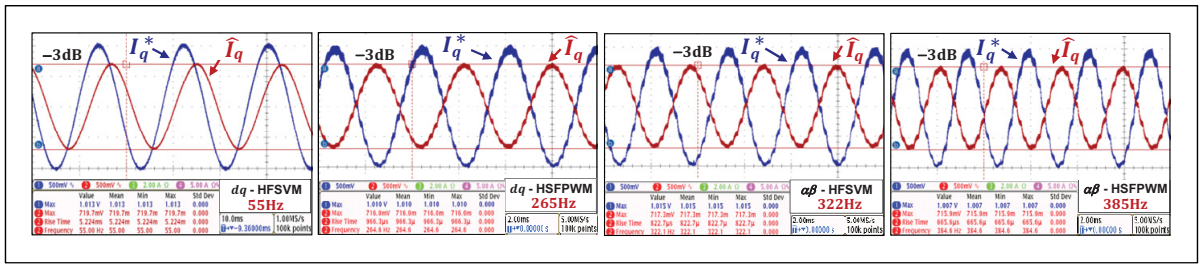

Figure 4.24 Experimental results: Reference and measured q-axis current for evaluating the closed-loop control bandwidth of the four HFSI techniques

The performance of the four HFSI techniques has been also evaluated with an 80kW-IPMSM intended for EV propulsion. The simulation results obtained during speed reversal from +300rpm to -300rpm under 100% of torque are shown in Figure 4.25. The parameters of the simulated EV IPMSM-drive are presented in Table III of the Appendix III.

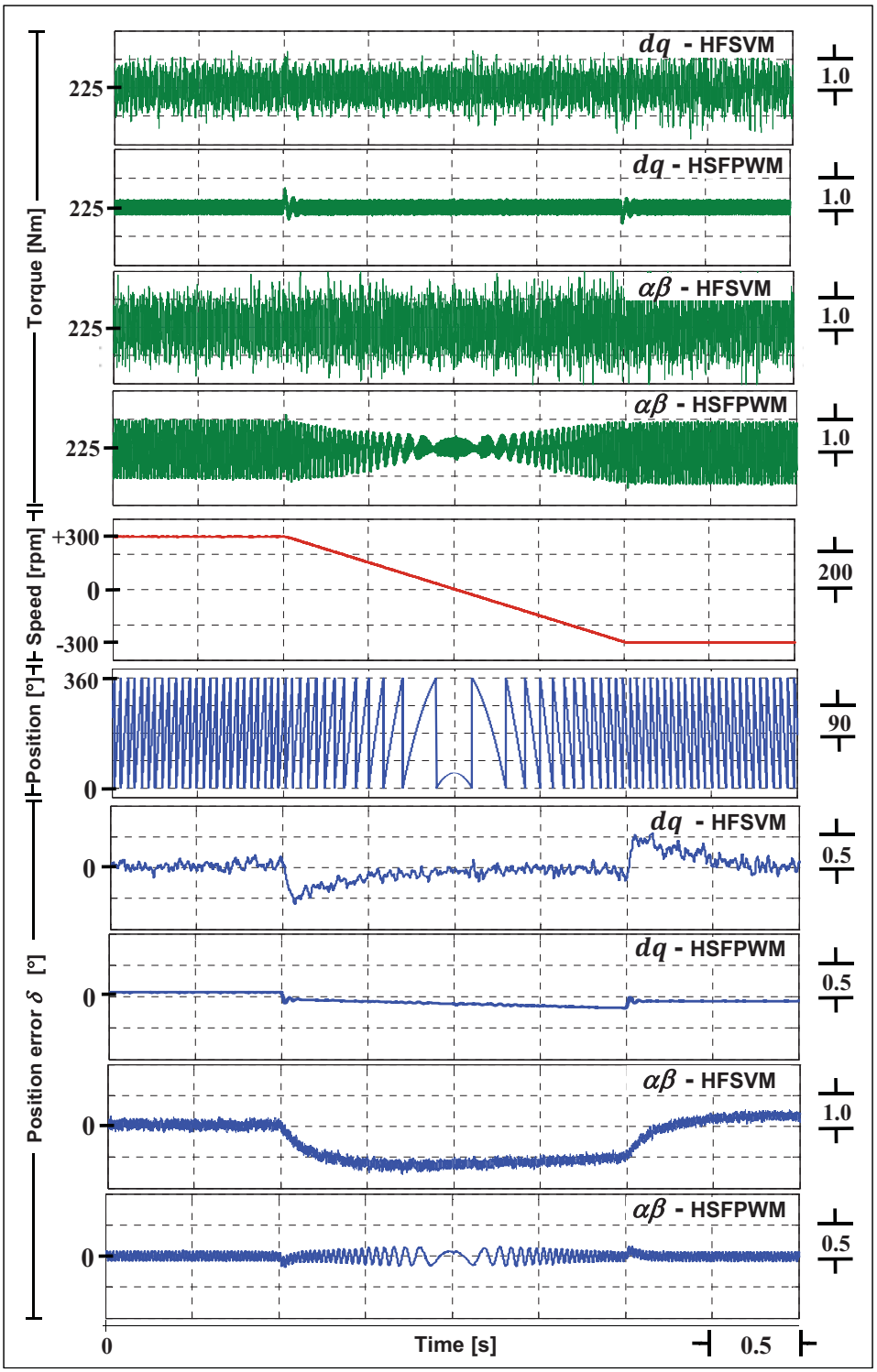

Figure 4.25 Simulation results obtained with the 80kW IPMSM: Performance of the four HFSI techniques for the speed reversal test under maximum torque

4.5 Conclusion

The performance of two novel HSFVI demodulation algorithms for encoderless FOC of PMSMs intended for EV propulsion has been investigated in this paper.

The achieved DSP-based qualitative and quantitative comparison analysis exhaustively validated through simulations and experiments with a 2.5kW PMSM has shown that the proposed PWM-based HSFSI techniques present a smaller rotor position error and a larger bandwidth than the classic SVM-based HFSI sensorless algorithms. Therefore, they allow a better machine control performance in terms of a smaller torque ripple generation and a faster current control loop.

Thanks to the very small dq-inductances value and the larger saliency ratio of the simulated 80kW IPMSM intended for EV propulsion, the dc bus voltage utilization percentage required for achieving a large high frequency stator currents SNR and thus a small rotor position estimation error does not limit the operating frequency of the proposed HSFVI algorithms. Hence, the parameters of the EV-IPMSM can allow increasing eventually the injection frequency up to 20 kHz, where the audible noise is virtually unnoticeable for human ear.

The use of the proposed pulsating and rotating HSFPWM sensorless techniques for estimating the rotor position in the low speed range and the standstill condition can thereby positively contribute to the fault-tolerant and reliability enhancement in LHDEV PMSM-traction drives.

GENERAL CONCLUSION

This thesis has presented three main contributions to the performance improvement on rotor position sensored and sensorless FOC of PMSMs intended for EV propulsion applications.

The first contribution was the development of the novel algorithm based on PA for an efficient position error compensation of MAEs. The implementation of the algorithm demonstrated its high efficiency bearing in mind that only 56 coefficients were needed to be stored in the DSP memory for a fifth-order approximation and solely 20 multiplications and 14 additions had to be executed in real-time, thus consuming less than 0.25 μs of the DSP time-step. The position error of ±0.75 electrical degrees obtained with the TM4 EV drive controlling the 80-kW PMSM successfully demonstrated that the proposed PA algorithm assisted with the type-2 PLL is a promising solution to compensate the position error of MAEs in PMSMs for EV applications.

The second contribution was the modeling and the analysis of the effects from the rotor position error in the performance of FOC-PMSM drives. The proposed model was validated by simulation and experimental results with a 400-W PMSM. The premise of the torque ripple generated due to the error from the rotor position sensor was also verified from the experimental results obtained with the 80-kW PMSM designed and manufactured by the company TM4® Electrodynamic Systems. The compensation of the error from the magnetic analog encoder mounted on the 80-kW PMSM using the PA algorithm developed in the first contribution allowed reducing the torque ripple magnitude to the range of ±1 Nm for different conditions varying from 100 Nm at 1000 r/min up to 55 Nm at 9000 r/min. Thanks to the first and second contributions, the maximum torque ripple limit condition of 5% demanded in high-performance EV PMSM-drives was successfully evaluated and fulfilled.

The third contribution was the investigation of the performance of two novel HSFVI demodulation algorithms for encoderless FOC of PMSMs. The proposed algorithms do not require voltage measurements or approximations for estimating the rotor position angle, do not need extra-hardware and work indistinctly with PMSMs having either delta- or wye- connected

windings. Therefore, they can be more easily integrated with most of the PMSM-drives currently available in industry. The achieved DSP-based qualitative and quantitative comparison analysis exhaustively validated through simulations and experiments with the 2.5-kW PMSM strongly demonstrated that the proposed PWM-based HSFSI techniques allow a better machine control performance in terms of a smaller torque ripple generation and a faster current control loop. The use of the proposed sensorless techniques for estimating the rotor position in the low speed range and the standstill condition can thereby positively contribute to the fault-tolerant and reliability enhancement in LHDEV PMSM-traction drives.

The three contributions described above constitute an important step-forward in the domain of PMSM-drives. The development of the theory and equations that support the proposed algorithms as well as the simulation and experimental results obtained at ÉTS and TM4 with the 400-W, 2.5-kW and 80-kW PMSMs are a valuable archive for future works on this subject.

FUTURE WORK

The proposed Half Switching Frequency Voltage Injection (HSFVI) demodulation algorithms described in Chapter IV were successfully tested in laboratory with the 2.5kW SMPMSM. In spite that this machine has the permanent magnets radially inset in the rotor, the fundamental direct and quadrature inductances L_d and L_q are equal whereas the differences between the high frequency direct $L_{d_{hf}}$ and quadrature $L_{q_{hf}}$ inductances at 555Hz and 2.5 kHz are only 17% and 32%, respectively. Given that the SNR of the high frequency currents containing the valuable rotor position information increases with the high frequency inductance difference ΔL_{hf} , the accuracy of the rotor position estimated with the proposed algorithms can be enhanced by using an IPMSM. Moreover, by using this kind of machine, much better results can be obtained injecting a high frequency signal with a voltage magnitude even smaller than the one used in the experiments, thus allowing to apply the proposed algorithms at much higher rotor speeds. It is important to emphasize that the smaller the difference between $L_{d_{hf}}$ and $L_{q_{hf}}$, the higher the DC bus voltage utilization percentage required for achieving a good sensorless estimation characterized by a small rotor position error. In the tests, around 35%-40% of the DC bus voltage was required for implementing the proposed HSFVI algorithms with an injection frequency of 2.5 kHz. The parameters of the 2.5kW SMPMSM used in the experiments of Chapter IV inherently restricted the upper limit of the injected frequency given that for higher frequencies, the remaining DC bus voltage was not enough to control the stator currents and counteract the increase of the BEMF with rotor speed. Therefore, the maximum operating speed of the machine under the encoderless FOC was likewise constrained. The increasing of the DC bus voltage beyond 250V was not an option given that the insulation of the stator windings could be damaged. The motivation for increasing the frequency of the injected signal not only is the enhancement of the current control bandwidth but also the reduction of the hassling audible vibration produced by the stator windings of the machine. If the injection frequency was increased to around 20 kHz, this audible nuisance would be virtually unnoticeable for human ear. The proposed HSFVI algorithms are easily adaptable for working at such high frequency. Nevertheless, in order to achieve this, an IPMSM with relatively very small dq-inductances is required. Moreover,

by using this type of salient machine, the DC bus voltage utilized for the high frequency injection would not limit neither the operating frequency of the proposed HSFVI algorithms nor the top operation speed of the machine in sensorless mode control.

The testing of the proposed techniques using an injection frequency of 20 kHz with an IPMSM having small dq-inductances and high saliency ratio would be an interesting future work. These tests can lead to improve several important aspects on PMSM-drives for EVs such as the machine control performance in terms of a smaller rotor position error, a smaller torque ripple generation, a wider operating speed range under encoderless FOC, a larger bandwidth by means of faster current control loops as well as a zero audible noise for the electric vehicle driver.

APPENDIX I

ANALYSIS AND DESIGN OF THE PLL USED IN EXPERIMENTS

The continuous transfer function $H(S)$ of the type-2 PLL is given by (Emura and Lei, 2000; Emura et al., 2000; Gardner, 2005; Harnefors and Nee, 2000; Jung and Nam, 2011)

$$\mathrm{H}(S) = \frac{\theta'(S)}{\theta(S)} = \frac{k_i + k_p \cdot S}{S^2 + k_p \cdot S + k_i} = \frac{\omega_n^2 + (2 \cdot \sigma \cdot \omega_n) \cdot S}{S^2 + (2 \cdot \sigma \cdot \omega_n) \cdot S + \omega_n^2} \tag{A I-1}$$

After applying the Euler backward transformation $S = (Z-1)/(Z \cdot T_s)$, the discrete transfer function $H(Z)$ and the set of difference equations that govern the PLL are expressed as

$$H(Z) = \frac{\theta'(Z)}{\theta(Z)} = \frac{(k_i \cdot T_s^2 + k_p \cdot T_s)Z^2 - (k_p \cdot T_s)Z}{(k_i \cdot T_s^2 + k_p \cdot T_s + 1)Z^2 - (k_p \cdot T_s + 2)Z + 1} \tag{A I-2}$$

$$\omega'(k) = \omega'(k-1) + (k_p + k_i \cdot T_s) \cdot e(k) - (k_p) \cdot e(k-1) \tag{A I-3}$$

$$e(k) = sin[\theta(k)] \cdot cos[\theta'(k)] - cos[\theta(k)] \cdot sin[\theta'(k)] \tag{A I-4}$$

$$\theta'(k) = \theta'(k-1) + T_s \cdot \omega'(k) \tag{A I-5}$$

$$k_i = \omega_n^2 \tag{A I-6}$$

$$k_p = 2 \cdot \sigma \cdot \omega_n \tag{A I-7}$$

where k represents every sample of the discrete system, T_s stands for the sampling time, θ and θ' are the real input and the estimated output rotor positions, while ω' is the estimated rotor speed.

The PLL bandwidth ω_b is obtained by solving the following fourth-order equation that results by equating $|H(j\omega_b)| = 1/\sqrt{2}$ in (A I-1)

$$\omega_b^4 - \omega_n^4 - 2\cdot\omega_b^2\cdot\omega_n^2 - 4\cdot\sigma^2\cdot\omega_b^2\cdot\omega_n^2 = 0 \quad \text{(A I-8)}$$

The useful solution from (A I-8) is given by the expression (Gardner, 2005)

$$\omega_b = \omega_n\sqrt{1 + 2\sigma^2 + \sqrt{1 + (1 + 2\sigma^2)^2}} \quad \text{(A I-9)}$$

A higher attenuation of the harmonics contained in the rotor position error can be achieved by reducing the bandwidth of the PLL but at the expense of a larger phase delay. Bearing this tradeoff in mind, the PLL bandwidth ω_b has been set at 510 rads/s. Note that for a rotor speed ω_m of 5000 r/min, $|H(2\omega_m)| \approx -7.3$ dB , whereas $|H(10\omega_m)| \approx -20.5$ dB.

In order to avoid any amplification of the rotor position error near ω_b , the transfer function of the PLL has been reduced to a first-order system by placing a pole and a zero at the same location. This design requirement is fulfilled by setting the damping factor σ = 3.5355. From (A I-9), the natural frequency ω_n is found to be 70.71 rads/s. By evaluating (A I-6) and (A I-7), the constants of the PLL loop filter result in $k_p \approx 500$ and $k_i \approx 5000$.

By substituting these values in (A I-1), the continuous transfer function results in

$$H(S) = \frac{500\cdot S + 5000}{S^2 + 500\cdot S + 5000} \quad \text{(A I-10)}$$

By considering also the sampling time T_s = 50 μs in (A I-2), the discretized transfer function of the PLL is given by

$$H_2(Z) = \frac{0.025\cdot Z^2 - 0.025\cdot Z}{1.025\cdot Z^2 - 2.025\cdot Z + 1} \quad \text{(A I-11)}$$

The linearized system of the discrete PLL used in experiments is accurately modeled by the following first-order transfer function

$$H_1(Z) = \frac{0.025 \cdot Z}{(Z - 0.975)} \qquad \text{(A I-12)}$$

The root locus of (A I-11) and (A I-12) is shown in Figure A I-1. Note that a zero and one of the poles in $H_2(Z)$ appeared overlapped. The poles of $H_2(Z)$ lying inside the unit circle also guarantee the stability of the reduced-order system $H_1(Z)$.

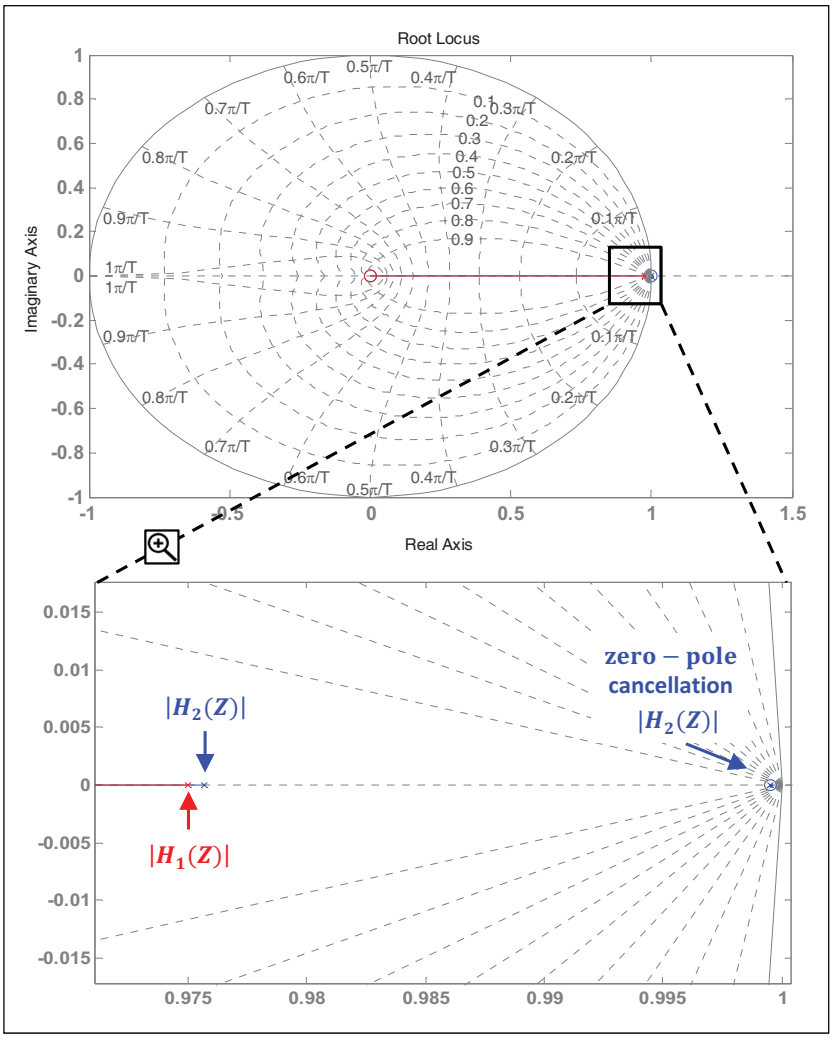

Figure-A I-1 Root locus of the linearized second- and first-order transfer functions for the PLL used in experiments

The Bode diagram of the continuous and discretized transfer functions is shown in Figure A I-2. A good frequency-response matching, the negligible amplification of $H(S)$ and $H_2(Z)$ as well as the ideal flat response of $H_1(Z)$ can be observed.

The maximum amplification gain of $H_2(Z)$ is about 0.144 dB and takes place at 4.54 Hz. The step response presents an overshoot of 1.76%.

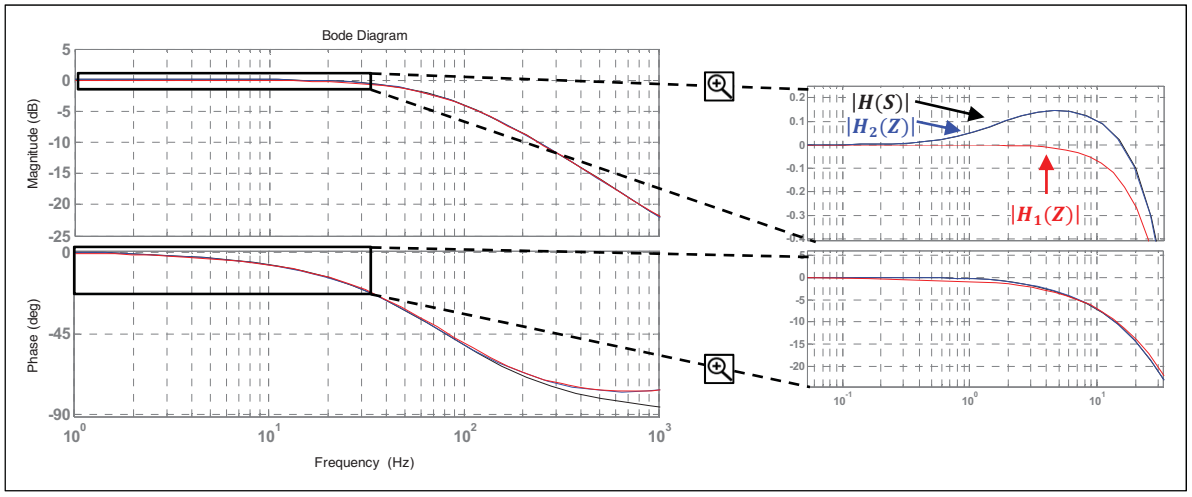

Figure-A I-2 Frequency response of the continuous and discretized transfer functions of the PLL used in experiments

APPENDIX II

BASE, CRITICAL, AND MAXIMUM SPEED IN PMSMS

The base speed ω_B is function of the intersection point between the MTPA curve and the current limit circle. In case of IPMSMs, it is derived from (3.29) evaluated at the solution of (3.25) and (3.26) given by

$$\vec{I}_d = \frac{-\vec{\lambda}_r + \sqrt{\vec{\lambda}_r^{\,2} + 8\left[\Delta L \cdot \vec{I}_{max}\right]^2}}{4\Delta L} \quad \text{and} \quad \vec{I}_q = \sqrt{\vec{I}_{max}^{\,2} - \vec{I}_d^{\,2}} \tag{A II-1}$$

The resulting equation for the based speed is as follows (Sul, 2011)

$$\omega_{B\,(IPMSM)} = \frac{\vec{V}_{max}}{\sqrt{\left(\vec{\lambda}_r + L_d \cdot \vec{I}_d\right)^2 + L_q{}^2\left(\vec{I}_{max}^{\,2} - \vec{I}_d^{\,2}\right)}} \tag{A II-2}$$

The expression for the base speed in SMPMSMs is obtained by substituting $L_d = L_q = L$ and $\vec{I}_d = 0$ in (A II-2)

$$\omega_{B\,(SMPMSM)} = \frac{\vec{V}_{max}}{\sqrt{\vec{\lambda}_r^{\,2} + \left(L \cdot \vec{I}_{max}\right)^2}} \tag{A II-3}$$

In finite-speed PMSM-drives, the theoretical maximum speed ω_M is reached when the current angle is 90°. The expression for the maximum speed in IPMSMs is found by substituting $\vec{I}_d = -\vec{I}_{max}$ in (A II-2)

$$\omega_{M\ (IPMSM)} = \frac{\vec{V}_{max}}{\vec{\lambda}_r - L_d \cdot \vec{I}_{max}} \tag{A II-4}$$

The maximum speed in SMPMSMs is deduced by substituting $L_d = L$ in (A II-4). In infinite-speed PMSM-drives, the critical speed ω_C is function of the intersection point between the MTPV curve and the current limit circle. For IPMSMs, it is deduced from (3.33) evaluated at the solution of (3.25) and (3.31) given by (A II-5), where $H = 2\Delta L\left(L_d{}^2 + L_q{}^2\right)$

$$\vec{I}_d = \frac{-\vec{\lambda}_r \cdot L_d(L_d + \Delta L) + \sqrt{\left[\vec{\lambda}_r \cdot L_d(L_d + \Delta L)\right]^2 - 2H\left[L_d \vec{\lambda}_r{}^2 - \Delta L\left(L_q \cdot \vec{I}_{max}\right)^2\right]}}{H} \tag{A II-5}$$

The resulting equation for the critical speed is (A II-6)

$$\omega_{C\ (IPMSM)} = \frac{\vec{V}_{max}\sqrt{\Delta L}}{\sqrt{2\left(L_d{}^2 \cdot \Delta L\right) \cdot \vec{I}_d{}^2 + \vec{\lambda}_r \cdot L_d(L_d + 3\Delta L) \cdot \vec{I}_d + \vec{\lambda}_r{}^2 (L_d + \Delta L)}} \tag{A II-6}$$

The expression for the critical speed in SMPMSMs is found by substituting $L_d = L_q = L$ and $\vec{I}_d = -\vec{\lambda}_r / L$ in (A II-2) (Sul, 2011)

$$\omega_{C\ (SMPMSM)} = \frac{\vec{V}_{max}}{\sqrt{\left(L \cdot \vec{I}_{max}\right)^2 - \vec{\lambda}_r{}^2}} \tag{A II-7}$$

Table-A II-1 Parameters of the PMSMs

Parameter	Symbol	SMPMSM	IPMSM	Units
Rotor Flux	λ_r	0.046	0.040	V·s
Phase Resistance	R_s	1.0	0.041	Ω
Phase dq Inductances	L_d , L_q	4.0/4.0	0.184/0.300	mH
Cont. and Peak Torque	τ_c , τ_{pk}	1.4/2.5	120/225	N·m
Cont.* and Max Power	P_c , P_M	0.28/0.44	37/80	kW
Base, Rated and Max Speed	ω_B , ω_R , ω_M	1.4/2.15/4	2.93/9.65/12	Kr/min
Cont. and Peak Current	I_c , I_{pk}	5/9	317/500	A
Number of pole pairs	P	4	5	-

* Continuous power measured at rated speed

APPENDIX III

QUALITATIVE AND QUANTITATIVE PERFORMANCE COMPARISON OF THE FOUR HFSI TECHNIQUES

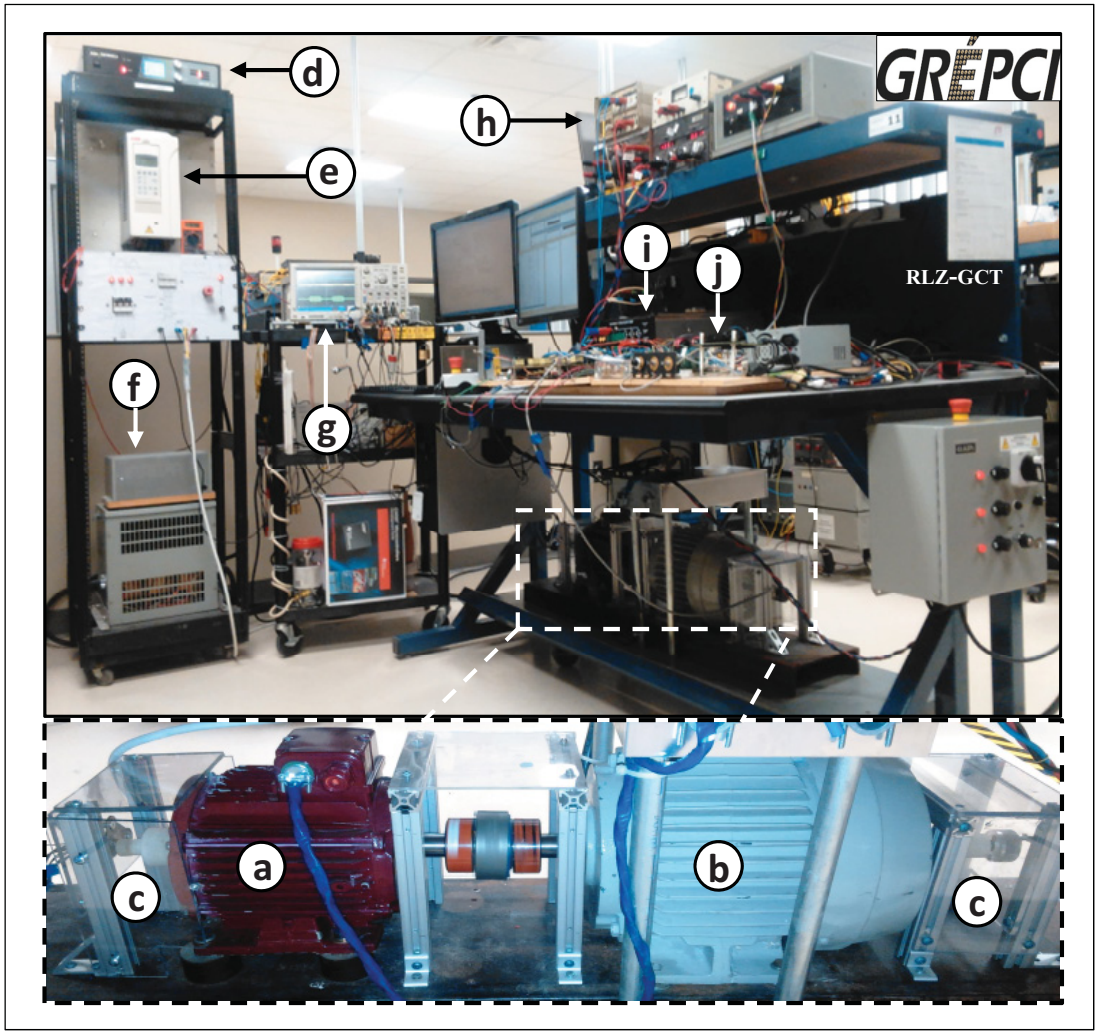

Figure-A III-1 Experimental setup used for the sensorless tests: (a) 2.5-kW PMSM (b) Induction Machine (c) Encoders (d) 4kW Bi-directional DC source (e) IM-drive (f) Braking resistors (g) Scope (h) DC voltage sources i) 2L-Inverter for PMSM-drive (j) TI® DSP-based control board

Table-A III-1 Qualitative performance comparison of the four HFSI techniques

Feature	HFSI TECHNIQUE			
	dq-HFSVM	dq-HSFPWM	$\alpha\beta$-HFSVM	$\alpha\beta$-HSFPWM
DC voltage utilization	Low (√)	Medium	Medium	High
Ratio of HF current to rated fundamental current	Medium	Low	High	Low (√)
DSP implementation complexity	Low (√)	Medium	Medium	High
PI controller requirement for position estimation	YES	YES	YES	NO (√)
DSP execution-time	Low	Low (√)	Medium	High
Current control bandwidth	Low	Medium	Medium	High (√)
Rotor position error	Low	Low (√)	High	Medium
Torque ripple	Medium	Medium	High	Low (√)
Sensitivity to machine parameters	Low	Medium	Low (√)	Medium
Overall performance of encoderless FOC-PMSM	Medium	High	Low	High (√)

√ Check mark means the best performance

Table-A III-2 Quantitative performance comparison of the four HFSI techniques

Parameter	Units	HFSI TECHNIQUE							
		SMPMSM-drive				IPMSM-drive			
Modulation	-	SVM	PWM	SVM	PWM	SVM	PWM	SVM	PWM
Frame	-	dq	dq	$\alpha\beta$	$\alpha\beta$	dq	dq	$\alpha\beta$	$\alpha\beta$
V_{inj}	V	21.6	43.8	43.3	50.0	1.0	5.0	1.0	5.0
f_{inj}	Hz	555	2.5K	555	2.5K	588	10K	588	10K
$\lvert\rho\rvert$	°	11.9	7.7	8.9	4.2	0.71	0.78	1.58	0.16
δ	°	±1.6	±1.2	±3.7	±1.9	±0.21	±0.02	±0.26	±0.16
I_{hf}	A	0.34	0.14	0.68	0.13	1.49	0.68	1.49	0.68
τ_{ripple}	%	±7.0	±6.4	±9.2	±2.9	±0.67	±0.27	±0.89	±0.50
I_{BW}	Hz	55	265	322	385	>84	>84	>84	>84
Base Speed	rpm	1020	680	750	440	2920	2440	2920	2440

- SMPMSM - drive : Tests at 300rpm under ±9 Nm
- IPMSM - drive : Tests at ±300rpm under 225 Nm

Table-A III-3 PMSM-drives parameters

Parameter	Symbol	Value		Units
		SMPMSM	IPMSM	
Rotor Flux	λ_r	0.3	0.040	V·s
Phase Resistance	R_s	1.5	0.041	Ω
Phase dq Inductances	L_d , L_q	14/14	0.184/0.300	mH
Cont. and Peak Torque	τ_c , τ_{pk}	5.4/9	120/225	N·m
Cont. and Max Power	P_c , P_M	1.5/2.5	37/80	KW
Base Speed (SVM/PWM) *	ω_B	1050/870	2930/2480	rpm
Cont. and Peak Current	I_c , I_{pk}	3/5	317/500	A
Number of pole pairs	P	4	5	-
DC bus voltage	V_{DC}	250	350	V
Switching frequency	f_{sw}	5	20	KHz
Current sampling frequency	I_{sf}	5	20	KHz

* Measured when no HF voltage is injected

APPENDIX IV

DETAILED PROCEDURE FOR THE DERIVATION OF SOME IMPORTANT EQUATIONS INCLUDED IN THE TRANSACTIONS PAPERS

In order to find the expression for the PLL bandwidth, the transfer function $H(S)$ is evaluated at the cut-off frequency $S = j\omega_b$, where the attenuation of the input signal is -3dB. The detailed procedure for deriving eq. (A I-8) is as follows :

$$\mathrm{H}(S) = \frac{\omega_n^{\,2} + (2 \cdot \sigma \cdot \omega_n) \cdot S}{S^2 + (2 \cdot \sigma \cdot \omega_n) \cdot S + \omega_n^{\,2}} \tag{A IV-1}$$

$$|H(j\omega_b)| = 1/\sqrt{2} \tag{A IV-2}$$

$$\left| \frac{\omega_n^{\,2} + (2 \cdot \sigma \cdot \omega_n) \cdot (j\omega_b)}{(j\omega_b)^2 + (2 \cdot \sigma \cdot \omega_n) \cdot (j\omega_b) + \omega_n^{\,2}} \right| = 1/\sqrt{2} \tag{A IV-3}$$

By calculating the magnitude of the complex numbers in (A IV-3), it is rewritten as :

$$\frac{\sqrt[2]{(\omega_n^{\,2})^2 + (2 \cdot \sigma \cdot \omega_n \cdot \omega_b)^2}}{\sqrt[2]{(\omega_n^{\,2} - \omega_b^{\,2})^2 + (2 \cdot \sigma \cdot \omega_n \cdot \omega_b)^2}} = 1/\sqrt{2} \tag{A IV-4}$$

$$\frac{\omega_n^{\,4} + 4 \cdot \sigma^2 \cdot \omega_n^{\,2} \cdot \omega_b^{\,2}}{\omega_n^{\,4} + \omega_b^{\,4} - 2 \cdot \omega_n^{\,2} \cdot \omega_b^{\,2} + 4 \cdot \sigma^2 \cdot \omega_n^{\,2} \cdot \omega_b^{\,2}} = 1/2 \tag{A IV-5}$$

$$2 \cdot \omega_n^{\,4} + 8 \cdot \sigma^2 \cdot \omega_n^{\,2} \cdot \omega_b^{\,2} = \omega_n^{\,4} + \omega_b^{\,4} - 2 \cdot \omega_n^{\,2} \cdot \omega_b^{\,2} + 4 \cdot \sigma^2 \cdot \omega_n^{\,2} \cdot \omega_b^{\,2} \tag{A IV-6}$$

$$(\omega_n^{\,4} - \omega_b^{\,4} + 4 \cdot \sigma^2 \cdot \omega_n^2 \cdot \omega_b^{\,2} + 2 \cdot \omega_n^{\,2} \cdot \omega_b^{\,2} = 0)(-1) \tag{A IV-7}$$

The final expression is given by (Gardner, 2005) :

$$\omega_b^{\,4} - \omega_n^{\,4} - 2 \cdot \omega_b^2 \cdot \omega_n^2 - 4 \cdot \sigma^2 \cdot \omega_b^2 \cdot \omega_n^{\,2} = 0 \tag{A IV-8}$$

The detailed procedure for deriving eq. (4.11) is presented below. According to the demodulation procedure of Fig. 4.2, the HF q'-axis current from (A IV-9) is first multiplied by the high frequency sinusoidal signal $sin(\omega_{hf} t)$:

$$I'_{q_{hf}} = \frac{V_{inj}\, sin(\omega_{hf} t\,)}{L_{d_{hf}} L_{q_{hf}} \omega_{hf}} \left[-\Delta L_{hf}\, sin(2\delta) \right] \qquad \text{(A IV - 9)}$$

$$I'_{q_{hf}} \cdot\, sin\big(\omega_{hf} t\,\big) = \left[\frac{-\Delta L_{hf} V_{inj}}{L_{d_{hf}} L_{q_{hf}} \omega_{hf}} \right] \left[sin^2(\omega_{hf} t)\, sin(2\delta) \right] \qquad \text{(A IV - 10)}$$

By applying the trigonometric identity from (A IV - 11) to (A IV - 10) :

$$sin^2\big(\omega_{hf} t\big) = \frac{1 - cos(2\omega_{hf} t\,)}{2} \qquad \text{(A IV - 11)}$$

the following expression is obtained :

$$I'_{q_{hf}} \cdot\, sin\big(\omega_{hf} t\,\big) = \left[\frac{-\Delta L_{hf} V_{inj}}{2 L_{d_{hf}} L_{q_{hf}} \omega_{hf}} \right] \left[sin(2\delta\,) - \, cos(2\omega_{hf} t\,)\, sin(2\delta\,) \right] \qquad \text{(A IV - 12)}$$

The rotor position error function $f(\delta)$ obtained after applying the low-pass filter (*LPF*) to (A IV - 12) is expressed as :

$$f(\delta) = LPF \left[I'_{q_{hf}} \cdot\, sin\big(\omega_{hf} t\,\big) \right] \qquad \text{(A IV - 13)}$$

Due to the *LPF*, the second term from (A IV - 12) containing the high frequency component is fairly attenuated. By keeping just the first term containing the low frequency component in (A IV - 12), the error function is written as follows :

$$f(\delta) = \left[\frac{-\Delta L_{hf} V_{inj}}{2 L_{d_{hf}} L_{q_{hf}} \omega_{hf}} \right] sin(2\delta\,) \qquad \text{(A IV - 14)}$$

By assuming that the the rotor position error δ is small, the evaluation of the trigonometric function can be replaced with its argument, i.e., $2\delta \approx 0 \rightarrow \sin(2\delta) \approx 2\delta$. The simplified expression for the rotor position error function $f(\delta)$ is finally given by :

$$f(\delta) \approx \left[\frac{-\Delta L_{hf} V_{inj}}{L_{d_{hf}} L_{q_{hf}} \omega_{hf}} \right] \delta \qquad \text{(A IV - 15)}$$

The detailed procedure for deriving eq. (4.19) is presented below. According to the demodulation procedure of Fig. 4.8, the HF α - axis current from (A IV - 16) is first multiplied by the term (A IV - 18) whereas the HF β - axis current from (A IV - 17) is multiplied by the term (A IV - 19) :

$$I_{\alpha_{hf}} = \frac{V_{inj}}{L_{d_{hf}} L_{q_{hf}} \omega_{hf}} \left[\Sigma L_{hf} \sin(\omega_{hf} t) - \Delta L_{hf} \sin\left(\omega_{hf} t - 2\theta_r\right) \right] \quad \text{(A IV - 16)}$$

$$I_{\beta_{hf}} = \frac{V_{inj}}{L_{d_{hf}} L_{q_{hf}} \omega_{hf}} \left[-\Sigma L_{hf} \cos(\omega_{hf} t) - \Delta L_{hf} \cos\left(\omega_{hf} t - 2\theta_r\right) \right] \quad \text{(A IV - 17)}$$

$$I_{\alpha_{hf}}{}' = \cos\left(\omega_{hf} t - 2\theta_r{}'\right) \quad \text{(A IV - 18)}$$

$$I_{\beta_{hf}}{}' = \sin\left(\omega_{hf} t - 2\theta_r{}'\right) \quad \text{(A IV - 19)}$$

The error e is calculated as follows :

$$e = I_{\alpha_{hf}} \cdot I_{\alpha_{hf}}{}' - I_{\beta_{hf}} \cdot I_{\beta_{hf}}{}' \quad \text{(A IV - 20)}$$

By substituting (A IV - 16) - (A IV - 19) into (A IV – 20), the error is e given by :

$$e = \frac{V_{inj}}{L_{d_{hf}} L_{q_{hf}} \omega_{hf}} \left\{ \left[\Sigma L_{hf} \sin(\omega_{hf} t) - \Delta L_{hf} \sin\left(\omega_{hf} t - 2\theta_r\right) \right] \cdot \cos\left(\omega_{hf} t - 2\theta_r{}'\right) + \left[\Sigma L_{hf} \cos(\omega_{hf} t) + \Delta L_{hf} \cos\left(\omega_{hf} t - 2\theta_r\right) \right] \cdot \sin\left(\omega_{hf} t - 2\theta_r{}'\right) \right\} \quad \text{(A IV - 21)}$$

By expanding (A IV - 21), the error e is expressed as :

$$e = \frac{V_{inj}}{L_{d_{hf}} L_{q_{hf}} \omega_{hf}} \left\{ \begin{array}{l} \Sigma L_{hf} \sin(\omega_{hf} t) \cdot \cos\left(\omega_{hf} t - 2\theta_r{}'\right) \\ - \Delta L_{hf} \sin\left(\omega_{hf} t - 2\theta_r\right) \cdot \cos\left(\omega_{hf} t - 2\theta_r{}'\right) \\ + \Sigma L_{hf} \cos(\omega_{hf} t) \cdot \sin\left(\omega_{hf} t - 2\theta_r{}'\right) \\ + \Delta L_{hf} \cos\left(\omega_{hf} t - 2\theta_r\right) \cdot \sin\left(\omega_{hf} t - 2\theta_r{}'\right) \end{array} \right\} \quad \text{(A IV - 22)}$$

By applying the trigonometric identity from (A IV - 23) to (A IV - 22) :

$$\sin(\alpha) \cdot \cos(\beta) \pm \cos(\alpha) \cdot \sin(\beta) = \sin(\alpha \pm \beta) \quad \text{(A IV - 23)}$$

the error e is simplified as :

$$e = \frac{V_{inj}}{L_{d_{hf}} L_{q_{hf}} \omega_{hf}} \left\{ \Sigma L_{hf} \cdot sin\left[2(\omega_{hf} t - \theta_r')\right] + \Delta L_{hf} \cdot sin[2(\theta_r - \theta_r')] \right\} \quad \text{(A IV - 24)}$$

By substituting $\theta_r - \theta_r' = \delta$ in (A IV - 24), it is rewritten as :

$$e = \frac{V_{inj}}{L_{d_{hf}} L_{q_{hf}} \omega_{hf}} \left\{ \Sigma L_{hf} \cdot sin\left[2(\omega_{hf} t - \theta_r')\right] + \Delta L_{hf} \cdot \sin(2\delta) \right\} \quad \text{(A IV - 25)}$$

After low-pass filtering the error e from (A IV - 25), the first term containing the high frequency component is fairly attenuated. By keeping just the second term containing the low frequency component in (A IV - 25), the rotor position error function $f(\delta)$ is written as follows :

$$f(\delta) = LPF(e) = \frac{V_{inj}}{L_{d_{hf}} L_{q_{hf}} \omega_{hf}} \cdot \Delta L_{hf} \cdot \sin(2\delta) \quad \text{(A IV - 26)}$$

By assuming that the the rotor position error δ is small, the evaluation of the trigonometric function can be replaced with its argument, i.e., $2\delta \approx 0 \rightarrow \sin(2\delta) \approx 2\delta$. The simplified expression for the rotor position error function $f(\delta)$ is finally given by :

$$f(\delta) \approx \left[\frac{2\Delta L_{hf} V_{inj}}{L_{d_{hf}} L_{q_{hf}} \omega_{hf}} \right] \delta \quad \text{(A IV - 27)}$$

BIBLIOGRAPHY

Aksenenko, V. D. and S. I. Matveyev. 2005. "Digital Angle Sensor Self-Calibration: Two Approaches to Accuracy Increasing". In *2005 IEEE Instrumentationand Measurement Technology Conference Proceedings*. (16-19 May 2005) Vol. 1, p. 543-547.

Al-nabi, E., B. Wu, N. R. Zargari, and V. Sood. 2013. "Sensorless Control of CSC-Fed IPM Machine for Zero- and Low-Speed Operations Using Pulsating HFI Method". *IEEE Transactions on Industrial Electronics,* vol. 60, n^{o} 5, p. 1711-1723.

Ancuti, R., I. Boldea, and G. D. Andreescu. 2010. "Sensorless V/f control of high-speed surface permanent magnet synchronous motor drives with two novel stabilising loops for fast dynamics and robustness". *IET Electric Power Applications,* vol. 4, n^{o} 3, p. 149-157.

Bergas-Jan, J., C. Ferrater-Sim, G. Gross, R. Ramirez-Pisco, S. Galceran-Arellano, and J. Rull-Duran. 2012. "High-Accuracy All-Digital Resolver-to-Digital Conversion". *IEEE Transactions on Industrial Electronics,* vol. 59, n^{o} 1, p. 326-333.

Bolognani, S., S. Calligaro, and R. Petrella. 2014. "Adaptive Flux-Weakening Controller for Interior Permanent Magnet Synchronous Motor Drives". *IEEE Journal of Emerging and Selected Topics in Power Electronics,* vol. 2, n^{o} 2, p. 236-248.

Bon-Ho, Bae, N. Patel, S. Schulz, and Sul Seung-Ki. 2003. "New field weakening technique for high saliency interior permanent magnet motor". In *Industry Applications Conference, 2003. 38th IAS Annual Meeting. Conference Record of the*. (12-16 Oct. 2003) Vol. 2, p. 898-905 vol.2.

Briz, F. and M. W. Degner. 2011. "Rotor Position Estimation". *IEEE Industrial Electronics Magazine,* vol. 5, n^{o} 2, p. 24-36.

Bunte, A. and S. Beineke. 2004. "High-performance speed measurement by suppression of systematic resolver and encoder errors". *IEEE Transactions on Industrial Electronics,* vol. 51, n^{o} 1, p. 49-53.

Chai, S., L. Wang, and E. Rogers. 2013. "A Cascade MPC Control Structure for a PMSM With Speed Ripple Minimization". *IEEE Transactions on Industrial Electronics,* vol. 60, n^{o} 8, p. 2978-2987.

Chen, X., M. Edington, R. Thornton, Fang Yunzhou, and Peng Qingfeng. 2007. "Development issues of an ISG PM machine and control system". In *2007 7th Internatonal Conference on Power Electronics*. (22-26 Oct. 2007), p. 922-929.

Cho, Y., K. B. Lee, J. H. Song, and Y. I. Lee. 2015. "Torque-Ripple Minimization and Fast Dynamic Scheme for Torque Predictive Control of Permanent-Magnet Synchronous Motors". *IEEE Transactions on Power Electronics,* vol. 30, n° 4, p. 2182-2190.

Choi, C., K. Lee, and W. Lee. 2015. "Observer-Based Phase-Shift Fault Detection Using Adaptive Threshold for Rotor Position Sensor of Permanent-Magnet Synchronous Machine Drives in Electromechanical Brake". *IEEE Transactions on Industrial Electronics,* vol. 62, n° 3, p. 1964-1974.

Consoli, A., G. Scelba, G. Scarcella, and M. Cacciato. 2013. "An Effective Energy-Saving Scalar Control for Industrial IPMSM Drives". *IEEE Transactions on Industrial Electronics,* vol. 60, n° 9, p. 3658-3669.

Emura, T. and Wang Lei. 2000. "A high-resolution interpolator for incremental encoders based on the quadrature PLL method". *IEEE Transactions on Industrial Electronics,* vol. 47, n° 1, p. 84-90.

Emura, T., Wang Lei, M. Yamanaka, and H. Nakamura. 2000. "A high-precision positioning servo controller based on phase/frequency detecting technique of two-phase-type PLL". *IEEE Transactions on Industrial Electronics,* vol. 47, n° 6, p. 1298-1306.

EV-volumes. 2017. " Global Plug-in Sales for 2016 ". Online: http://www.ev-volumes.com/. Accessed: 06 March 2017.

evHUB. 2011. " Why EVs? ". Online: http://evworld.com.sg/WhyEV.htm. Accessed: 20 November 2016.

Faber, J. 2012. "Self-calibration and noise reduction of resolver sensor in servo drive application". In *ELEKTRO, 2012*. (21-22 May 2012), p. 174-178.

Flieller, D., N. K. Nguyen, P. Wira, G. Sturtzer, D. O. Abdeslam, and J. Merckle. 2014. "A Self-Learning Solution for Torque Ripple Reduction for Nonsinusoidal Permanent-Magnet Motor Drives Based on Artificial Neural Networks". *IEEE Transactions on Industrial Electronics,* vol. 61, n° 2, p. 655-666.

Foo, G. and M. F. Rahman. 2010. "Sensorless Sliding-Mode MTPA Control of an IPM Synchronous Motor Drive Using a Sliding-Mode Observer and HF Signal Injection". *IEEE Transactions on Industrial Electronics,* vol. 57, n° 4, p. 1270-1278.

Gabriel, F., F. De Belie, X. Neyt, and P. Lataire. 2013. "High-Frequency Issues Using Rotating Voltage Injections Intended For Position Self-Sensing". *IEEE Transactions on Industrial Electronics,* vol. 60, n° 12, p. 5447-5457.

Gallegos-Lopez, G., F. S. Gunawan, and J. E. Walters. 2005. "Optimum torque control of permanent-magnet AC Machines in the field-weakened region". *IEEE Transactions on Industry Applications,* vol. 41, n° 4, p. 1020-1028.

Gao, Q., G. M. Asher, M. Sumner, and L. Empringham. 2009. "Position Estimation of a Matrix-Converter-Fed AC PM Machine From Zero to High Speed Using PWM Excitation". *IEEE Transactions on Industrial Electronics,* vol. 56, n° 6, p. 2030-2038.

Gardner, F. M. 2005. *Phaselock Techniques*. Hoboken, NJ, USA: Wiley.

Gebregergis, A., M. H. Chowdhury, M. S. Islam, and T. Sebastian. 2015. "Modeling of Permanent-Magnet Synchronous Machine Including Torque Ripple Effects". *IEEE Transactions on Industry Applications,* vol. 51, n° 1, p. 232-239.

Ha, J. I. 2008. "Analysis of Inherent Magnetic Position Sensors in Symmetric AC Machines for Zero or Low Speed Sensorless Drives". *IEEE Transactions on Magnetics,* vol. 44, n° 12, p. 4689-4696.

Hagiwara, N., Y. Suzuki, and H. Murase. 1992. "A method of improving the resolution and accuracy of rotary encoders using a code compensation technique". *IEEE Transactions on Instrumentation and Measurement,* vol. 41, n° 1, p. 98-101.

Hanselman, D. C. 1990. "Resolver signal requirements for high accuracy resolver-to-digital conversion". *IEEE Transactions on Industrial Electronics,* vol. 37, n° 6, p. 556-561.

Hanselman, D. C. 1991. "Techniques for improving resolver-to-digital conversion accuracy". *IEEE Transactions on Industrial Electronics,* vol. 38, n° 6, p. 501-504.

Hao, L., S. Gopalakrishnan, C. Namuduri, and K. Rahman. 2013. "Impact of position sensor accuracy on the performance of IPM drives". In *2013 IEEE Energy Conversion Congress and Exposition*. (15-19 Sept. 2013), p. 196-201.

Harnefors, L. and H. P. Nee. 2000. "A general algorithm for speed and position estimation of AC motors". *IEEE Transactions on Industrial Electronics,* vol. 47, n° 1, p. 77-83.

Hoang, H. V. and J. W. Jeon. 2011. "An Efficient Approach to Correct the Signals and Generate High-Resolution Quadrature Pulses for Magnetic Encoders". *IEEE Transactions on Industrial Electronics,* vol. 58, n° 8, p. 3634-3646.

Hoang, K. D., J. Wang, M. Cyriacks, A. Melkonyan, and K. Kriegel. 2013. "Feed-forward torque control of interior permanent magnet brushless AC drive for traction applications". In *Electric Machines & Drives Conference (IEMDC), 2013 IEEE International*. (12-15 May 2013), p. 152-159.

Holtz, J. 2008. "Acquisition of Position Error and Magnet Polarity for Sensorless Control of PM Synchronous Machines". *IEEE Transactions on Industry Applications,* vol. 44, n° 4, p. 1172-1180.

Hoseinnezhad, R. 2006. "Position sensing in brake-by-wire callipers using resolvers". *IEEE Transactions on Vehicular Technology,* vol. 55, n° 3, p. 924-932.

Hoseinnezhad, R., A. Bab-Hadiashar, and P. Harding. 2007. "Calibration of Resolver Sensors in Electromechanical Braking Systems: A Modified Recursive Weighted Least-Squares Approach". *IEEE Transactions on Industrial Electronics,* vol. 54, n° 2, p. 1052-1060.

Hu, J., J. Zou, F. Xu, Y. Li, and Y. Fu. 2012. "An Improved PMSM Rotor Position Sensor Based on Linear Hall Sensors". *IEEE Transactions on Magnetics,* vol. 48, n° 11, p. 3591-3594.

Hwang, S. H., H. J. Kim, J. M. Kim, L. Liu, and H. Li. 2011. "Compensation of Amplitude Imbalance and Imperfect Quadrature in Resolver Signals for PMSM Drives". *IEEE Transactions on Industry Applications,* vol. 47, n° 1, p. 134-143.

Hwang, S. H., J. H. Lee, J. M. Kim, and C. Choi. 2010. "Compensation of analog rotor position errors due to nonideal sinusoidal encoder output signals". In *2010 IEEE Energy Conversion Congress and Exposition*. (12-16 Sept. 2010), p. 4469-4473.

Jansen, P. L. and R. D. Lorenz. 1995. "Transducerless position and velocity estimation in induction and salient AC machines". *IEEE Transactions on Industry Applications,* vol. 31, n° 2, p. 240-247.

Ji-Hoon, Jang, Ha Jung-Ik, M. Ohto, K. Ide, and Sul Seung-Ki. 2004. "Analysis of permanent-magnet machine for sensorless control based on high-frequency signal injection". *IEEE Transactions on Industry Applications,* vol. 40, n° 6, p. 1595-1604.

Ji-Hoon, Jang, Sul Seung-Ki, Ha Jung-Ik, K. Ide, and M. Sawamura. 2003. "Sensorless drive of surface-mounted permanent-magnet motor by high-frequency signal injection based on magnetic saliency". *IEEE Transactions on Industry Applications,* vol. 39, n° 4, p. 1031-1039.

Ju-Chan, Kim, Kim Jang-Mok, U. Kim Cheul, and Choi Cheol. 2006. "Ultra precise position estimation of servomotor using analog quadrature encoders". In *Twenty-First Annual IEEE Applied Power Electronics Conference and Exposition, 2006. APEC '06.* (19-23 March 2006), p. 5 pp.

Jung, S. and J. I. Ha. 2015. "Analog Filtering Method for Sensorless AC Machine Control With Carrier-Frequency Signal Injection". *IEEE Transactions on Industrial Electronics,* vol. 62, n° 9, p. 5348-5358.

Jung, S. Y., J. Hong, and K. Nam. 2013. "Current Minimizing Torque Control of the IPMSM Using Ferrari's Method". *IEEE Transactions on Power Electronics,* vol. 28, n° 12, p. 5603-5617.

Jung, S. Y., C. C. Mi, and K. Nam. 2015. "Torque Control of IPMSM in the Field-Weakening Region With Improved DC-Link Voltage Utilization". *IEEE Transactions on Industrial Electronics,* vol. 62, n° 6, p. 3380-3387.

Jung, S. Y. and K. Nam. 2011. "PMSM Control Based on Edge-Field Hall Sensor Signals Through ANF-PLL Processing". *IEEE Transactions on Industrial Electronics,* vol. 58, n° 11, p. 5121-5129.

Kano, Y., T. Kosaka, and N. Matsui. 2013. "Design of signal-injection-based sensorless interior permanent magnet synchronous motor drives for HEV". In *2013 IEEE International Symposium on Sensorless Control for Electrical Drives and Predictive Control of Electrical Drives and Power Electronics (SLED/PRECEDE)*. (17-19 Oct. 2013), p. 1-7.

Kano, Y., T. Kosaka, N. Matsui, T. Takahashi, and M. Fujitsuna. 2012. "Signal-injection-based sensorless IPM traction drive for wide-torque range operation at low speed". In *2012 IEEE Energy Conversion Congress and Exposition (ECCE)*. (15-20 Sept. 2012), p. 2284-2291.

Kavanagh, R. C. 2001. "Probabilistic learning technique for improved accuracy of sinusoidal encoders". *IEEE Transactions on Industrial Electronics,* vol. 48, n° 3, p. 673-681.

Kim, S., J. I. Ha, and S. K. Sul. 2011a. "PWM switching frequency signal injection sensorless method in IPMSM". In *2011 IEEE Energy Conversion Congress and Exposition*. (17-22 Sept. 2011), p. 3021-3028.

Kim, S., J. I. Ha, and S. K. Sul. 2012. "PWM Switching Frequency Signal Injection Sensorless Method in IPMSM". *IEEE Transactions on Industry Applications,* vol. 48, n° 5, p. 1576-1587.

Kim, S. I., J. H. Im, E. Y. Song, and R. Y. Kim. 2016. "A New Rotor Position Estimation Method of IPMSM Using All-Pass Filter on High-Frequency Rotating Voltage Signal Injection". *IEEE Transactions on Industrial Electronics,* vol. 63, n° 10, p. 6499-6509.

Kim, S., Y. C. Kwon, S. K. Sul, J. Park, and S. M. Kim. 2011b. "Position sensorless operation of IPMSM with near PWM switching frequency signal injection". In *Power Electronics and ECCE Asia (ICPE & ECCE), 2011 IEEE 8th International Conference on*. (May 30 2011-June 3 2011), p. 1660-1665.

Kim, S. and S. K. Sul. 2011. "High performance position sensorless control using rotating voltage signal injection in IPMSM". In *Power Electronics and Applications (EPE*

2011), Proceedings of the 2011-14th European Conference on. (Aug. 30 2011-Sept. 1 2011), p. 1-10.

Kok Kiong, Tan and Tang Kok-Zuea. 2005. "Adaptive online correction and interpolation of quadrature encoder signals using radial basis functions". *IEEE Transactions on Control Systems Technology,* vol. 13, n° 3, p. 370-377.

Lara, J. and A. Chandra. 2014a. "Performance study of switching frequency signal injection algorithm in PMSMs for EV propulsion: A comparison in stator and rotor coordinates". In *2014 IEEE 23rd International Symposium on Industrial Electronics (ISIE)*. (1-4 June 2014), p. 865-870.

Lara, J. and A. Chandra. 2014b. "Position error compensation in quadrature analog magnetic encoders through an iterative optimization algorithm". In *IECON 2014 - 40th Annual Conference of the IEEE Industrial Electronics Society*. (Oct. 29 2014-Nov. 1 2014), p. 3043-3048.

Lara, J., A. Chandra, and J. Xu. 2012. "Integration of HFSI and extended-EMF based techniques for PMSM sensorless control in HEV/EV applications". In *IECON 2012 - 38th Annual Conference on IEEE Industrial Electronics Society*. (25-28 Oct. 2012), p. 3688-3693.

Lara, J., J. Xu, and A. Chandra. 2016a. "Effects of Rotor Position Error in the Performance of Field-Oriented-Controlled PMSM Drives for Electric Vehicle Traction Applications". *IEEE Transactions on Industrial Electronics,* vol. 63, n° 8, p. 4738-4751.

Lara, J., J. Xu, and A. Chandra. 2016b. "A Novel Algorithm Based on Polynomial Approximations for an Efficient Error Compensation of Magnetic Analog Encoders in PMSMs for EVs". *IEEE Transactions on Industrial Electronics,* vol. 63, n° 6, p. 3377-3388.

Lin, P. Y. and Y. S. Lai. 2012. "Voltage Control Technique for the Extension of DC-Link Voltage Utilization of Finite-Speed SPMSM Drives". *IEEE Transactions on Industrial Electronics,* vol. 59, n° 9, p. 3392-3402.

Lin, Q., T. Li, and Z. Zhou. 2011. "Error Analysis and Compensation of the Orthogonal Magnetic Encoder". In *Instrumentation, Measurement, Computer, Communication and Control, 2011 First International Conference on*. (21-23 Oct. 2011), p. 11-14.

Liu, J. M. and Z. Q. Zhu. 2014. "Sensorless Control Strategy by Square-Waveform High-Frequency Pulsating Signal Injection Into Stationary Reference Frame". *IEEE Journal of Emerging and Selected Topics in Power Electronics,* vol. 2, n° 2, p. 171-180.

Longya, Xu and Wang Changjiang. 1998. "Implementation and experimental investigation of sensorless control schemes for PMSM in super-high variable speed operation". In *Industry Applications Conference, 1998. Thirty-Third IAS Annual Meeting. The 1998 IEEE*. (12-15 Oct. 1998) Vol. 1, p. 483-489 vol.1.

Luo, X., Q. Tang, A. Shen, and Q. Zhang. 2016. "PMSM Sensorless Control by Injecting HF Pulsating Carrier Signal Into Estimated Fixed-Frequency Rotating Reference Frame". *IEEE Transactions on Industrial Electronics,* vol. 63, n° 4, p. 2294-2303.

Masaki, R., S. Kaneko, M. Hombu, T. Sawada, and S. Yoshihara. 2002. "Development of a position sensorless control system on an electric vehicle driven by a permanent magnet synchronous motor". In *Power Conversion Conference, 2002. PCC-Osaka 2002. Proceedings of the*. (2002) Vol. 2, p. 571-576 vol.2.

Mattavelli, P., L. Tubiana, and M. Zigliotto. 2005. "Torque-ripple reduction in PM synchronous motor drives using repetitive current control". *IEEE Transactions on Power Electronics,* vol. 20, n° 6, p. 1423-1431.

Mohamed, Y. A. R. I. and E. F. El-Saadany. 2008. "A Current Control Scheme With an Adaptive Internal Model for Torque Ripple Minimization and Robust Current Regulation in PMSM Drive Systems". *IEEE Transactions on Energy Conversion,* vol. 23, n° 1, p. 92-100.

Mok, H. S., S. H. Kim, and Y. H. Cho. 2007. "Reduction of PMSM torque ripple caused by resolver position error". *Electronics Letters,* vol. 43, n° 11, p. 646-647.

Moldovan, A., F. Blaabjerg, and I. Boldea. 2011. "Active-flux-based, V/f-with-stabilizing-loops versus sensorless vector control of IPMSM Drives". In *2011 IEEE International Symposium on Industrial Electronics*. (27-30 June 2011), p. 514-519.

Morimoto, S., M. Sanada, and Y. Takeda. 1994. "Effects and Compensation of Magnetic Saturation in Flux-Weakening Controlled Permanent Magnet Synchronous Motor Drives". *IEEE Transactions on Industry Applications,* vol. 30, n° 6, p. 1632.

Morimoto, S., Y. Takeda, T. Hirasa, and K. Taniguchi. 1990. "Expansion of operating limits for permanent magnet motor by current vector control considering inverter capacity". *IEEE Transactions on Industry Applications,* vol. 26, n° 5, p. 866-871.

Nakao, N. and K. Akatsu. 2014. "Suppressing Pulsating Torques: Torque Ripple Control for Synchronous Motors". *IEEE Industry Applications Magazine,* vol. 20, n° 6, p. 33-44.

Nalepa, R. and T. Orlowska-Kowalska. 2012. "Optimum Trajectory Control of the Current Vector of a Nonsalient-Pole PMSM in the Field-Weakening Region". *IEEE Transactions on Industrial Electronics,* vol. 59, n° 7, p. 2867-2876.

Nasiri-Gheidari, Z. and F. Tootoonchian. 2015. "Axial Flux Resolver Design Techniques for Minimizing Position Error Due to Static Eccentricities". *IEEE Sensors Journal,* vol. 15, n° 7, p. 4027-4034.

Ogasawara, S. and H. Akagi. 1998. "Implementation and position control performance of a position-sensorless IPM motor drive system based on magnetic saliency". *IEEE Transactions on Industry Applications,* vol. 34, n° 4, p. 806-812.

Perera, P. D. C., F. Blaabjerg, J. K. Pedersen, and P. Thogersen. 2003. "A sensorless, stable V/f control method for permanent-magnet synchronous motor drives". *IEEE Transactions on Industry Applications,* vol. 39, n° 3, p. 783-791.

Petrovic, V., R. Ortega, A. M. Stankovic, and G. Tadmor. 2000. "Design and implementation of an adaptive controller for torque ripple minimization in PM synchronous motors". *IEEE Transactions on Power Electronics,* vol. 15, n° 5, p. 871-880.

Petrovic, V., A. M. Stankovic, and V. Blasko. 2003. "Position estimation in salient PM synchronous motors based on PWM excitation transients". *IEEE Transactions on Industry Applications,* vol. 39, n° 3, p. 835-843.

Preindl, M. and S. Bolognani. 2015. "Optimal State Reference Computation With Constrained MTPA Criterion for PM Motor Drives". *IEEE Transactions on Power Electronics,* vol. 30, n° 8, p. 4524-4535.

Qamar, N. Abou, C. J. Hatziadoniu, and H. Wang. 2015. "Speed Error Mitigation for a DSP-Based Resolver-to-Digital Converter Using Autotuning Filters". *IEEE Transactions on Industrial Electronics,* vol. 62, n° 2, p. 1134-1139.

Rahman, K. M. and S. Hiti. 2005. "Identification of machine parameters of a synchronous motor". *IEEE Transactions on Industry Applications,* vol. 41, n° 2, p. 557-565.

Ramakrishnan, R., A. Gebregergis, M. Islam, and T. Sebastian. 2013. "Effect of position sensor error on the performance of PMSM drives for low torque ripple applications". In *Electric Machines & Drives Conference (IEMDC), 2013 IEEE International*. (12-15 May 2013), p. 1166-1173.

Rojas, S., M. A Perez, J. Rodriguez, and H. Zelaya. 2010. "Torque ripple modeling of a permanent magnet synchronous motor". In *Industrial Technology (ICIT), 2010 IEEE International Conference on*. (14-17 March 2010), p. 433-438.

Sala-Perez, P., S. Galceran-Arellano, and D. Montesinos-Miracle. 2013. "A sensorless stable V/f control method for a five-phase PMSM". In *Power Electronics and Applications (EPE), 2013 15th European Conference on*. (2-6 Sept. 2013), p. 1-10.

Sencer, B. and E. Shamoto. 2014. "Effective Torque Ripple Compensation in Feed Drive Systems Based on the Adaptive Sliding-Mode Controller". *IEEE/ASME Transactions on Mechatronics,* vol. 19, n° 6, p. 1764-1772.

Shaotang, Chen, C. Namuduri, and S. Mir. 2002. "Controller-induced parasitic torque ripples in a PM synchronous motor". *IEEE Transactions on Industry Applications,* vol. 38, n° 5, p. 1273-1281.

Shi, T., Z. Wang, and C. Xia. 2015. "Speed Measurement Error Suppression for PMSM Control System Using Self-Adaption Kalman Observer". *IEEE Transactions on Industrial Electronics,* vol. 62, n° 5, p. 2753-2763.

Shin, H. J., J. Y. Choi, H. I. Park, and S. M. Jang. 2012. "Vibration Analysis and Measurements Through Prediction of Electromagnetic Vibration Sources of Permanent Magnet Synchronous Motor Based on Analytical Magnetic Field Calculations". *IEEE Transactions on Magnetics,* vol. 48, n° 11, p. 4216-4219.

SolidEnergy. 2016. " Reinventing the battery ". Online: http://www.solidenergysystems.com/. Accessed: 20 November 2016.

Soong, W. L. and T. J. E. Miller. 1994. "Field-weakening performance of brushless synchronous AC motor drives". *IEE Proceedings - Electric Power Applications,* vol. 141, n° 6, p. 331-340.

Sue, S. M. and C. T. Pan. 2008. "Voltage-Constraint-Tracking-Based Field-Weakening Control of IPM Synchronous Motor Drives". *IEEE Transactions on Industrial Electronics,* vol. 55, n° 1, p. 340-347.

Sul, S.-K. 2011. *Control of Electric MachineDrive Systems*. Hoboken,NJ, USA: Wiley.

Sun, T., J. M. Kim, G. H. Lee, J. P. Hong, and M. R. Choi. 2011. "Effect of Pole and Slot Combination on Noise and Vibration in Permanent Magnet Synchronous Motor". *IEEE Transactions on Magnetics,* vol. 47, n° 5, p. 1038-1041.

Tan, K. K., H. X. Zhou, and Lee Tong Heng. 2002. "New interpolation method for quadrature encoder signals". *IEEE Transactions on Instrumentation and Measurement,* vol. 51, n° 5, p. 1073-1079.

Tesla. 2016. " The World's Fastest Charging Station ". Online: https://www.tesla.com/supercharger. Accessed: 20 November 2016.

Uddin, M. N. 2011. "An Adaptive-Filter-Based Torque-Ripple Minimization of a Fuzzy-Logic Controller for Speed Control of IPM Motor Drives". *IEEE Transactions on Industry Applications,* vol. 47, n° 1, p. 350-358.

Wai, J. and T. M. Jahns. 2001. "A new control technique for achieving wide constant power speed operation with an interior PM alternator machine". In *Industry Applications Conference, 2001. Thirty-Sixth IAS Annual Meeting. Conference Record of the 2001 IEEE*. (Sept. 30 2001-Oct. 4 2001) Vol. 2, p. 807-814 vol.2.

Wang, G., R. Yang, and D. Xu. 2013. "DSP-Based Control of Sensorless IPMSM Drives for Wide-Speed-Range Operation". *IEEE Transactions on Industrial Electronics,* vol. 60, n° 2, p. 720-727.

Weizhe, Qian, S. K. Panda, and Xu Jian-Xin. 2004. "Torque ripple minimization in PM synchronous motors using iterative learning control". *IEEE Transactions on Power Electronics,* vol. 19, n° 2, p. 272-279.

Weizhe, Qian, S. K. Panda, and J. X. Xu. 2005. "Speed ripple minimization in PM synchronous motor using iterative learning control". *IEEE Transactions on Energy Conversion,* vol. 20, n° 1, p. 53-61.

Wu, S. T., J. Y. Chen, and S. H. Wu. 2014. "A Rotary Encoder With an Eccentrically Mounted Ring Magnet". *IEEE Transactions on Instrumentation and Measurement,* vol. 63, n° 8, p. 1907-1915.

Xia, C., B. Ji, and Y. Yan. 2015. "Smooth Speed Control for Low-Speed High-Torque Permanent-Magnet Synchronous Motor Using Proportional-Integral-Resonant Controller". *IEEE Transactions on Industrial Electronics,* vol. 62, n° 4, p. 2123-2134.

Xu, P. L. and Z. Q. Zhu. 2016a. "Carrier Signal Injection-Based Sensorless Control for Permanent-Magnet Synchronous Machine Drives Considering Machine Parameter Asymmetry". *IEEE Transactions on Industrial Electronics,* vol. 63, n° 5, p. 2813-2824.

Xu, P. L. and Z. Q. Zhu. 2016b. "Novel Carrier Signal Injection Method Using Zero-Sequence Voltage for Sensorless Control of PMSM Drives". *IEEE Transactions on Industrial Electronics,* vol. 63, n° 4, p. 2053-2061.

Xu, Y., N. Parspour, and U. Vollmer. 2014. "Torque Ripple Minimization Using Online Estimation of the Stator Resistances With Consideration of Magnetic Saturation". *IEEE Transactions on Industrial Electronics,* vol. 61, n° 9, p. 5105-5114.

Xu, Yongxiang, Dianchen Zheng, Yanyu Wei, Jibin Zou, and Jing Shang. 2012. "DSP based all-digital resolver-to-digital conversion using DSRF-PLL". In *Power Electronics and Motion Control Conference (IPEMC), 2012 7th International*. (2-5 June 2012) Vol. 2, p. 1210-1215.

Yepes, A. G., J. Malvar, A. Vidal, O. Lopez, and J. Doval-Gandoy. 2015. "Current Harmonics Compensation Based on Multiresonant Control in Synchronous Frames

for Symmetrical n-Phase Machines". *IEEE Transactions on Industrial Electronics,* vol. 62, n° 5, p. 2708-2720.

Yoon, Y. D., S. K. Sul, S. Morimoto, and K. Ide. 2011. "High-Bandwidth Sensorless Algorithm for AC Machines Based on Square-Wave-Type Voltage Injection". *IEEE Transactions on Industry Applications,* vol. 47, n° 3, p. 1361-1370.

Yu-seok, Jeong, R. D. Lorenz, T. M. Jahns, and Sul Seung-Ki. 2005. "Initial rotor position estimation of an interior permanent-magnet synchronous machine using carrier-frequency injection methods". *IEEE Transactions on Industry Applications,* vol. 41, n° 1, p. 38-45.

Zeraoulia, M., M. E. H. Benbouzid, and D. Diallo. 2006. "Electric Motor Drive Selection Issues for HEV Propulsion Systems: A Comparative Study". *IEEE Transactions on Vehicular Technology,* vol. 55, n° 6, p. 1756-1764.

Zhu, H., X. Xiao, and Y. Li. 2012. "Torque Ripple Reduction of the Torque Predictive Control Scheme for Permanent-Magnet Synchronous Motors". *IEEE Transactions on Industrial Electronics,* vol. 59, n° 2, p. 871-877.